NOVEL MEMS ACTUATOR BASED ON METAL-INSULATOR TRANSITION

by

Chengzi Huang

A Dissertation

Submitted to the Faculty of Purdue University

In Partial Fulfillment of the Requirements for the degree of

Doctor of Philosophy

School of Materials Engineering

West Lafayette, Indiana

December 2020

THE PURDUE UNIVERSITY GRADUATE SCHOOL
STATEMENT OF COMMITTEE APPROVAL

Dr. Shriram Ramanathan, Co-Chair

School of Materials Engineering

Dr. Dana Weinstein, Co-Chair

School of Electrical and Computer Engineering

Dr. Carol Handwerker

School of Materials Engineering

Dr. Elliott Slamovich

School of Materials Engineering

Approved by:

Dr. David F. Bahr

This is for my families. Thanks for always being there with me.

ACKNOWLEDGMENTS

I would like to thank my adivsor Prof. Shriram Ramanathan not only accepting me into his program, but also for his dedicated guidance and support. Prof. Ramanathan is a great mentor who helped me found my interest and built my research professionalism step by step. I've gained numerous knowledge and experiences with phase transition oxides in Ramanathan's lab.

I would also like to thank my co-advisor Prof. Dana Weinstein, who has introduced the MEMS technology to me and helped me build my own MEMS related systems. Prof. Weinstein has provided me so many insight advice and technical support when I was hindered by challenges. Her availability and openness for questions, advice, and discussion have streamlined my doctoral work.

I greatly appreciated the significant efforts of my committee members, Prof. Carol Handwerker and Prof. Elliott Slamovich. They have been guided and supported me during the past period to keep me on track through their rich experience and valuable feedback.

Besides, I'd like to extend a big thanks to all my friends and colleagues, including Dr. Zhen Zhang, Dr. Xuegang Chen, Dr. Fan Zuo, Dr. Yifei Sun, Dr. Hai-Tian Zhang, Dr. Sandip Mondal, Dr. Koushik Ramadoss, Dr. Jun Jiang, Dr. Derek Schwanz, Qi Wang, Michael Taejoon Park, Haoming Yu from Ramanathan group, Dr. Shreyas Y. Shah, Dr. Umesh Bhaskar, Matthew J. Storey, Samuel Peana, Yanbo He, Jackson Anderson, Udit Rawat, Imtiaz Ahmed from HybridMEMS group, and Dr. Noah Opondo, Dr. Mert Torunbalci, Dr. Ben Yu, Dr. Bin Dong, Hao Tian, Sen Dai, Alex Jiang, Ozan Erturk from OxideMEMS group. I really appreciated working with those outstanding colleagues together, who are sharing knowledge in advanced science and technology without borders.

Special thanks to our SHRIMP project members: Dr. Xuegang Chen, Samuel Peana and Jackson Anderson. We've worked together, conquered every single challenges, and finally built our devices from scratch. Without the team work and collaboration, the extent and depth of this project would not have been possible.

Apart from members in my group, I want to show my appreciation to the MSE family for their support and accompany. I will always treasure the memories with the four years I

spent here. I also would like to thank every individuals within the Birck family who provided great help and support during my graduated studies.

Finally, I want to express the depth of my gratitude to my family for all they have done and their unconditional support. Since I was a child until the highest academic degree, thanks for their years of dedication!

TABLE OF CONTENTS

LIST OF TABLES

LIST OF FIGURES

ABBREVIATIONS

AFM	atomic force microscopy
ALD	atomic layer deposition
EDS	energy-dispersive X-ray spectroscopy
FEA	finite element analysis
FEM	finite element modeling
FWHM	full with half maximum
GLM	grating light modulator
HDPCVD	high density plasma chemical vapor deposition
IC	integrated circuit
ICP	inductively coupled plasma
MIT	metal-insulator transition
LPCVD	low pressure chemical vapor pressure
MEMS	micro-electromechanical system
MOEMS	micro opto eElectromechanical sysyem
MRD	Materials Research Diffractometer
MUMPS	multi user MEMS processes
RIE	reactive ion etch
RTA	Rapid Thermal Annealing
SEM	scanning electron microscope
SCREAM	single crystal reactive etching and metallization
TEC	thermal expansion coefficient
TOF-SIMS	Time of Flight Secondary Ion Mass Spectroscopy
XRD	X-ray diffraction
XPS	X-ray photoelectron spectroscopy

NOMENCLATURE

BYZ	yttrium-doped barium zirconate
DSO	$DyScO_3$
EDP	ethylene diamene pyrocatechol
KOH	potassium hydroxide
LAO	lanthanum aluminate, $LaAlO_3$
LSAT	$(LaAlO_3)_{0.3}(Sr_2\ AlTaO_6)_{0.7}$
NGO	neodymium Gallate, $NdGaO_3$
NNO	neodymium nicklate, $NdNiO_3$
PLD	pulsed laser deposition
SLAO	strontium lanthanum aluminate, $SrLaAlO_4$
SNO	samarium nicklate, $SmNiO_3$
STO	Strontium titanate, $SrTiO_3$
TMAH	tetramethyl ammonium hydroxide
YAO	yttrium aluminum perovskite, $YAlO_3$

ABSTRACT

Rare earth nickelate exhibits a series of fantastic properties based on its abnormal metal-insulator transition (MIT) phenomenon, which has attracted huge concerns from different areas since 1970s. Except for traditional thermally driven method for phase transition materials, electron doping is found to be another effective driving mechanism which origins from the strong correlation of electrons in the e_g orbital of Ni^{2+} cation. Giant changes of resistivity and lattice parameter are observed during the phase transition. Although there is no record of perovskite materials utilized in actuation area, NNO is a strong candidate based on its unique properties such as high induced strain, giant resistivity change, and fast phase transition speed. In this work, the crystal structures and phase transition mechanisms of perovskite nickelates is being discussed, and based on their performance, $NdNiO_3$ (NNO) is selected to be the core material for MicroElectroMechanical Systems (MEMS) actuators. Synthesis as well as characterization method are also introduced to further understand and utilize its unique properties in actuators. actuators with 3 different layer stack are fabricated and tested. Traditional actuation materials are being discussed in details and are compared with NNO. This study also offers us an opportunity to explore the mechanical properties of perovskite nickelates associated with the phase transition, and their application in MEMS.

Besides, a vertical multilayer VO_2 MEMS actuator is fabricated to understand the vertical structure performance. Equivalent thermal circuit is developed with a thermal response time of 0.39 ms, and COMSOL finite element analysis is performed to determine spatial distribution of current flow and temperature profile, and to verify experimental measurements of strain induced bending in this multilayer vertical structure. The obtained experimental result shows a good fit with simulation analysis, which can in future be utilized to develop a generic understanding of such vertical MEMS devices.

1. INTRODUCTION OF PEROVSKITE NICKLATE

Perovskite nickelates are a series of oxides with formula $RENiO_3$, where RE represents rare earth elements such as La, Pr, Nd, Sm, Eu, etc. As phase transition materials, $RENiO_3$ exhibit a metal-insulator transition (MIT) at a specific temperature. Below the MIT temperature, $RENiO_3$ materials function as insulators with large resistivity. Above MIT temperature, $RENiO_3$ materials transit to conductors. Lattice parameter change is accompanied with the phase transition, making it possible for actuation applications.

1.1 Crystal Structures of $RENiO_3$

Perovskite nickelates contain a rare earth atom and 8 surrounded tilted NiO_6 octahedra. The ideal perovskite structure, with formula ABX_3, is shown in Fig. 1.1 [1]. Since A is a larger cation than B, A is surrounded by 12 X anions and forms 12-fold coordination; while B is in 6-fold coordination. An ideal perovskite structure holds a perfect cubic symmetry, and in order to make A and B cations perfectly suit the interstitial between anions, the relationship between the A-X atom distance and the B-X atom distance is established [2]:

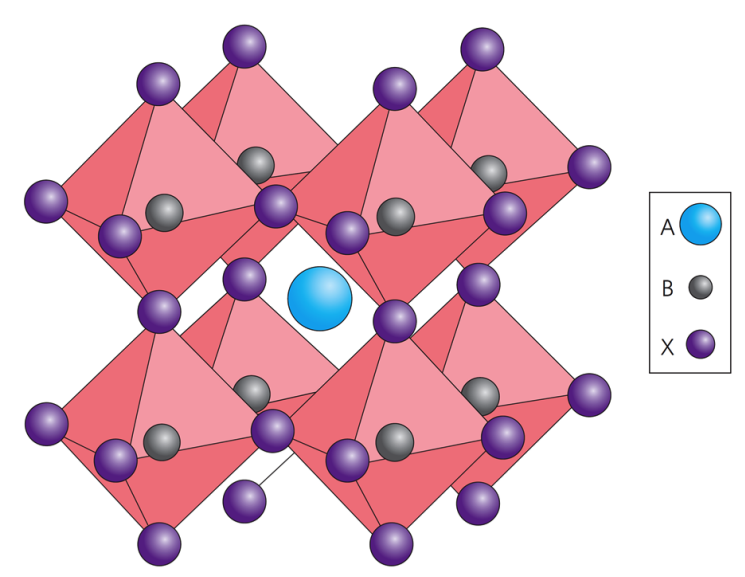

Figure 1.1. Schematic of standard perovskite ABX_3 cubic structure [1]

$$d_{A-X} = \sqrt{2} d_{B-X} \tag{1.1}$$

In the case of perovskite nickelates, the RE cations are not large enough relative to the Ni^{3+} cations to satisfy this relationship. In order to keep the whole structure stable, NiO_6 octahedra is slightly tilted to reduce extra interstitial space. The degree of distortion can be determined by the relationship between d_{A-X} and d_{B-X}, defined as the tolerance factor t [3]:

$$t = \frac{d_{A-X}}{\sqrt{2} d_{B-X}} \tag{1.2}$$

Usually people use experimental data of bond distances to calculate the tolerance factor, instead of ideal ionic radius. Medarde et al. stated that the experimental tolerance factor is slightly smaller compared with the ideal number [2]. Besides, The decrease of the tolerance factor indicates the further tilting of the NiO6 octahedra, which results in a decrease of orbital overlap. The $RENiO_3$ performs more like an insulator in stead of metallic. The orbital overlap is discussed in detail in section 1.2.

For most phase transition materials, during MIT there will be a sudden change of cell volume, while clear structure change is not accompanied [4]. On the contrast, $RENiO_3$ shows a different story. For smaller RE radius, $RENiO_3$ is *Pbnm* group when T is above MIT temperature. As temperature drops below the MIT temperature, it shows $P2_1/n$ (monoclinic) space group. Alonso et al. suggested that the monoclinic phase may exist not only in smaller RE radius. All $RENiO_3$ have minoclinic phase at low temperature phase, but they are more difficult to catch the structure from X-ray diffraction [5].

1.1.1 Room Temperature Structure

At room temperature, We discuss the crystal structure of $RENiO_3$ based on the tolerance factor. Tolerance factor is an important indicator that describes crystal structure stability and distortion. It is experimentally observed that when t is slightly smaller than 1, NiO_6 octahedra rotates along the [111] direction [6], which makes the cubic structure transfer to rhombohedral ($R\bar{3}c$), as shown in Fig. 1.2(a). Wold et al. first verified the rhom-

bohedral structure of $LaNiO_3$ by X-ray diffraction method [6]. When t is even smaller, NiO_6 distorts even severely and starts to rotate along [110] and [001] directions [7], resulting in an orthorhombic structure *Pbnm*, shown in Fig. 1.2(b). When t is smaller than 0.7, perovskite structures won't form [8].

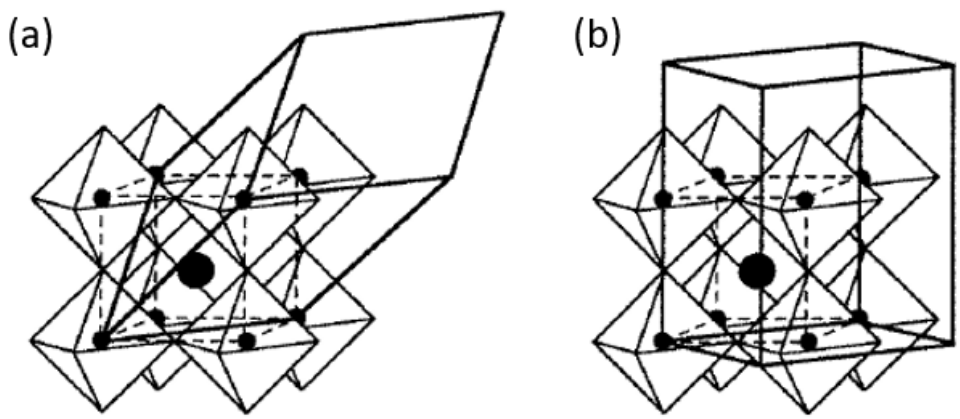

Figure 1.2. Perovskite structure with (a) rhombohedral ($R\bar{3}c$) distortion and (b) orthorhombic (*Pbnm*) distortion [2].

Experiment results have shown that except for $LaNiO_3$ which exhibited a $R\bar{3}c$ crystal structure, the remaining $RENiO_3$ nickelates all stabilize with a *Pbnm* symmetry [4]. Medarde et al. concluded the tolerance factor for each $RENiO_3$ structure [9], as plotted in Fig. 1.3. The tolerance factor of La is 0.986 based on its large ionic radius, which causes less tilted NiO_6 octahedra and forms a rhombohedral structure. For the rest of the rare earth ions, with the increasing atomic number, the nuclear shows an increase of attraction to electrons, thus resulting a smaller ion size. From Lu to Pr, the tolerance factor ranges from $t \approx 0.932$ (Lu) to $t \approx 0.975$ (Pr), and all of those $RENiO_3$ are stabilized with orthorhombic structure. Lacorre et al. figured out that the boundary of rhombohedral and orthorhombic sits at $t = 0.932$ with a series of $RENiO_3$ lattice parameter analysis, as listed on top of Fig. 1.3 [9].

1.1.2 Magnetic Properties

Garcia et al. established the magnetic structures of $PrNiO_3$ and $NdNiO_3$, as shown in Fig. 1.4. One thing that gains people's interest is that it showed the same number of

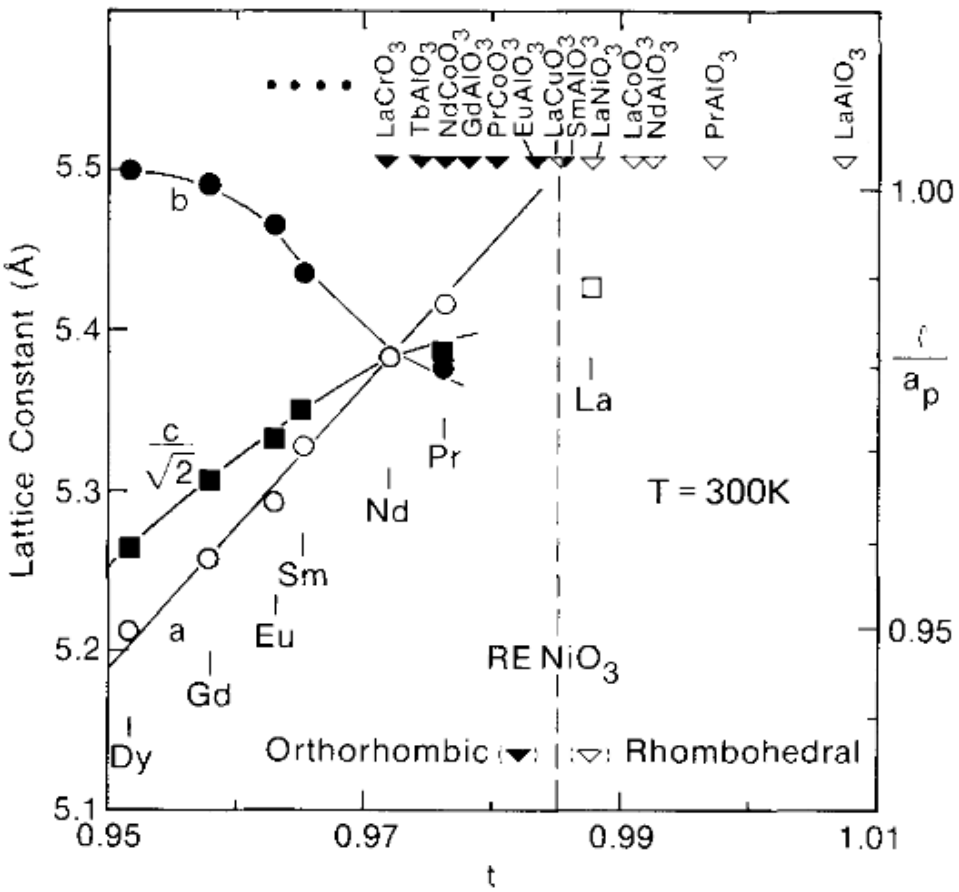

Figure 1.3. Cell parameter of perovskite nickelates as a function of tolerance factor [9]

ferromagnetic and antiferromagnetic couplings for each Ni magnetic moment. There are 6 nearest neighbours for each Ni magnetic moment, and in this proposed structure, three of them are ferromagnetic while the other three are antiferromagnetic. Such similar structures has also been found in $SmNiO_3$ [10].

In *Pbnm* strucuture, it is generally considered that the e_g orbital splits into two non-degenerate orbitals, $a_{g,1}$ and $a_{g,2}$. As discussed above, NiO_6 octahedra is slightly tilted in *Pbnm* strucuture. While the tilting angle is eligible, $a_{g,1}$ and $a_{g,2}$ can be describes as a linear relationship with e_g orbitals $d_{x^2-y^2}$ and $d_{3z^2-r^2}$ [2]:

$$a_{g,1} = \alpha_1 d_{x^2-y^2} + \beta_1 d_{3z^2-r^2} \tag{1.3}$$

$$a_{g,2} = \alpha_2 d_{x^2-y^2} + \beta_2 d_{3z^2-r^2} \tag{1.4}$$

Based on Goodenough-kanamori rule, the superexchange interactions are antiferromagnetic if the overlapping orbitals are half-filled, and virtual electron transfer happens between the orbitals. On the contrast, if the virtual electron transfer is from a fully filled orbital to a half filled orbital, or a half filled orbital to an empty orbital, the interactions are ferromagnetic. the expected situation for Ni magnetic moment is only one of the a_g orbital are occupied, which should result an antiferromagnetic structure, as shown in Fig. 1.4 (a). However, the experimentally measured structures of $PrNiO_3$, $NdNiO_3$, and $SmNiO_3$ (all of them are *Pbnm* strucutures) are a combination of ferromegnaatic and antiferromagnetic, indicating that the a_g orbital of Ni is not uniformly half filled.

Several assumptions were proposed to explain this abnormal phenomenon. Garcia et al. [10], cyrot et al. [11] indicated that the experimentally measured structure may comes from the orbital superlattice. Since the $a_{g,1}$ and $a_{g,2}$ may have very similar energy, the intraatomic exchange as well as the released energy when electrons occupies lower engergy state together may lead to a sublattice formation rom the ground dtate lattice. Another explanation is based on the cooperative Jahn-Teller effect. it states that for any non-linear molecules with spatially degenerate electronic ground state, there will be a geometrical distortion which could lower the over all energy of the system [12]. However, there is no Jahn-Teller distortion as been obeserved in $RENiO_3$ structures, making the superlattice theory a stronger candidate [2].

1.1.3 Phase Diagram of $RENiO_3$

Fig. 1.5 summarised $RENiO_3$ crystal, electrical as well as magnetic structure at different temperature based on their Re ion radius. T_{M-I} illustrated the temperature boundary of insulator and metallic phase. T_N is the Neel temperature for $RENiO_3$. Above the Neel temperature, material switches from antiferromagnetic structure to paramagnetic structure. For $RENiO_3$ With larger RE ion radius such as Nd and Pr, their Neel temperature T_N equal to the MIT temperature T_{M-I}; while for smaller RE ions from Lu to Sm, $T_N < T_{M-I}$. T_{O-R}

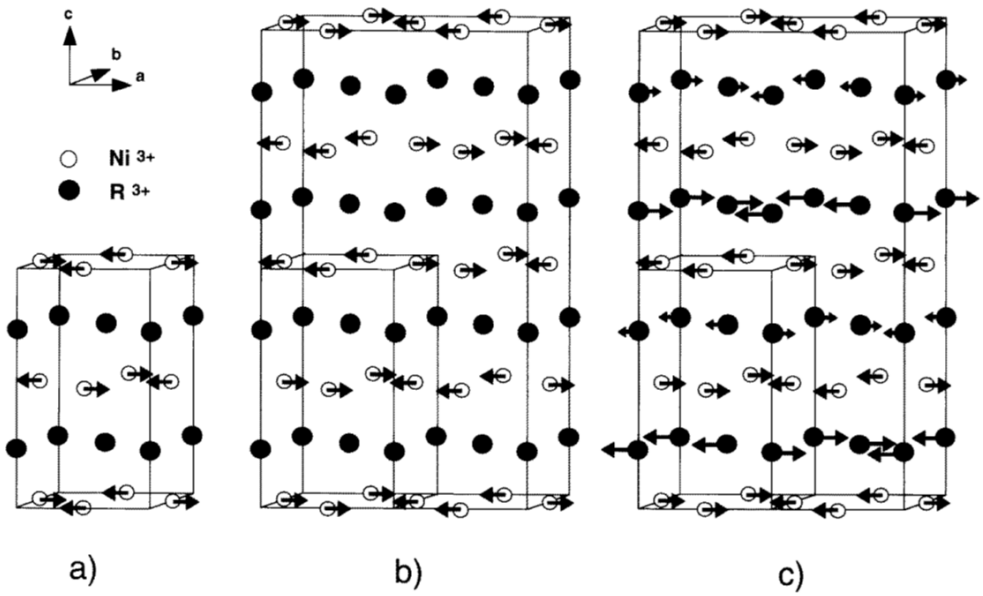

Figure 1.4. (a) Predicted [13] and (b) experimentally measured magnetic structure of $PrNiO_3$ [14]; (c) experimentally measured structure of $NdNiO_3$ [15] and $SmNiO_3$ [10] below 30 K.

is the temperature that $RENiO_3$ transfers from $Pbnm$ structure to $R\bar{3}c$ structure. As it shows in the figure, for all the $RENiO_3$, T_{O-R} is always higher than T_{M-I}, which means the $R\bar{3}c$ will only appear in high temperature phase. Besides, $LaNiO_3$ switches from $R\bar{3}c$ to $Pm3m$ (cubic) when temperature is higher than 1200 K. From the trend it is clear that with temperature increases, $RENiO_3$ transfers to a structure that has less NiO_6 distortion, and gets loser to a cubic structure.

1.2 $RENiO_3$ Phase Transition

Perovskite nickelates exhibit an abrupt first order metal-insulator transition at a certain temperature, as shown in Fig. 1.6 (a). Below the MIT temperature, nickelates acts as an insulator, and above the MIT temperature it shows an abrupt decrease in resistance. The MIT temperature also exhibits a close relation with the lattice distortion. $LaNiO_3$, which has the least NiO_6 tilting with a rhombohedral structure, shows no phase transition behavior; while from $PrNiO_3$ to $SmNiO_3$, the RE ions has decreasing ion radius, which leads to a larger

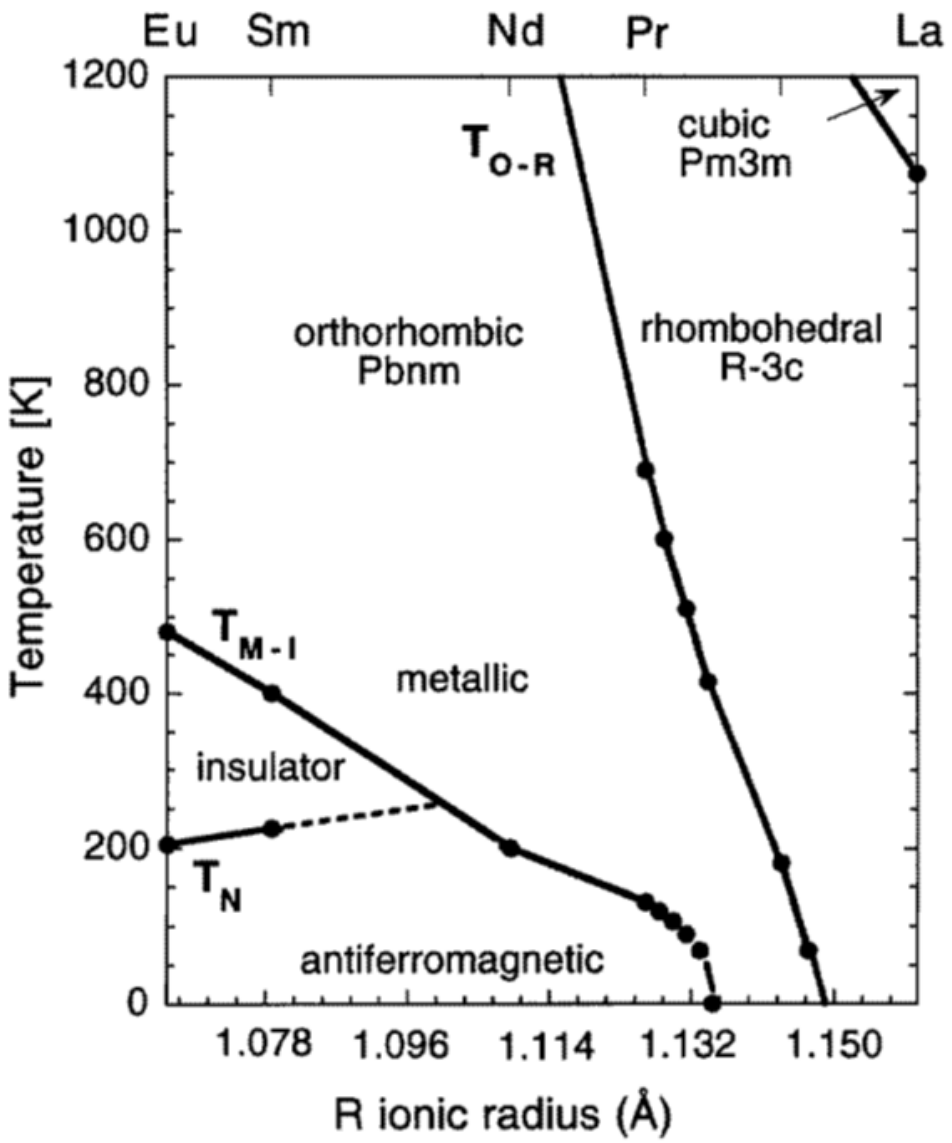

Figure 1.5. Phase diagram of $RENiO_3$ perovskites based on RE ion radius. Crystal, electrical, and magnetic structure transition is being presented [2].

NiO_6 tilting and correspondingly decreasing tolerance factor. From the figure we can clearly read that the tolerance factor is negatively proportional to the MIT temperature.

Furthermore, the phase transition is accompanied with 0.2% volume expansion at the MIT temperature, as shown in Fig. 1.6(b). The volume increase comes from two parts: (1) the Ni-O distance increase as well as (2) the Ni-O-Ni superexchange angle θ decrease. θ is defined as:

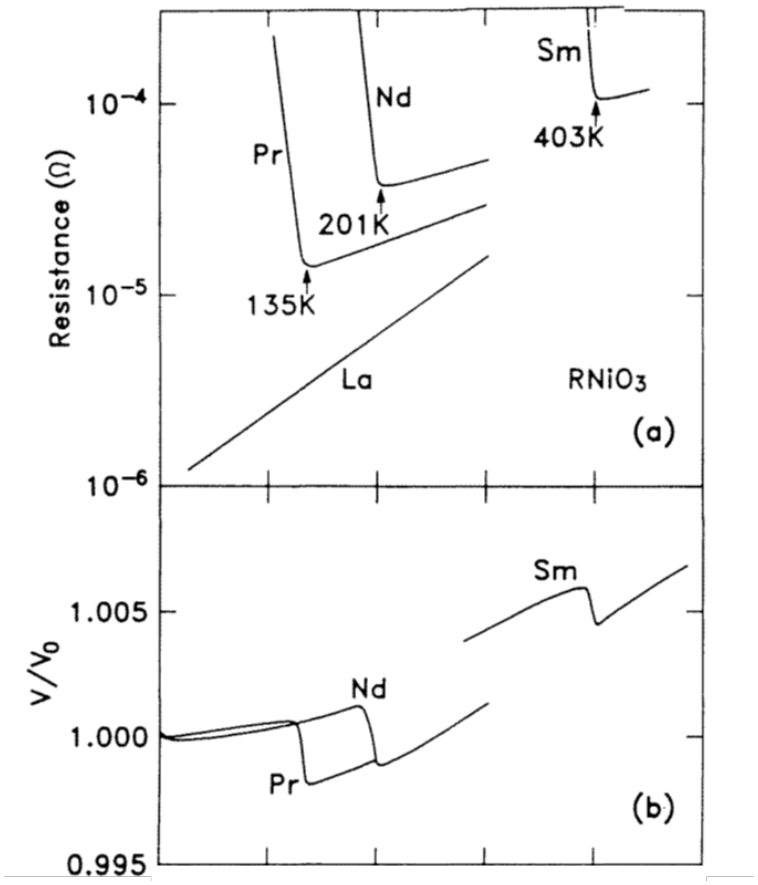

Figure 1.6. Cell parameter of perovskite nickelates as a function of tolerance factor [16].

$$\theta \approx \pi - 2\omega \tag{1.5}$$

where ω is the NiO_6 tilting angle we discussed above. Fig. 1.7 clearly illustrates the trends of Ni-O distance change as well as Ni-O-Ni superexchange angle θ change. As temperature goes above the MIT temperature, the Ni-O distance decreases, indicating the NiO_6 distortion is getting larger; the decrease of θ also proves that NiO_6 is further tilted when the phase transition happened.

1.2.1 Phase Transition Mechanism

Ni valence is an important factor in the properties of the correlated perovskite nickelates because it affects the band structure. Consider the d orbital of an octahedra Ni ion. In the

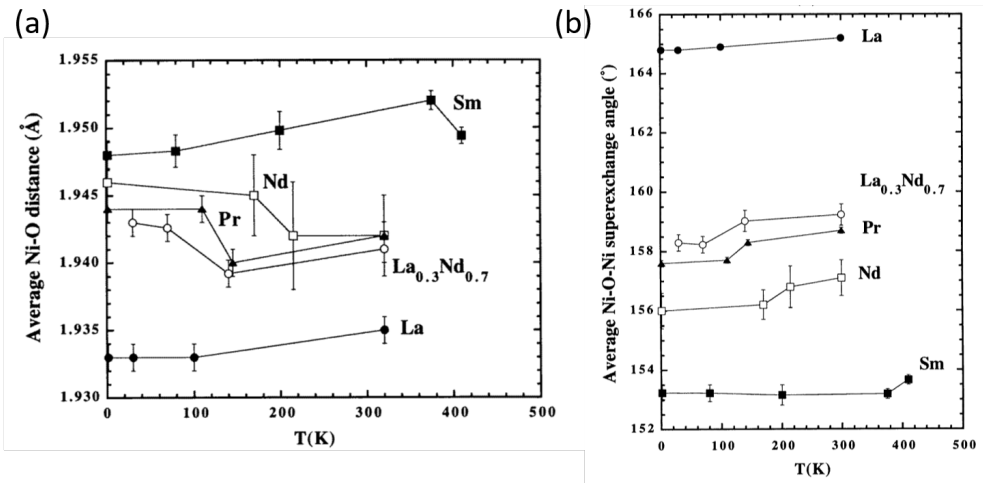

Figure 1.7. (a) Ni-O distance change and (b) θ change in $RENiO_3$ across MIT temperature [2].

octahedral structure the 5 degenerated d orbitals split into t_{2g} and e_g orbitals [17]. The e_g orbital carries higher energy because it is farther away from oxygen ligands. The orbital energy diagram is shown in Fig. 1.8. For a Ni^{3+} ion, the orbital diagram is $Ni^{3+}t_2g^6e_g^1$, only one single electron is expected in the e_g orbital. Beyond the phase transition temperature, all the Ni stay at Ni^{3+} state, and the total structure is metallic. While in a low temperature case, it is believed that the charge disproportionation of Ni^{3+} results in the insulating phase, described as [18]

$$Ni^{3+}t_{2g}^6e_g^1 \longrightarrow Ni^{2+}t_{2g}^6e_g^2 + Ni^{4+}t_{2g}^6e_g^0 \tag{1.6}$$

For Ni^{4+} ions, there is no electron in the e_g orbital; and for Ni^{2+} ions, the e_g orbital is half filled by 2 electrons, where 2 electrons are strongly correlated with each other. Due to the strong correlation, there are no free electrons in Ni^{2+} ions. Such disproportionation of Ni created a new band diagram, as shown in Fig. 1.3(b). This figure shows that a small band gap (around several hundred millivolts [20]) is formed, and the metallic nickelate transferred to insulating phase, with its resistivity increased one to two orders of magnitude.

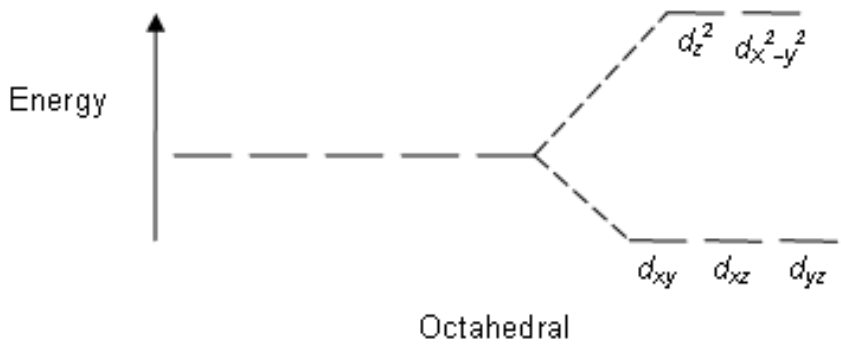

Figure 1.8. splitting of d orbitals in octahedral structure [19]

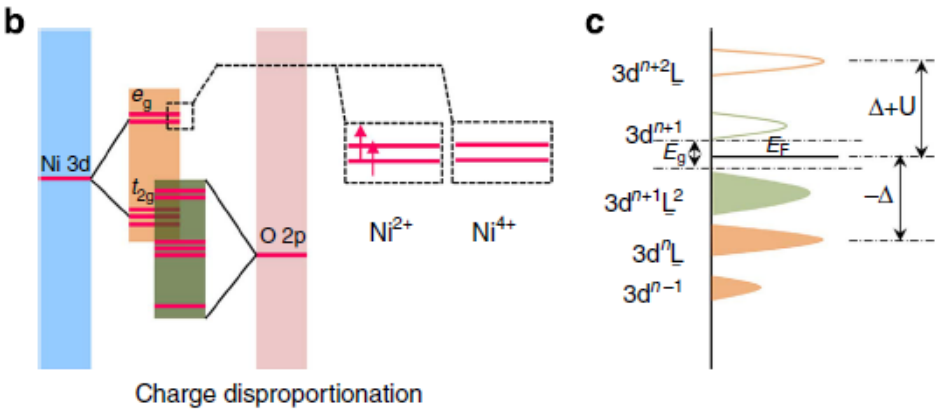

Figure 1.9. Schematics of molecular orbitals and band diagram of Ni^{3+} charge disproportionation [20].

1.2.2 Hysteresis

$RENiO_3$ perovskite also shows the hysteresis behavior during MIT because of the first order transition nature. Hysteresis shows the dependence of the state of the material based on its previous state, and in the case of $RENiO_3$, it indicates a coexistence state of both high temperature and low temperature structure in a temperature range which near the MIT temperature. A trend is found that for $RENiO_3$ perovskites which have higher MIT temperature, they show a smaller hysteresis, and for some compounds the hysteresis even disappeared. Granados et al. thought the reason is the transformation dynamics [21], [22].

At higher temperature, more thermal energy is available, which enables a faster transition and as a result a smaller temperature range of phase coexistence. As the hysteresis is related with dynamic thermal response, Mogrinski et al. mentioned that when a rapid cooling is applied to $RENiO_3$, the material will be quenched and stay in the high temperature metallic state[23].

Fig. 1.10 shows the hysteresis of resistance and *Granados et al* transferred the resistance change into volume change during MIT [22]. The MIT temperature is defined where the differential of lnR reaches the maximum point.

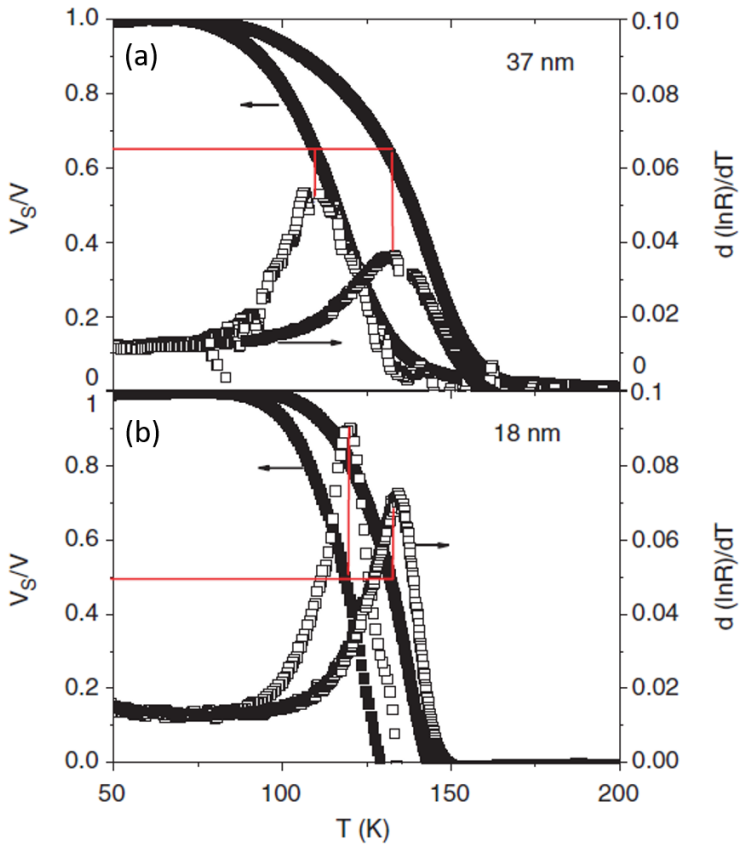

Figure 1.10. Schematics of molecular orbitals and band diagram of Ni^{3+} charge disproportionation [20].

While hysteresis is closely related with thermal performance, the nature of hysteresis is considered to be the coupling between magnetic and electrical transition in $RENiO_3$ [24]. As we mentioned in section 1.1.3, for some $RENiO_3$ their Neel temperature equals to the

MIT temperature, and only in those $RENiO_3$ perovskites resistance hysteresis is observed. For $RENiO_3$ with the case $T_{MI} > T_N$, there is no resistance hysteresis [25], [26].

1.2.3 Systematic Change among Rare Earth Elements

There are systematic periodic trends among $RENiO_3$ in both physical and structural properties. The MIT temperature increases with the decreasing ion size from La to Lu. La holds the metallic phase when temperature is higher than 1.5 K ; for Pr, Nd, and Sm the MIT temperature is 135, 200 and 400 K separately. Around 1 to 2 orders of magnitude of resistance change can be observed during MIT [8], accompanied with small discontinuous volume change [17].

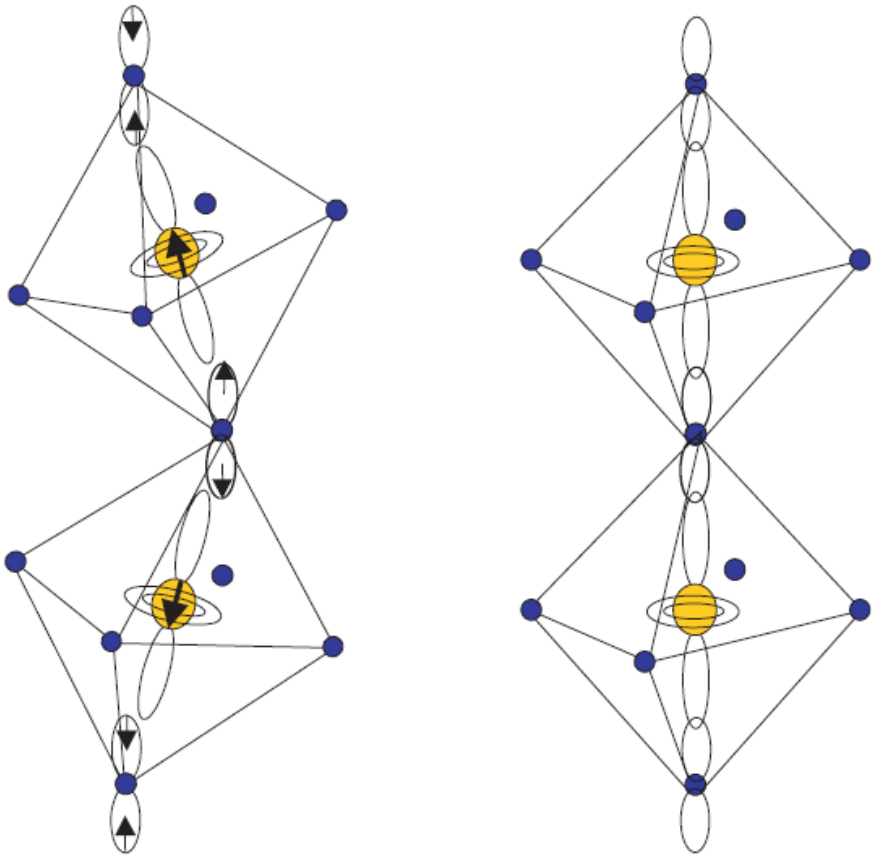

Figure 1.11. left figure plots the tilted NiO_6 octahedra, which reduces nickel and oxygen orbital overlap; right figure is the octahedra without distortion as a comparison [24].

This change can be explained by the distortion of NiO_6 octahedra. Based on the RE ion size, the NiO_6 octahedra are tilted to stabilize the structure, and here a Ni-O-Ni bond angle reduction along 2 NiO_6 octahedra is expected [4]. In this case, the orbital overlap between nickel and oxygen will be reduced by the tilted NiO_6 octahedra, enhancing the insulating phase. Fig. 1.11 depicts this idea [24]. As the tolerance factor decreases, there is a more and more severe distortion, and the phase transition temperature systematically increases.

From here we can find one distinct difference among $RENiO_3$: their phase transition temperatures range from 1.5 K to 600 K, as shown in Fig. 1.12. When mixing two nickelates with different RE ion sizes, there is a systematic modulation in transition temperature. For example, the phase transition temperatures of $NdNiO_3$ (NNO) and $SmNiO_3$ (SNO) are 200 K and 410 K. G. Frand et al. Mixed Nd and Sm in appropriate ratio, and got the product $Nd_{0.45}Sm_{0.55}NiO_3$ with phase transition occurs at room temperature [27]. This theoretically ensures the possibility to find a mixed $RENiO_3$ with any desired phase transition temperature from 1.5 K to 600 K.

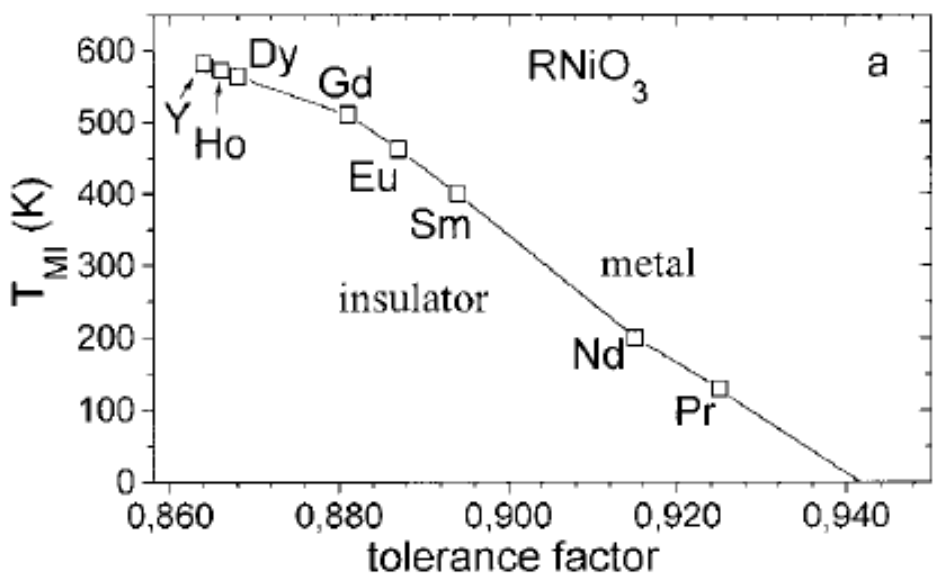

Figure 1.12. MIT temperature of nickelates with different RE ions. The difference of ion size results in systematic trends of tolerance factor, thus affected MIT temperature [28].

1.3 Strain Effect

Since lattice parameter strongly influences the phase transition of $RENiO_3$, the epitaxial strain induced by the substrate is crucial for transition behavior modification. As we discussed before, the tilted NiO_6 octahedra will favor an insulating phase. However, the effect of strain can be described in two aspects, for example, a compressive strain will result in an even tilted NiO_6 octahedra, which enhances the insulating phase and increases the transition temperature; on the other hand, the Ni-O bond shrinks at the same time, which reduces the Ni-O-Ni angle and increases the orbital overlap, causing a decrease in the transition temperature [24]. G. H. Aydogdu et al. deposited SNO thin films via magnetron sputtering on $LaAlO_3$ (LAO), $SrTiO_3$ (STO), $SrLaAlO_4$ (SLAO), Si and Al_2O_3, where each substrate has a different lattice mismatch with SNO. It was observed that compressive strain is able to stabilize the Ni^{3+} oxidation states and thus decreases the MIT temperature, while tensile strain has the opposite effect [29]. F. Conchon et al. observed the same result with were also published. Tiwari et al. observed an increase of transition temperature when NNO is grown on compressive substrate [30]. Since film growth is highly sensitive to many experimental conditions, the comparison between different experiments is very difficult. Such problems have very high degree of complexity, and further control experiments remain to be done.

Mikheev et al. established a strain-temperature phase diagram of NNO to summarize the influence of strain caused by NNO thickness, as shown in Fig. 1.13 [31]. A negative epitaxial strain is caused to the front NNO layer by $YAlO_3$ (YAO), $LaAlO_3$ (LAO) substrate, while on the contrast, $NdGaO_3$ (NGO), $(LaAlO_3)_{0.3}(Sr_2AlTaO_6)_{0.7}$ (LSAT), $SrTiO_3$ (STO), $DyScO_3$ (DSO) contributes to a positive strain. The caused train to NNO are listed below [31]:

Compressive		Tensile	
YAO	3.58%	**NGO**	+0.86%
LAO	1.20%	**LSAT**	+0.93%
		STO	+1.72%
		DSO	+2.96%

Fig. 1.13 directly plotted the NNO phase with various strain in the temperature range from 0 K to 300 K, with different NNO thicknesses (4 unit cell to 15 unit cell) [31]. For thinner NNO, antiferromagnetic insulating (AFI) phase were mostly presented, the only exception was paramagnetic phase when temperature is above 130 K and with a large negative strain; with increasing NNO thickness, paramagnetic phase is favored. negative strain also favors paramagnetic phase.

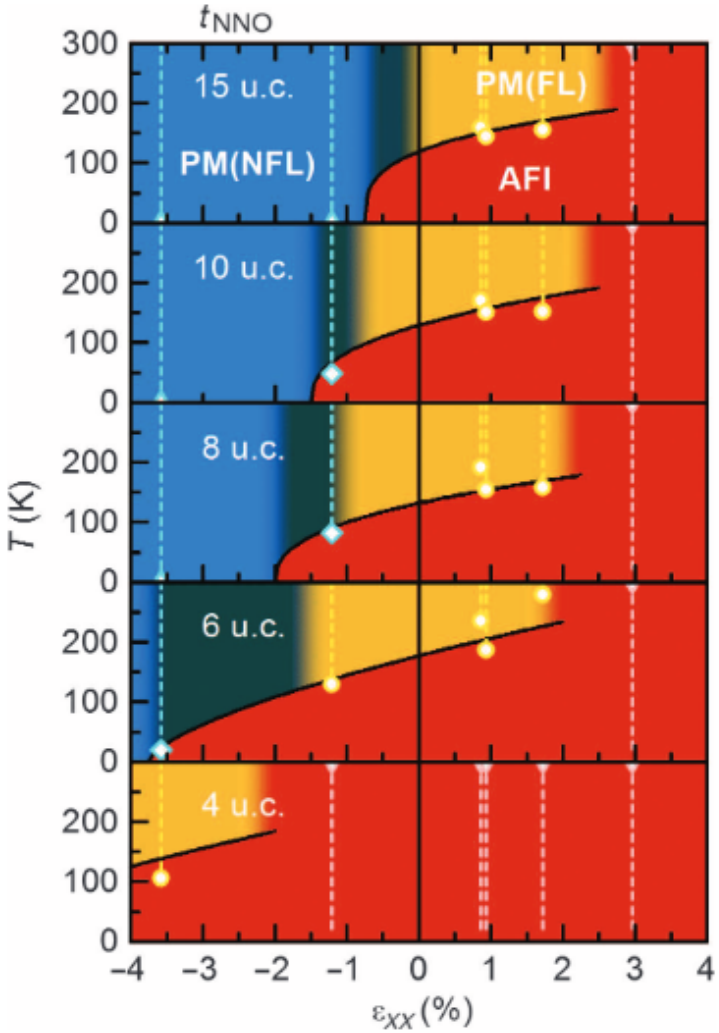

Figure 1.13. Strain-temperature phase diagram of NNO with different NNO layer thickness. The strain here is induced by different substrate, as listed in the context [31].

Except for the lattice mismatch between the substrate and perovskite nickelate, the MIT temperature is also closely related to the film thickness. When the film is very thin,

the lattice mismatch causes huge strain and thus affects the structure of nickelate; while when the film grows thicker, strain is gradually released. P. laffez et al. observed that with increasing thickness of NNO film grown on $NdGaO_3$ substrate, the MIT temperature increases and gradually approaches its original MIT temperature, as shown in Fig. 1.14[32]. This provides us another way to modulate the MIT temperature of $RENiO_3$. However, since the strain is gradually released, transport properties near the substrate are much different from the top surface, which means the whole material is not uniform.

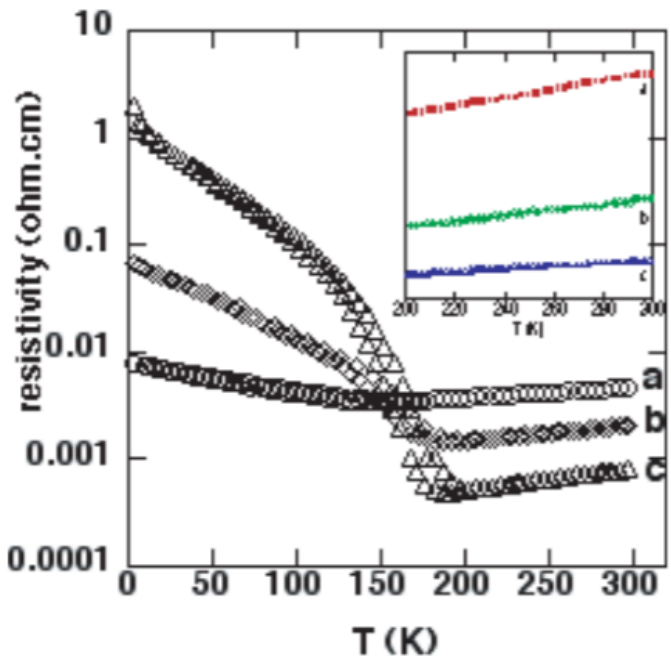

Figure 1.14. Resistivity versus temperature curve for NNO thin films, where thickness of sample a is 17 nm, whose MIT temperature is 129 K; thickness of b is 73 nm, MIT temperature 159 K; thickness of c is 150 nm, MIT temperature 182 K. Inset figure indicated their resistivity in conducting region [32].

1.4 MIT Based on Electron Doping

As discussed in section 1.2.1, the MIT of perovskite nickelates can be thermally driven by disproportionation of Ni^{3+}, introducing Ni^{2+} and Ni^{4+}. Another remarkable way to drive the phase transition is electron doping. Hydrogen or lithium can be used to provide electrons

to the structure [18]. The following sections will mainly focus on the hydrogen-based electron doping.

1.4.1 Theoretical Background

Platinum or palladium electrodes are required as a catalyst to decompose H_2 into hydrogen atoms, and these hydrogen atoms further split to H^+ ions (protons) and e^-. Protons will diffuse into the lattice accompanied with an electron based on charge neutralization. The electron joins the e_g orbital of Ni^{3+}, reducing the valence to Ni^{2+} and the doped material exhibits an insulating state. Since there are only Ni^{2+} ions here, the band diagram is simpler than the Ni^{3+} charge disproportionation case, as shown see in Fig. 1.15. Accompanied by the band diagram of oxygen ligand, a much larger band gap around several electron-volts [33] is obtained. Such electron doping transfers nickelates to a total insulator with very high resistivity.

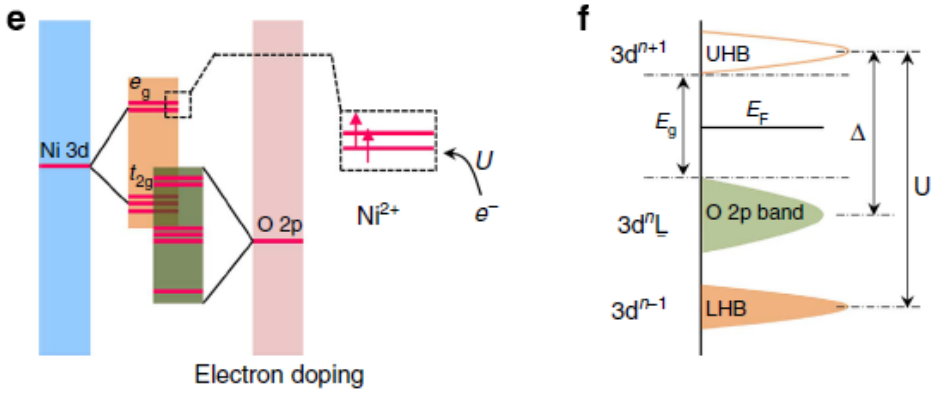

Figure 1.15. Schematics of molecular orbitals and band diagram of electron doping of Ni^{3+} [20]

1.4.2 Properties during Electron Doping

Shi et al. reported an electron doping experiment with SNO thin film epitaxially grown on $LaAlO_3$ substrate [18]. After annealing SNO in hydrogen atmosphere at 200 °C, the resistance of electron doped SNO (H-SNO) increased 8 orders of magnitude, accompanied by transparency change from opaque to semi-transparent. The H-SNO recovered to SNO

after annealing in O_3. Its resistivity-temperature curve of both pure SNO and H-SNO is plotted in Fig. 1.16. Compared with electron doping, the resistivity change caused by thermally driven phase transition is too small to be observed in the figure. Additionally, the resistance of H-SNO decreases with increasing temperature, this is due to both the thermal excitation of carriers and extraction of H_2.

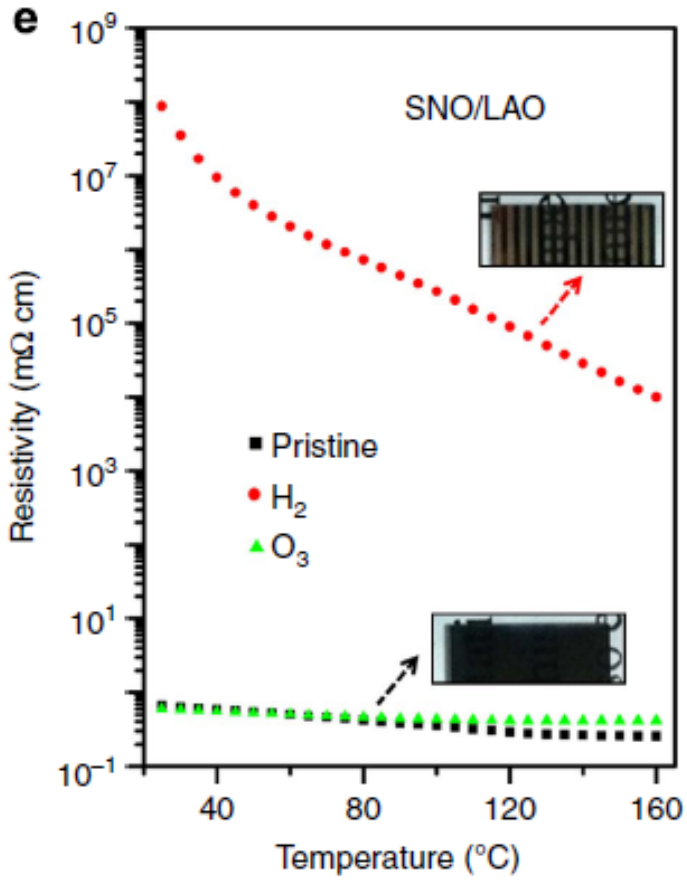

Figure 1.16. Resistivity-temperature curve for pristine (black), H2 doped (red) and recovered (green) SNO, accompanied with their optical characteristics [18].

More interestingly, when exploring the in-situ resistance change of SNO in hydrogen annealing at 50 °C, Fig. 1.17 shows that the resistance drastically increases at the beginning and gradually stabilizes; when switching the hydrogen atmosphere to air, the resistivity quickly decreases, but still remains a much higher level compared with its original value. After O_3 is introduced, SNO resistivity totally turns back to its original level.

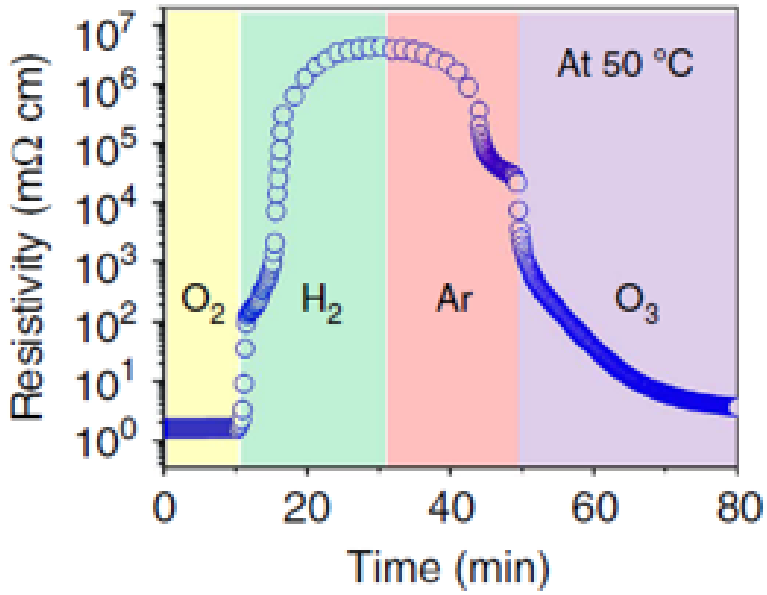

Figure 1.17. Resistivity change of SNO thin film when different gas is injected. Resistivity drastically increased when H_2 is purged in, and rapidly drop back to Pristine level when placed in Ar and O_2 atmosphere [18].

Furthermore, Y. Zhou et al. measured the lattice parameter for both pure SNO and electron doped H-SNO [34]. The lattice parameter changed from 2.98 Å to 3.18 Å during SNO (Ni^{3+}) transition to H-SNO (Ni^{2+}). This can be explained by the increase of nickel ion size. Since Ni^{2+} has a larger ionic radius, the Ni-O-Ni bond will be straightened and NiO_6 octahedra will be less tilted, resulting a larger lattice parameter of SNO. The lattice expansion shows the theoretical support of applying the phase transition behavior of perovskite nickelates into mechanical applications such as actuators.

1.4.3 Device Based on Electron Doping

A proton-gated SNO transistor is designed based on its electron doping mechanism. As shown in the schematic in Fig. 1.18, initially protons diffuse into BYZ and SNO, where BYZ layer is used to store protons. When a negative gating bias is applied, the electric field will drive protons to move into the SNO, which induces the SNO phase transition and results in an increase of the resistivity and volume, indicating an insulating phase . When negative bias is applied, protons move back to BYZ, in which case NNO will switch back to

its original metallic phase [18]. Previous research on SNO devices have inspired NNO as a candidate for creating a perovskite actuator.

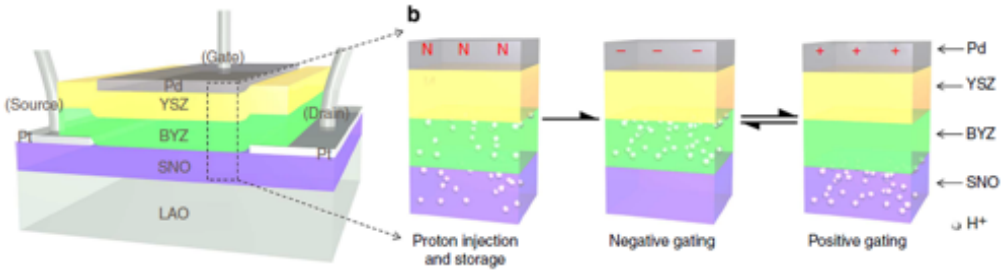

Figure 1.18. Proton gated SNO transistor and protons movement[18].

2. INTRODUCTION OF MEMS ACTUATOR

2.1 Overview of MEMS Technology

Microelectromechanical systems (MEMS) indicates the technology of microscale devices that relating electrical and mechanical components. Arising from 1970s, MEMS devices have been widely used in all kinds of applications acting as sensor, controller, and actuator in microscale, ranging from 1 μm to 100 μm. The origin of MEMS comes from integrated circuit (IC) fabrication technologies [35], nowadays MEMS has been applied in our everyday life including aerospace, information technology, robotics, medical engineering, chemical analysis, etc. Fig. 2.1 shows a simple example of a smart robot [36]. Accelerometer is used for measuring acceleration force when robot moves; Gyroscope changes the robot's orientation; Pressure sensor, tactile sensor, and force sensor can receive signals from outer environment. All those MEMS devices is connected all together with IC and built the functional robot.

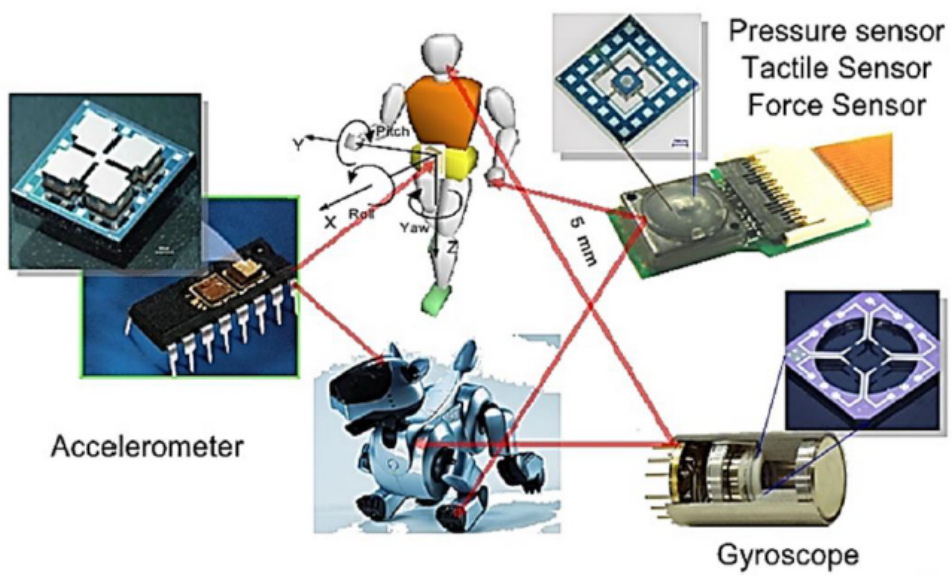

Figure 2.1. MEMS technologies applied in a smart robot [36].

MEMS technology enables the possibility that each component contributes a single functionality, while combining all the components together, a united device can realize complicated tasks. Besides, MEMS technology has its own advantages [36]: with integrated design and wafer fabrication, it minimizes the expenses and enables mass production. Moreover, with device scale in micrometer, the sensitivity and accuracy is drastically improved,

while at the same time the power consumption is largely reduced. Smaller size also makes it easier to integrate into systems, and possible to fabricate into large arrays. With all those advantages, MEMS technology is adopted in almost every fields, continuously bringing competitive applications to our daily life.

In 1947, Bell Telephone Laboratories invented transistor, which has started the empire of microelectronic technology. After that, the piezoresistive effect was found on Ge and Si in 1954, and strain gauges based on Si were began to commercialize in 1958 [37]. Those strain gauges were one of the earliest commercially distributed MEMS devices. Since 1982, Si started to become a potential candidate in MEMS, and there is a growing amount of references about its mechanical properties as well as etching data [38]. At the same time, micro-machining was becoming more and more important in fabrication. In 1971, Intel introduced their first microprocessor, Intel 4004 [39].

1987 and 1988 was a very important milestone for MEMS. The integrated fabrication was demonstrated on Si to connect rigid body with relative movement [37]. In 1992, Cornell University introduced Single Crystal reactive Etching and Metallization (SCREAM), a bulk micromachining process [40]. The same year, O. Solgaard invented the deformable grating light modulator (GLM), which is also known as Micro Opto Electromechanical sysyem (MOEMS) [41]. It was greatly applied display technology, graphic printing, and optical areas, etc. In 1993 Multi User MEMS Processes (MUMPS) was developed for low cost microsystems processing [42]. In 1998, Sandia national laboratories developed a five layer polycrystalline Si surface micromachining foundry, known as SUMMiT (Sandia Ultra-planar, Multilevel MEMS Technology) [43].

Walking into twenty first century, more and more MEMS applications has emerged based on the progress in MEMS manufacturing technologies and fabrication processes. Fig. 2.2 shows the application growth over time. MEMS is widely used in various areas, automotive, electronic, and industrial applications. Besides, MEMS started to be utlized in biological systems, such as drug delivery, glucometers, neural probe arrays, insulin pumps [44]

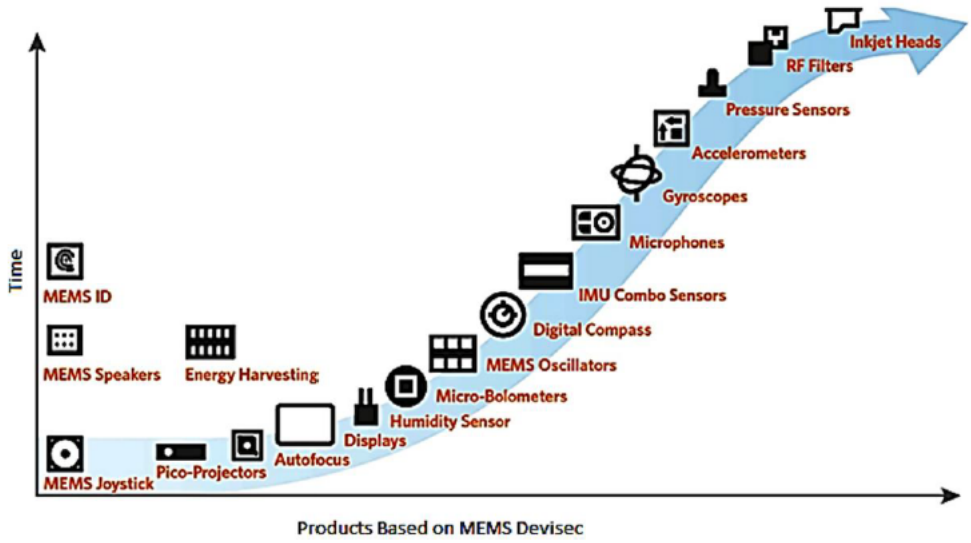

Figure 2.2. MEMS application growth over time [36].

2.2 MEMS Actuators

An actuator is a type of motor that is used to control movement or manage a mechanical system, and usually converts energy (such as electric, hydraulic, pneumatic, thermal and chemical energy) into mechanical motion [45]. Actuation systems were developed in ancient times, and after years of perfection, conventional actuator played an important role in our daily life. Nowadays with advances in micro-size fabrication as well as development of new technologies, there is a growing interest in micro actuation systems [46].

Normally, based on the actuation mechanism, actuators can be classified into 6 categories: shape memory, magnetostrictive, piezoelectric, electrostrictive, thermal expansion, and bio/chemical mechanisms [47]. Strain and Young's modulus are very important parameters to identify the performance of an actuator. Strain determines the amplitude of the actuation, while Young's modulus tells us the required applied force. Different types of actuators have diverse advantages, for example, shape memory alloys can offer giant displacements but very small loading force; on the contrast, piezoelectric materials can apply large force but tiny vibrate distances. These two parameters can be linked together by studying the volumetric work density [47], usually calculated by

$$\frac{W}{V} = \frac{E\epsilon^2}{2}. \tag{2.1}$$

2.2.1 VO_2 Actuator

When considering actuators based on other phase transition materials, VO_2 bimorph actuator, which is activated by phase transition, is an excellent example. J. Cao et al. fabricated a VO_2-Cr bimorph actuator by depositing Cr thin film on VO_2 single crystal microbeam [48]. When the bimorph layer cools down below phase transition temperature, VO_2 switches to the insulating phase and its lattice expands, while Cr shrinks due to thermal expansion. The difference between Cr and VO_2 causes a strain around 1% and thus drive the beam to deform. Fig. 2.3 illustrates the bimorph cantilever before and after phase transition, where a huge curvature change can be observed.

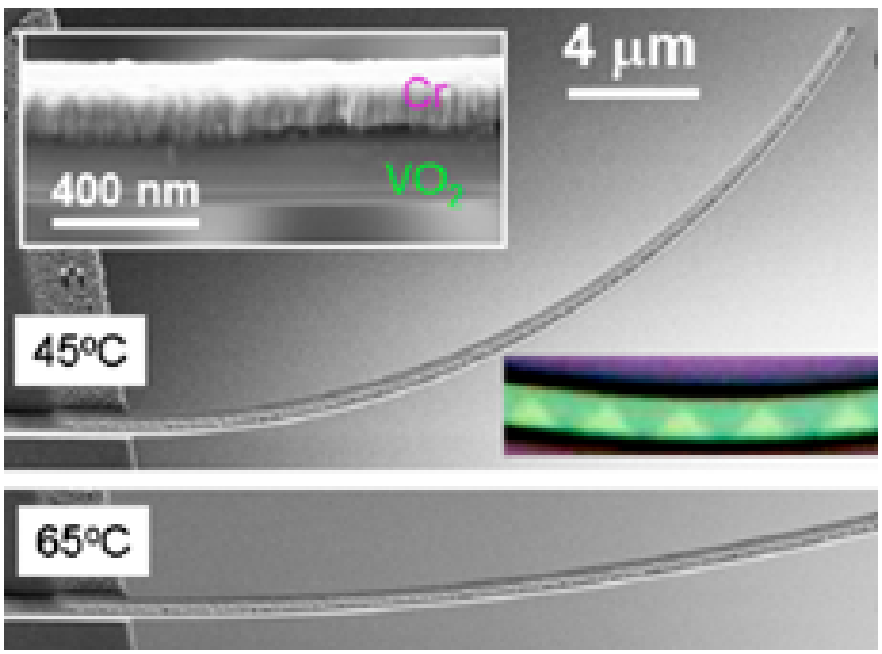

Figure 2.3. SEM images of VO_2-Cr bimorph actuator below (45 °C) and above (65 °C) phase transition temperature. Right inset picture shows the details of VO_2-Cr cantilever. Left inset picture is the optical figure of a wider VO_2-Cr cantilever [48].

However, just like most phase transition materials, the biggest problem of VO_2 bimorph actuator is the single driving method. K. Liu et al. explored different ways of activation

including adding laser or voltage [49], but the nature of all these methods is transferring energy to heat, and thus driving the phase transition. Since temperature is highly dependent on environment, such activation methods are relatively less reliable. Additionally, there is a huge energy loss when electric energy and optical energy transfer to heat, making the VO_2 bimorph actuator a low energy utilization efficiency.

2.2.2 Piezoelectric Actuator

Piezoelectric material is a type of materials that when an electric filed is applied in the axis of polarization, it will develop a mechanical strain and deform. Vice versa, internal electrical charge will be generated if a force is applied to a piezoelectric material [50]. To achieve such performance, the material is required to be non-centro symmetrical. A variety of materials exhibit such property including poled polycrystalline ceramics, single/highly oriented crystal ceramics, organic crystals, and polymers. Some of them are ferroelectrics which perform a spontaneous polarization with certain direction [51]. Schematic of a typical piezoelectric actuator is shown in Fig. 2.4. When inputting a voltage Q_3, specific displacement is generated.

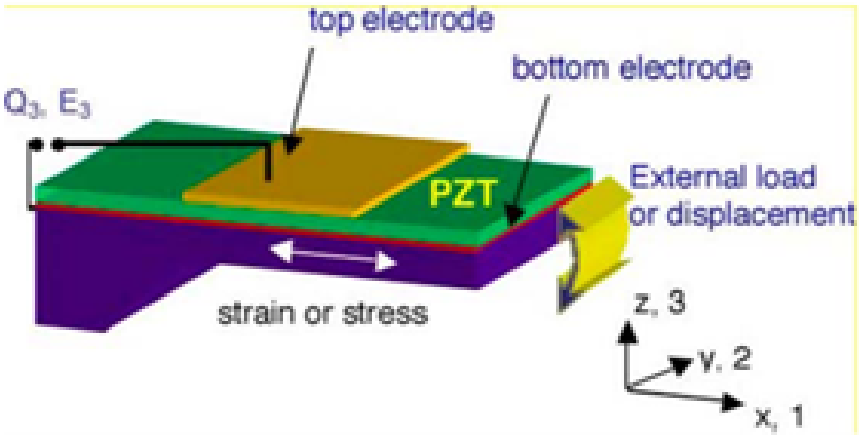

Figure 2.4. schematic of a piezoelectric actuator. Voltage Q_3 is added between top electrode and bottom electrode, and maximum displacement on the tip of cantilever is generated [52]

When considering its application on MEMS actuators, piezoelectric constant, the dielectric properties and the elastic properties play an important role. Lead zirconate titanate

(PZT) families are considered to be excellent candidate due to their high piezoelectric constants and high energy conversion efficiency [51]. They have perovskite structures, and performs different crystal symmetry including cubic, rhombohedral, tetragonal, orthorhombic under different temperature [53]. In general, materials with the perovskite structure usually have very high piezoelectric constants.

The piezoelectric constant of a material is described via d_{33} and d_{31}, which is determined by measuring the direct effect (add stress and measure the induced charge) or converse effect (add bias and measure the induced strain) [51]. Both d_{33} and d_{31} describe the relationship between the applied electric field and the induced strain, In the case of d_{33} these 2 parameters are in the same direction, while if they are perpendicular to each other, then d_{31} is applied. PZT is famous with its piezoelectric constants, while Fig. 2.5 shows out the shortage in small strain [53]. Optimization has been made to obtain larger strain, such as growing some single crystal PZT materials.

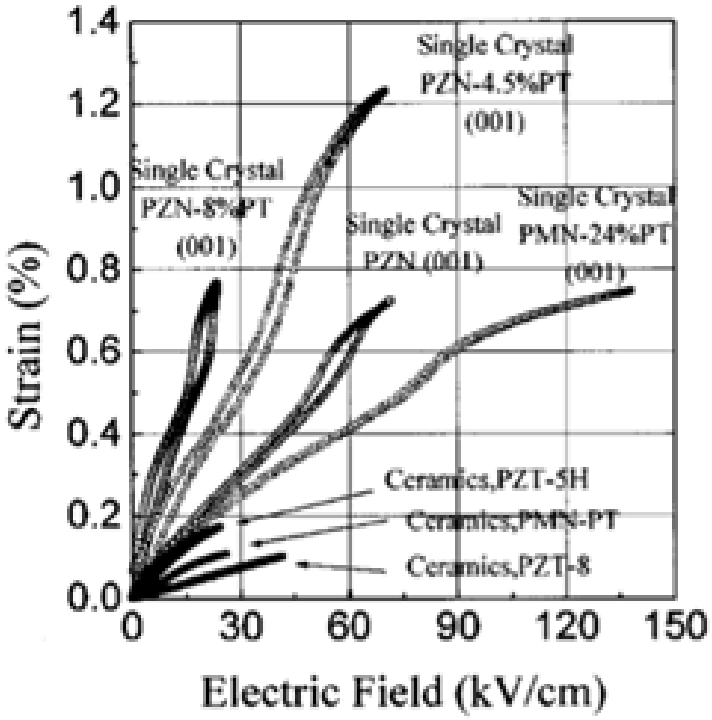

Figure 2.5. strain versus electric field for different PZT materials [53]. The maximum of strain change in PZT materials ranges from 0.1% to 1.2%.

3. MATERIALS AND METHODS

3.1 NNO Synthesis

Generally, the formation of $RENiO^{3+}$ is based on the reaction below [34]:

$$RE_2O_3 + 2NiO + \frac{1}{2}O_2 \longrightarrow RENiO_3 \tag{3.1}$$

Since normally Ni stays at bivalent charge state, Ni^{3+} is a meta-stable state and is only generated in extreme high pressure and high temperature environments. Several ways were used to synthesis $RENiO_3$ in previous works, including magnetron sputtering, pulsed laser deposition (PLD), and vapor deposition. This work is focused on the magnetron sputtering method, which is the most widely used technology to fabricate high quality $RENiO_3$ thin films.

3.1.1 Magnetron Sputtering Method

In order to achieve the stoichiometry of $RENiO_3$, separate RE target and Ni target are used as the sputtering growth source with appropriate action power. Argon/oxygen gas flow is required to generate plasma and at the same time oxidize RE and Ni. After sputtering deposition, the mixture of RE_2O_3 and NiO is obtained. As indicated before, a high pressure and high temperature annealing process is needed to make stable $RENiO_3$ structure. R. Jaramillo et al. achieved this process by annealing $RENiO_3$ in a stainless steel pressure vessel for 24 hours, keeping a condition of 770 K and 100 bar O_2 pressure [54]. It was also found that different RE ions have different requirements of temperature and pressure: nickelates with smaller RE ions are more difficult to stabilize compared with those with larger RE ions. Thermodynamic phase stability diagrams of SNO, NNO, PNO ($PrNiO_3$) are plotted in Fig. 3.1. Small rectangles are experimental data from different references. Since Sm, Nd, Pr show increasing ion size, $SmNiO_3$ has the smallest stable area, whose stabilization only occurs at very high temperature and high pressure. For NNO, fortunately the stabilization can occur at high temperature and ambient pressure, which greatly simplified the annealing process and effectively lowered the damage to other layers.

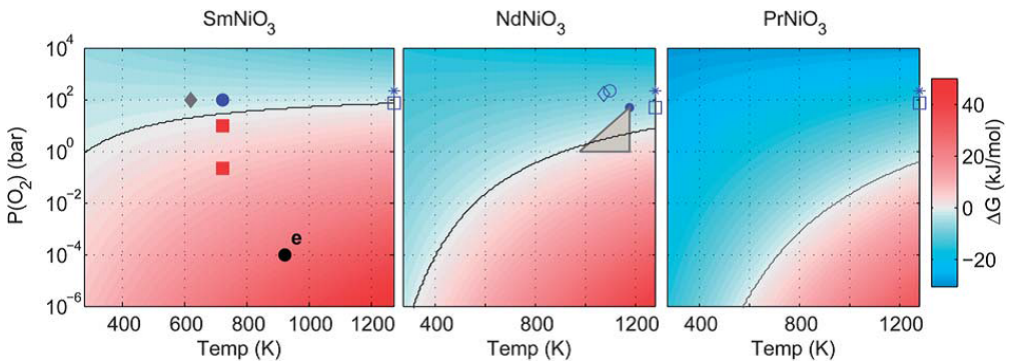

Figure 3.1. Required oxygen partial pressure and temperature for $RENiO_3$ stabilization (RE=Sm, Nd, Pr). Small dots and square are experiment data from published documents [54].

The resistance-temperature curve of NNO is shown in Fig. 3.2. Below the MIT temperature, there is a sharp decrease of resistance, which is caused by the charge disproportionation of Ni^{3+} state. Beyond the transition temperature, the increase of resistance with raising temperature just like usual metals is observed. Different experimental conditions may result in slightly different transition temperature as we discussed before, but normally it's around 200 K.

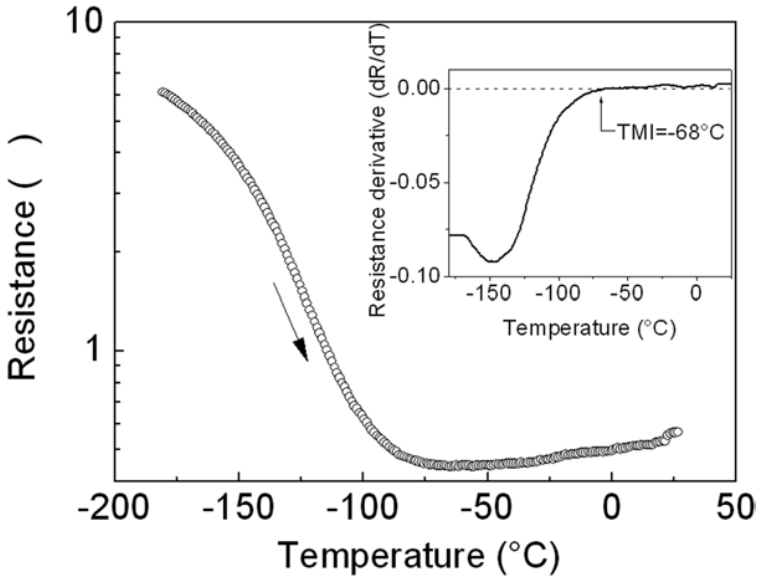

Figure 3.2. Resistance versus Temperature curve for NNO thin film. Inset plot is the derivative of resistance (dR/dT) versus temperature. MIT is defined when $dR/dT = 0$, which is -68 °C (205 K) [55].

Table 3.1. Comparison of Different Substrates for NNO Growth [57]

	MgO	STO	NGO	LAO
Substrate lattice parameter (Å)	4.2	3.89	3.86	3.79
Substrate-bulk nickelate mismatch	10.2%	2.10%	1.31%	-0.5%

3.1.2 Epitaxial Growth

Different substrates also show great influence on the thin film synthesis process. For substrates whose lattice do not match NNO, polycrystalline thin films are usually obtained. P. Laffez et al. presented their work about polycrystalline NNO growth on Silicon [56]. Single crystal substrates which has similar lattice parameters with NNO are very crucial for epitaxial growth. G. Catalan et al. compared the growth of NNO on $SrTiO_3$ (STO), $NdGaO_3$ (NGO), $LaAlO_3$ (LAO) and MgO [57], [58]. Table 3.1 displays their lattice parameters and relative lattice mismatch with NNO.

With their XRD plot in Fig. 3.3(a), NNO exhibited a preferential growth orientation 100 when deposited on STO, NGO and LAO. while for MgO substrate, which owns more than 10% mismatch of lattice parameter, NNO shows no epitaxial preference, and the crystallization is also very bad compared with epitaxially grown ones, see TEM diffraction plot in Fig. 3.3(c). The phase transition diagram further confirmed it as shown in Fig. 3.3(b), where NNO with least lattice mismatch performs the sharpest phase transition.

3.2 NNO Proton Doping Analysis

3.2.1 Transport Properties of Annealed NNO

To study the transport properties of H-NNO, the device stack shown in Fig. 3.4(a) is established. The current flows through Pd to NNO and then ITO, where Pd serves as the top electrode and ITO is the bottom electrode. The Pd pad size is 150 μm. The IV curves are measured by Keithley 2635 with the current resolution of 0.1 fA. For pristine NNO, the

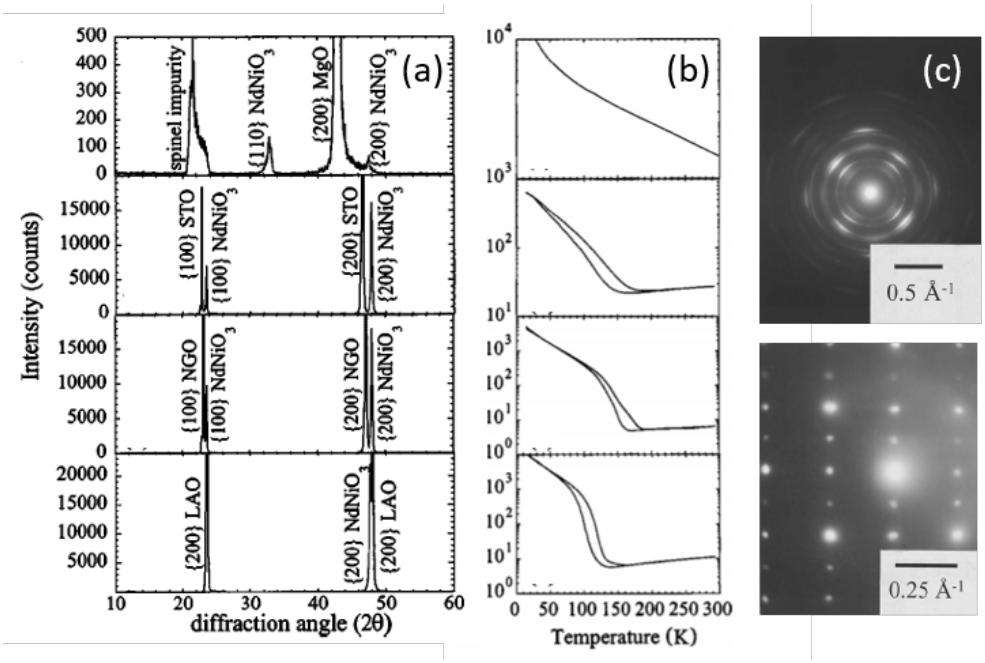

Figure 3.3. (a) XRD analysis for NNO grown on (from top to bottom) MgO, STO, NGO and LAO; (b) Resistance-temperature curve of NNO grown on (from top to bottom) MgO, STO, NGO and LAO; (c) TEM selected area diffraction for MgO (top) and NGO (bottom) [57].

measured resistance is 416 Ω in a small voltage region (0.1 V), indicating an ohmic contact and the metallic nature of the NNO stack.

To obtain H-NNO, the sample is annealed at 240O °C in H_2(5%)/Ar gas flowing setup for 20 minutes. In this annealing process, the metallic NNO is doped with proton realizing the metal-insulator transition. the IV curve presents the linear nature at a small voltage region (0.1 V), with a resistance of 750 MΩ. Compared with the pristine NNO, the resistance is increased more than six order of magnitude, indicating the appearance of insulator-metal transition. The corresponding J-E curve are displayed in Fig. 3.4(b). The J-E shows nonlinear feature for H-NNO stack with an applied electric field below 1.1 MV/cm^2 (17 V). The dielectric break down happens with the applied voltage above 17 V, where the device become conductive with a resistance of 6 Ω.

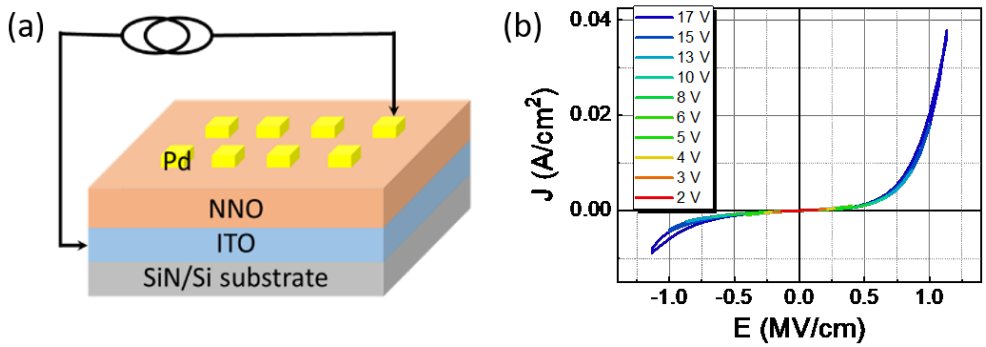

Figure 3.4. (a) Schematic of the measurement setup of Pd/NNO/ITO stack. (b) The J-E curve under various applied voltage range for H-NNO stack.

3.2.2 Annealing Time Dependent Resistance

Temperature dependent and annealing time dependent H_2 annealing studies have been conducted in order to systematically understand the H_2 doping effect in $NdNiO_3$ film as shown in Fig. 3.5. The temperature is raised from room temperature to 100 °C in 2-3 minutes with H_2/Ar gas flowing. The resistance is collected at room temperature after H_2 annealing, calculating from voltage-current data measured in linear region of 0.1 V range. It found that the resistance of NNO increases sharply when the sample is annealed in H_2 flowing gas (5 % H_2/Ar, 150 sccm gas flow). The resistance increases from 270 Ω of pristine NNO to 58.3 kΩ (180 s annealing) and 7.01 MΩ (60 s) annealing at 100 °C, indicating the fast doping process for NNO. Considering the short doping time and comparable small resistance, we can conclude that the NNO is partially doped. Continuously increase the annealing time, the resistance of HNNO will gradually increase, reaching 1.60 GΩ at 600 s at 100 °C. Then, the sample is annealed at 250 °C in air for 10 minutes in order to push the proton out of HNNO, resulting the resistance of 1.27 kΩ in lightly doped NNO. The sample is further annealing for 30 s at 200 °C with the resistance of 161 MΩ for this status HNNO sample. Then the resistance of HNNO will gradually increases to 39.8 GΩ with the 600 s H_2 annealing at 200 °C, hinting that the NNO is full doped at this annealing condition.

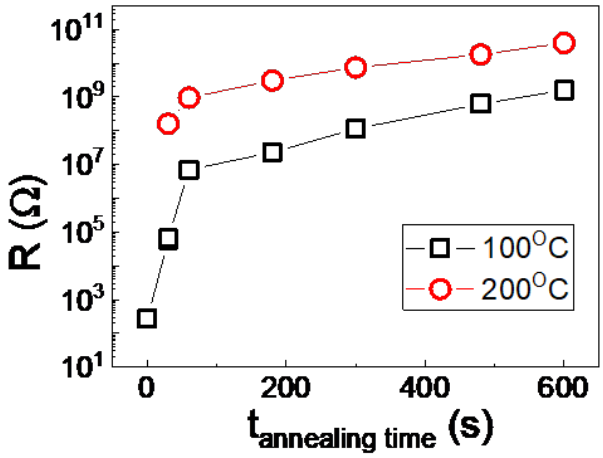

Figure 3.5. the annealing time dependent resistance at 100 °C and 200 °C.

3.2.3 SIMS Analysis of Hydrogen Doping

To further understand how protons transport during annealing process, Time of Flight Secondary Ion Mass Spectroscopy (TOF-SIMS) analysis is conducted to detect hydrogen ion distribution along the film stack. 2 different layer stacks are show in Fig. 3.6(a) is the actual sample that used for proton transportation measurement during doping process, and (b) is a control sample to exclude Pd as a H_2 split catalyst.

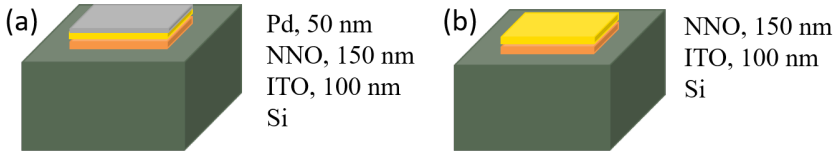

Figure 3.6. (a) Pd/NNO/ITO/Si stack for SIMS measurement and (b) NNO/ITO/Si stack as a control sample.

The SIMS result is shown in Fig. 3.7. Proton concentration versus proton diffusion depth is plotted, with varied doping conditions. doping temperature and doping time is the main parameters that tested here. For 100 °C doping temperature, 3 min and 10 min samples are selected; while for 200 °C doping temperature, since a higher temperature usually results a faster diffusion process, here 1 min, 3 min and 10 min samples are selected.

Since different layer shows different sensitivity to proton detection via SIMS, it is not advised to compare the SIMS data among different layers. Here we only compare proton

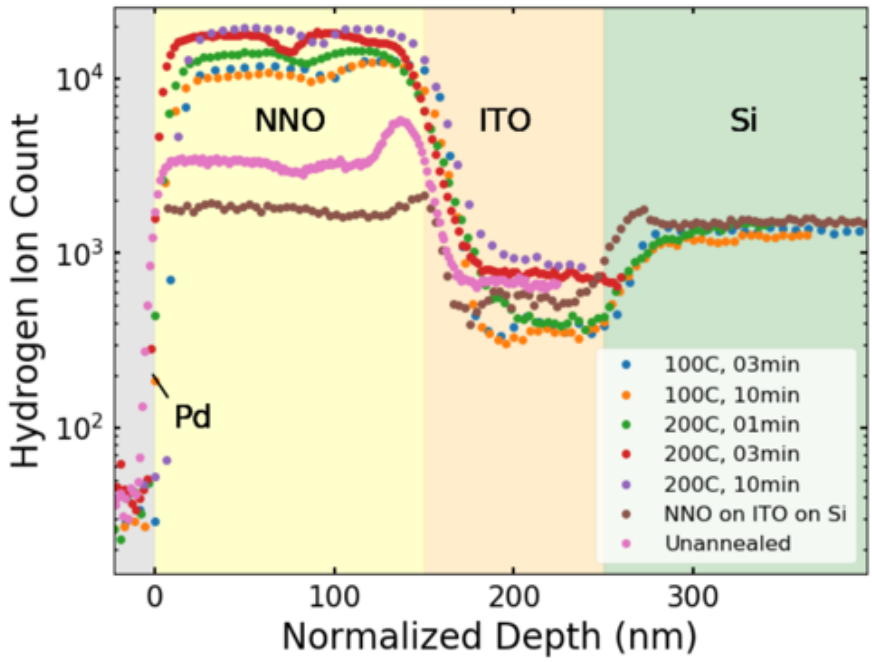

Figure 3.7. TOF-SIMS depth profile of the proton ion intensity of stacks under different annealing conditions.

concentration at the same layer with different doping condition. Considering the proton concentration in NNO layer, it is clear that the lowest concentration appeared in the unannealed sample, and control sample with NNO/ITO/Si layer stack is followed. This is because without Pd as a H_2 split catalyst, there is only a few H_2 that split and diffused into NNO, thus shows a much lower proton concentration in SIMS data. As for Pd/NNO/ITO/Si stack with different doping conditions, the 100 °C annealed samples showed a similar concentration with 3 min and 10 min anneal, but both of them are lower than all the 200 °C annealed samples. 3 min and 10 min anneal at 200 °C showed a similar proton concentration, indicating a full dope is completed.

3.2.4 Annealing Time Dependent Capacitance in HNNO

he capacitance of H_2 annealing NNO (HNNO) at different annealing time is tested and discussed in this section. The typical frequency dependent capacitance and dielectric loss tanδ with HNNO annealed for 180 s and 600 s at 100 °C are shown in Fig. 3.8. The ca-

pacitance of HNNO annealed for 180 s show a clear frequency dependent feature, decreasing from 111 pF at 500 Hz to 43 pF at 1 MHz. Considering large dielectric loss tanδ of 0.1-0.3, the capacitance signal contains other contributions such as leaky current, namely HNNO annealed for 180 s at 100 °C is not a good dielectric material. For HNNO film annealed for 600 s at 100 °C, the dielectric loss tanδ is reasonable low (below 0.1) above 40 kHz for good capacitance measurement. The capacitance is around 33-36 pF in the range of 40-1000 kHz, namely the dielectric constant around 25. Compared to the capacitance of HNNO collected at 100 °C, the capacitance of HNNO collected at 200 °C seems more reliable with pretty small dielectric loss tanδ. The capacitance of HNNO generally shows a gradual decrease as the increase of frequency, with light larger capacitance value for 180 s annealed HNNO compared to that of 600 s annealed HNNO.

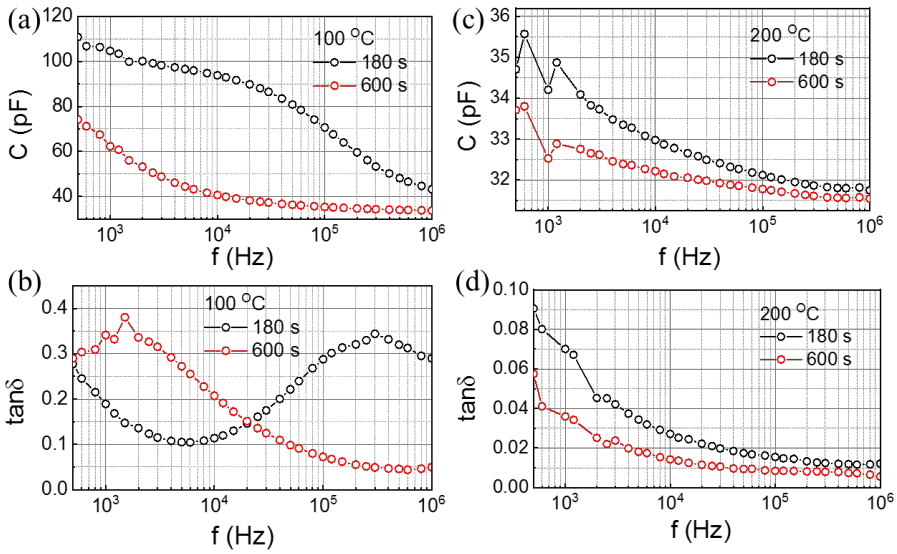

Figure 3.8. The frequency dependent capacitance (a, c) and dielectric loss tanδ (b, d) with NNO sample annealed at 100 °C and 200 °C, respectively.

The simple parallel plate capacitance model is used to calculate the dielectric of insulating HNNO film with the relation

$$\frac{\varepsilon_0 \varepsilon_r A}{d} \tag{3.2}$$

where C is the capacitance of HNNO stack. The ε_0 and ε_r are the vacuum dielectric constant and H-NNO dielectric constant. A and d are the Pd pad area and H-NNO thickness, respectively. Here, we build a simple parallel plate capacitance model with a reasonable ε_r of 23.5 shown as black curve in Fig. 3.9. We can put the corresponding capacitance data in this figure to extract the related HNNO thickness as shown in table I. Clearly, H2 annealing efficiently dopes the NNO sample, which shows time dependent doping effect at 100 °C. The calculated HNNO is 53 nm for 180 s doping while it is 123 nm for 600 s doping at 100 °C, indicating the partial doping of NNO at 100 °C (Fig. 3.9(a)). Differently, the doping level of HNNO at 200 °C is close to the thickness of 150 nm NNO, hinting that the NNO is almost fully doped at 200 °C as shown in Fig. 3.9(b)

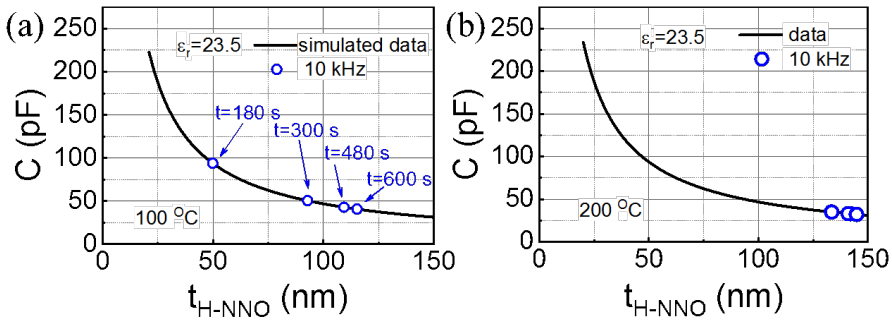

Figure 3.9. The annealing time dependent HNNO thickness for NNO sample annealed at (a) 100 °C and (b) 200 °C. The black curve is the simulated data from parallel plate capacitor model with dielectric constant of 23.5.

Table 3.2. The Annealing Time Dependent HNNO Thickness

Temperature	180 s	300 s	480 s	600 s
100 °C	53.0 nm	98.5 nm	116.5 nm	123.0 nm
200 °C	116.8 nm	122.0 nm	127.1 nm	130.5 nm

3.2.5 NNO Doping Condition Optimization

To better understand how the hydrogen anneal condition helps with electron doping, a series of experiment has been done to optimize the doping parameters including annealing temperature, annealing time and gas flow rate. The XRD measurement is done by Panalytical MRD X'Pert Pro High Resolution X-Ray Diffractometer. To get an accurate peak position, Si (400) peak is used for peak alignment, located at $2\theta = 69.58°$.

First, the doping effect at different temperature is explored. Fig. 3.10(a) shows the XRD plot of pristine and doped NNO stack, and Fig. 3.10(b) and Table. 3.3 listed the NNO (200) peak shift degrees. The H_2 anneal is processed with 150 sccm 5%H_2-95%Ar gas flow for 10 mins. When temperature is lower than 180 °C, there is nearly no peak shift, indicating that NNO is not doped; when temperature rises above 210 °C, doping of NNO is saturated. Considering too high temperature may cause permanent damage to the sample, an annealing temperature between 210 °C and 240 °C is suggested.

Table 3.3. NNO XRD Peak Shift after H_2 Anneal (Temperature Varies)

Anneal Temperature (°C)	NNO (200) 2θ Peak Position (°)
Pristine	32.98
180	32.86
210	32.35
240	32.33

The XRD plot of H_2 annealed NNO stack under different gas flow is shown in Fig. 3.11(a). Table. 3.4 listed the calculated NNO (200) peak shift degrees. Sample is annealed at 210 °C for 10 mins. When a larger flow is applied, the peak shift gets larger. From the XRD result, 100 sccm gas flow is enough for proton doping.

The XRD plot of NNO stack with different H_2 anneal duration is shown in Fig. 3.12(a). Fig. 3.12(b) and Table. 3.5 listed the calculated NNO (200) peak shift degrees. Sample is

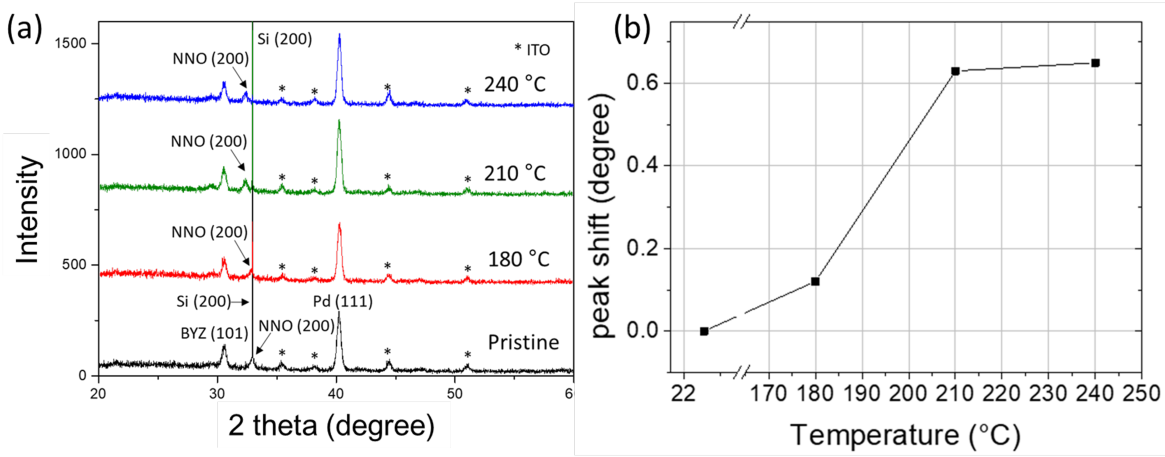

Figure 3.10. (a) XRD plot of NNO stack annealed at different temperature. Asterisk annotated are ITO substrate peaks. (b) NNO (200) peak shift versus annealing temperature. Doping gets saturated when temperature is higher than 210 °C.

Table 3.4. NNO XRD Peak Shift after H_2 Anneal (Gas Flow Varies)

Gas Flow (sccm)	NNO (200) 2θ Peak Position (°)
Pristine	32.98
50	32.64
100	32.26
150	32.25

annealed at 210 °C with 150 sccm H_2/Ar gas flow. From the plot, the doping is saturated after 10 min. Longer time annealing causes NNO peak spread out, and after 40 min anneal, the NNO (200) peak shows a lower intensity and higher FWHM (full with half maximum) compared with pristine and shorter time plot, indicating the lattice structure is turning to disordered state. Long time anneal may cause permanent damage to the sample's crystal structure.

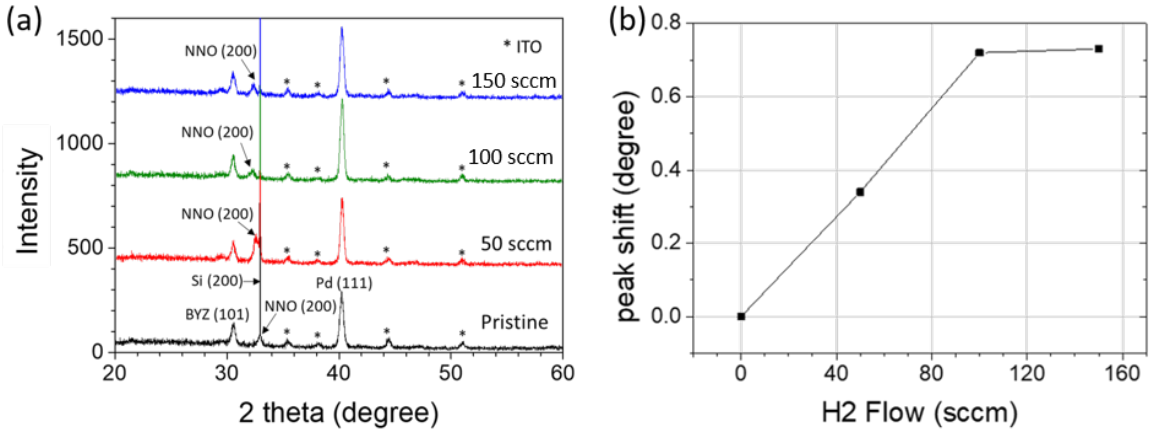

Figure 3.11. (a) XRD plot of NNO stack annealed at different H_2/Ar gas flow. Asterisk annotated are ITO substrate peaks. (b) NNO (200) peak shift versus H_2/Ar gas flow. Doping gets saturated when temperature is higher than 210 °C.

Table 3.5. NNO Layer XRD Peak Shift after H_2 Anneal (Time Varies)

Anneal Time (mins)	NNO (200) 2θ Peak Position (°)
Pristine	32.98
10	32.35
20	32.44
40	32.52

Combining all the results above, the preferred H_2 annealing condition is: 150 H_2/Ar gas flow for 10 min at 210 °C-240 °C temperature range.

3.3 Bottom Electrode: ITO

Due to the harsh annealing process of NNO (500 °C for 24h in air), ITO is selected as the bottom electrode for NNO actuator. ITO is a heavily doped n type semiconductor with a band gap of around 4 eV [59]. The large band gap makes ITO transparent in visible light range, while the heavily doped nature induces oxygen vacancies provides carriers and results

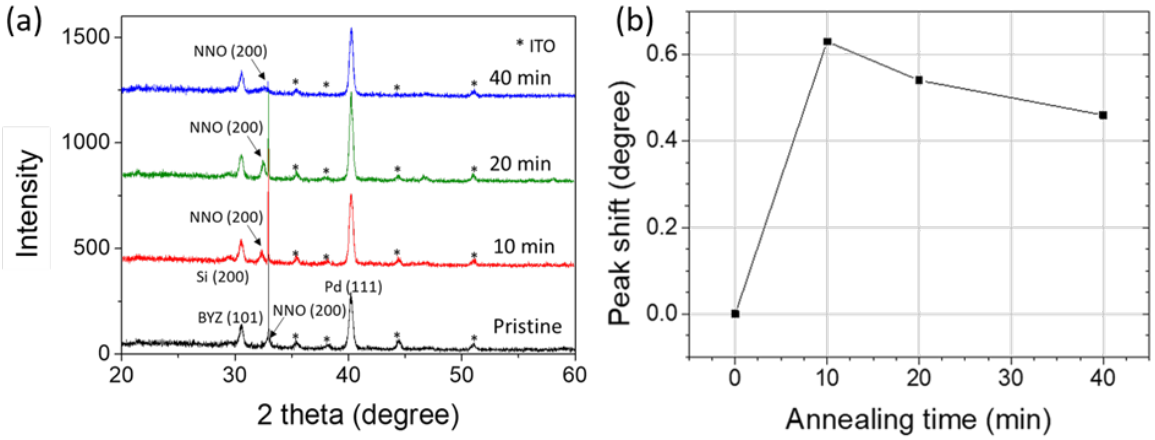

Figure 3.12. (a) XRD plot of NNO stack with different annealing duration. Asterisk annotated are ITO substrate peaks. (b) NNO (200) peak shift versus annealing duration. Doping gets saturated after 10 min.

a pretty good electrical conductivity. The combination of optical and electrical performance makes ITO a competitive candidate as a transparent oxide electrode.

Since the electrical conductivity of ITO is highly related with oxygen vacancies, the annealing process greatly affects the ITO resistivity. Hu et al. studied the influence of annealing atmosphere and temperature to ITO resistivity, as shown in Fig. 3.13(a) [60]. ITO annealing in air and in vacuum show two different trends: when ITO annealing in air, the resistivity increases when a higher temperature is applied; on the contrast, when annealing in vacuum, a higher temperature results a lower resistivity. Owning to the oxygen vacancy conducting nature, when ITO is annealed in air, the free oxygen will diffuse into ITO and react with oxygen vacancies, thus reduces the oxygen vacancy amount as well as carrier concentration. At higher temperature, more oxygen vacancies are reacted, contributing a higher resistivity. In the case of vacuum anneal, no reaction happened since there is no free oxygen in the atmosphere, higher temperature only results better crystallization, thus a decrease of ITO resistivity.

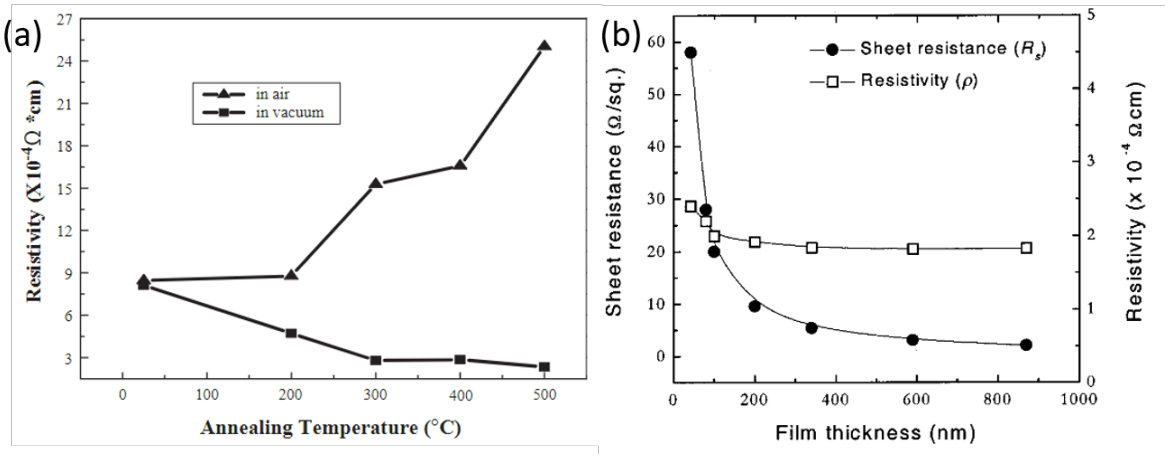

Figure 3.13. (a) ITO resistivity versus different annealing temperature, in air and in vacuum [60]. (b) Relationship of ITO resistivity, sheet resistance versus ITO film thickness [61].

The ITO resistivity also varies with ITO film thickness, especially a film that is thinner than 100 nm is considered. The relationship of ITO film thickness versus sheet resistance and resistivity is shown in Fig. 3.13(b) [61]. The sheet resistance is calculated by:

$$R = \frac{\rho}{t}\frac{L}{W} = R_s\frac{L}{w} \tag{3.3}$$

$$R_s = \frac{\rho}{t}, \tag{3.4}$$

a larger thickness is always accompanied with a smaller sheet resistance. Considering the resistivity, it shows a drastic increase when film thickness is smaller than 100 nm, and for thicker films the resistivity almost remains the same. Several explanations were provided to explain the resistivity increase in thinner films. First, a thinner film increases the possibility that carriers being scattered by the outer surface, which reduces the carriers mobility; second, when film is thinner than 100 nm, the grain size is defined by the film thickness. A thinner film means smaller grain sized as well as higher density of grain boundaries. Besides, thinner film also shows higher possibility to form islands and extensive voids, all those will contribute to a higher resistivity.

Another issue people concerned about working with ITO is the contamination problem of indium, especially in high temperature film deposition chambers. Fig. 3.14 shows the vapor pressure of common elements. While indium has a melting point of 156 °C (429 K), the vapor pressure is not as high as expected, and the boiling point of indium is as high as 2072 °C (2345 K).

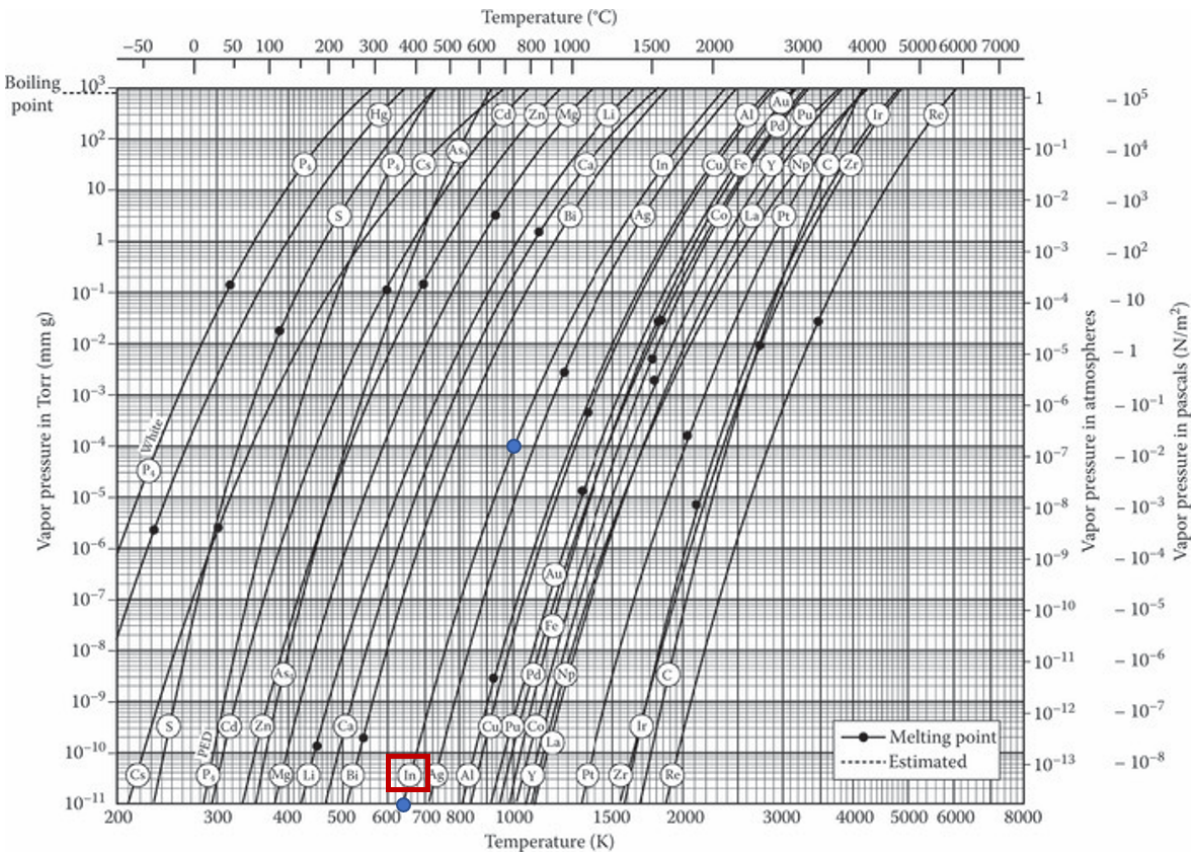

Figure 3.14. Vapor pressure of common elements [62].

Considering grow films on ITO in a ALD chamber with a chamber temperature of 200 °C, the following calculation gives the evaporation rate of indium. First, considering the pure indium case, the vapor pressure of indium at 200 °C can be calculated using Clausius-Clapeyron Equation, assuming enthalpy is temperature independent [63]:

$$ln(\frac{P_1}{P_2}) = \frac{-\Delta H_{vap}}{R}(\frac{1}{T_1} - \frac{1}{T_2}) \tag{3.5}$$

Where $-\Delta H_{vap}$ is the enthalpy of vaporization, and R is the universal gas constant, R = 8.314 J/(mol· K). Plugging in values of ITO vapor pressure from Fig. 3.14, the vapor pressure of indium at 200 °C is 1.36×10^{-18} Torr.

The evaporation rate is defined as the number of atoms leaving the surface in unit area and at unit time. The evaporation rate is highly related with material's bonding energy and the environment temperature. The expression shows below:

$$Z_A = 3.5 \times 10^2 2 \frac{P}{\sqrt{M \times T}} \tag{3.6}$$

Where

- Z_A is the evaporation rate in atoms/cm^2/s,
- P is the vapor pressure in Torr,
- T is the vapor temperature in Kelvin,
- M is the molar mass.

Plugging in the numbers for indium, $P_{473K} = 1.36 \times 10^{-18}$ Torr, $T = 473$ K, $M = 114.8$ g/mol, the evaporation rate of indium at 200 °C is $Z_A = 204.27$ atoms/cm^2/s. A comparison material is aluminum. Al is widely used in MEMS technology, and it's vapor pressure is very close to indium. using the equation above, the evaporation rate of Al at 200 °C is $Z_A = 64.29$ atoms/cm^2/s. It is clear that the evaporation rate of indium is in the same order of Al. If we decrease the evironment temperature to 150 °C, the evaporation rate of indium decrease to $Z_A = 0.17$ atoms/cm^2/s. Nearly no indium is evaporating at 150 °C, showing that when chamber temperature is lower than 150 °C, indium will not cause contamination problems.

The conclusion above is made for pure indium. For ITO films, even if there are indium extrapolated, the concentration would be much lower than pure indium metal, in this case there will not be ITO contamination when lemperature is lower than 150 °C.

3.4 NNO Actuator Fabrication

3.4.1 Layer Patterning

NNO stack patterning can be achieved either by a masked deposition method or an masked etch method. Considering multi-layer stack that needs to be patterned as well as the extra annealing process of NNO layer, the masked deposition method is complicated to realized and would bring misalignment problems. On the contrast, with the masked etch method, one mask could be used for the NNO stack patterning all the way to the ITO layer, making the process much simpler and since no extra patterning required, there is no misalignment problem as well.

For different etch methods, different masks are selected. For example, if RIE is selected as the etch method, the corresponding mask is required to have a low selectivity over etch material. The selectivity S is defined as:

$$S = \frac{\text{etch rate of material A}}{\text{etch rate of material B}} \tag{3.7}$$

In the case of ITO patterning, photoresist shows a much higher etch rate compared with ITO. A 3 μm thick photoresist is not enough to cover the etch process of 100 nm ITO. For thicker photoresists, the resolution is not high enough to transfer the ITO stack design (the smallest feature size is 3 μm). Considering the problems above, Al is selected as the etch mask for the ITO RIE process. ITO is etched by a combination of Ar and Cl_2 gas, and Al shows a very good resistance to the gas mixture. Al is a amphoteric metal, and solution that contains diluted Alkaline (such as MF-26A developer) is used for Al hard mask removal. Fig. 3.15 shows the SEM images of NNO actuator before and after ITO etch and substrate release with a Al hard mask. Al is not fully removed with diluted Alkaline solution, remaining a dirty surface of the actuator.

An alternate option of etch patterning would be photoresist mask with ion mill. Unlike RIE, ion mill shows similar etch rate to most of the materials because of the physical etch nature. This makes most of the photoresist available for the etch process. Another problem occurred during ion mill is the photoresist hardening, where a thicker photoresist is required to eliminate this problem. For the optimized photoresist, a balance should be reached for

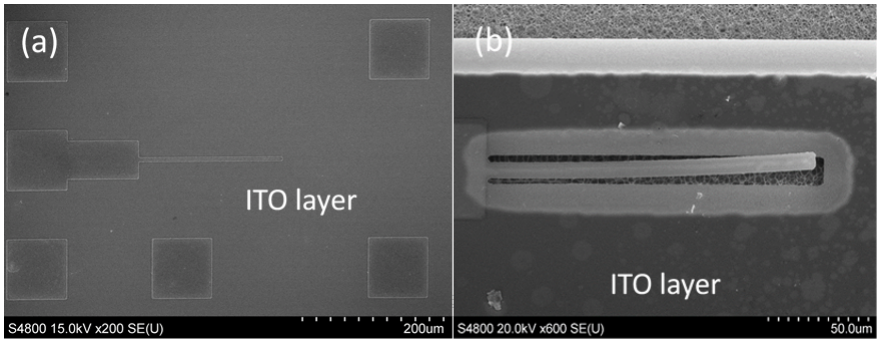

Figure 3.15. SEM pictures of NNO actuator (a) before and (b) after substrate release. During XeF_2 etching, ITO bottom electrode is covered with Al hard mask. The ITO layer shown in (b) became dirty after removing Al.

both avoiding hardening during ion mill, and at the same time has a good resolution to transfer NNO layout feature. Considering the smallest feature size is 3 μm, a 3 μm thick photoresist is selected.

3.4.2 Etch Method

Etch methods that are utilized in MEMS technology for layer patterning can be classified to 2 categories based on etch chemical: wet etch and dry etch [64], [65]. If considering the etch direction, etch methods have 2 categories: directional and isotropic [66]. For a layer patterning process, we will discuss the two types of directional etch technology in this section.

Reactive Ion Etch (RIE) is the most commonly used surface micromachining etch method in MEMS technology. In RIE, there is a reaction chamber where gas mixture split into ions by adding a RF power source. The ions are accelerated and reacts with the sample surface, then the sample is being etched. Since the ions are accelerated to a specific direction, the resulted sample etch is a also directional etch. Different materials has different etch rates when various etch gas are applied, such as Cl_2, BCl_3, CHF_3, CF_4, SF_6, etc. Different etch mask is selected based on different etch gas. While in our NNO stack, NNO layer is pretty resistive to all the etch gases, the etch rate is smaller than 5 nm/min. Such low etch rate makes it difficult to find a working etch mask. Photoresists typically couldn't sustain such

long time etch, and using metal masks would bring the mask removal problem, as discussed in section 2.4.1.

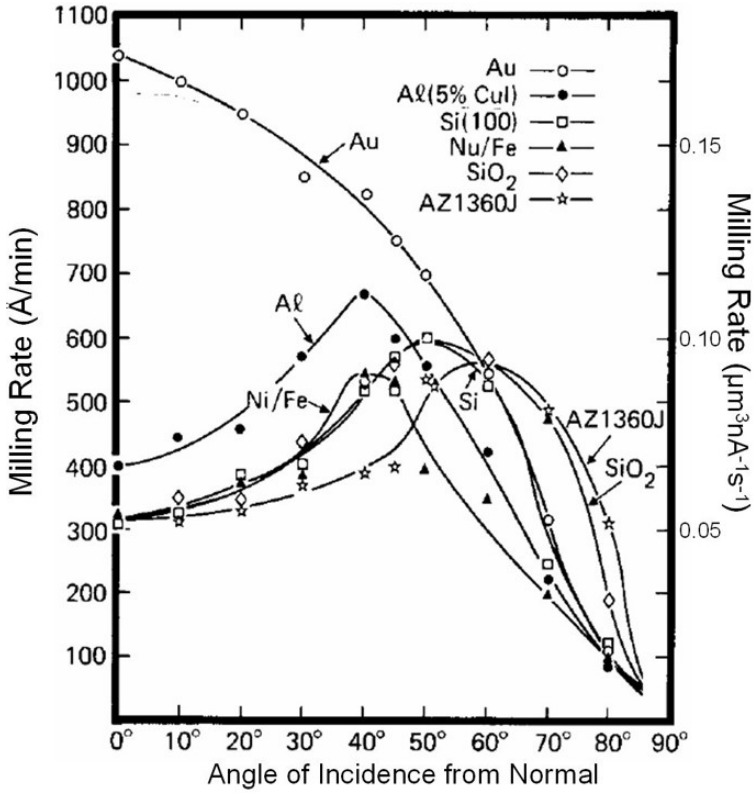

Figure 3.16. Ion milling rate versus incident beam angle for different materials [67].

Unlike RIE, ion mill is a perfect candidate for NNO stack etch. Ion mill is a physical etch technique that uses accelerated inert ions to hit the sample surface and thus remove the surface atoms. Since it's a physical etch process, the etch rate for most materials are very similar [68]. One thing that strongly affects the ion milling rate is the incident beam angle to the sample surface. Fig. 3.16 shows the relationship of incident beam angle with the milling rate for different materials. It is noted that incident beam angle between 30 °to 50 °shows the highest milling rate. However, a too high incident beam angle brings the uniformity problems near the milling edge as well as surface coating. Fig. 3.17 shows the stack residual problem because of angled milling. There are 1 μm wide stack residuals surrounding the beam stack, showing that around the beam the etching rate is smaller than open area. The adopted incident beam angle here is -30°, and a 3 μm thick photoresist is used as etch mask, making the 1 μm wide residual region reasonable.

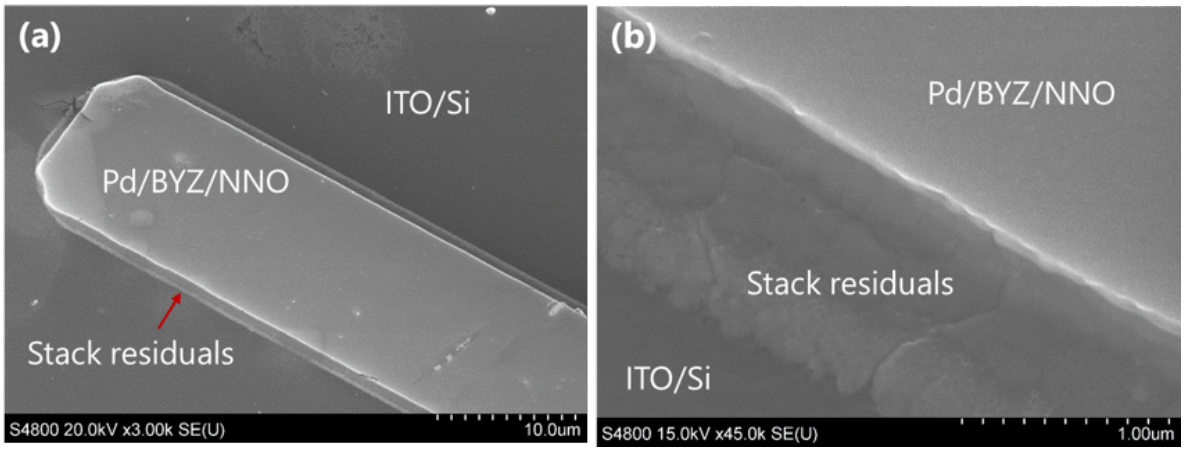

Figure 3.17. SEM images of etched Pd/BYZ/NNO stack. The zoomed in image of the residual stack is shown in (b).

To minimize the stack residual region, 30°incident beam angle is selected as the etch recipe. As for beam voltage, since NNO is a very hard material and difficult to etch, 600V bias is selected. The high voltage brings high energy ions, thus heats up the sample during milling, in such case a cooling process is added to avoid photoresist hardening. This part is discussed in section 2.5.2 in detail.

3.4.3 Substrate Release

Several Wet etch techniques are widely used in Si substrate release, including KOH (potassium hydroxide), EDP (ethylene diamene pyrocatechol), and TMAH (tetramethyl ammonium hydroxide) directional etch. Those alkaline chemicals show a preferential etching crystallographic direction along Si <100> and <11o>, while stop at <111> direction. This etch method is usually used by opening a large opening at backside, with a 54.74 ° angled directional etch to form released membranes at the top side, as shown in Fig. 3.18. SiN and SiO_2 layers are typically selected as the etch stop layer.

The KOH wet etch is a simple and low cost etch technology, however, it requires to etch all the way through the wafer, which requires a relatively long etch time and the resulted wafer is very fragile. Xenon difluoride (XeF_2) is another optional Si etching reagent that provides a gas phase isotropic dry etch of Si. XeF_2 etch shows high etch rate as large as 7000 Å/min at room temperature [69], and a high selectivity to photoresists, oxides, nitrides

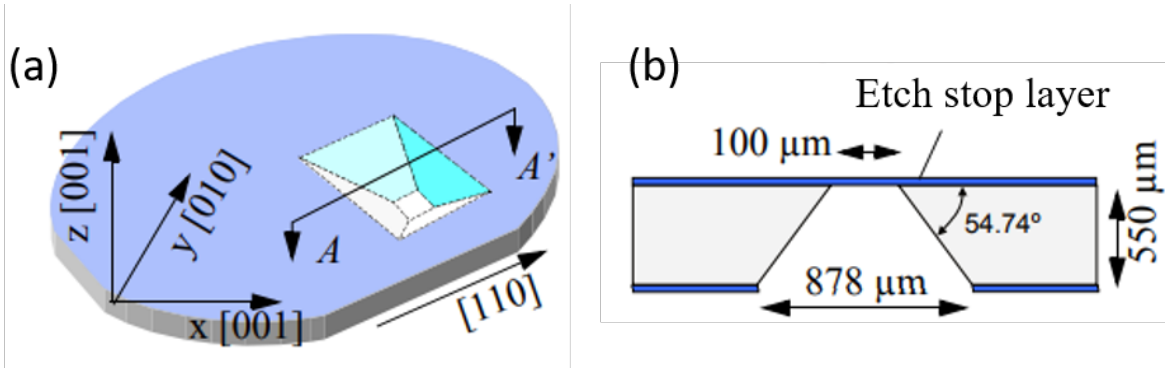

Figure 3.18. (a) crystallographic directions on a (100) Si wafer. (b) Schematic of KOH type wet etch for Si substrate release to form a membrane on the surface [65].

such frequently used masks. Besides, the gas phase etch avoids any solution treatment and prevents potential adhesion problems after release. If the sample is properly cleaned, there will be no side products or contaminants left after the etch process [70].

The etch rate of XeF_2 rate is highly depend on sevral parameters. Higher XeF_2 pressure, longer cycling time and a larger etch opening all results an increase in etch rate. Fig. 3.19 shows the Si etch rate as a function of opening size [71]. For a low XeF_2 pressure such as 1 Torr, the etch rate quickly saturated at 20 μm opening size, and gradually decreases with increasing opening size; while for higher XeF_2 pressure such as 3 Torr, the etch rate increases with an increasing opening size, and reached a maximum etch rate at opening size equals to 80 μm. As read from Fig. 3.19, a higher pressure brings a higher etch rate, and a larger saturation opening size.

For the NNO actuator layout, a variety of opening size is presented on the same chip, where a different etch rate is observed. Fig. 3.20(a) shows a NNO meander device after XeF_2 etch. The etch depth can be observed from how far the etch goes laterally since XeF_2 is a isotropic etch, with similar etch rate along all directions. After running etch cycles, the meander part is etched 24.25 μm deep, while the plate part with small etch holes (3 μm) is only etched 9.84 μm. To ensure no overetch occurs and at the same time all the components are released, a pre-calculated design for different etch openings is required.

Fig. 3.20(b) shows that crack happened when the device is etched too deep. The critical etch depth is highly dependent on stack mechanical properties such as stiffness,elasticity,

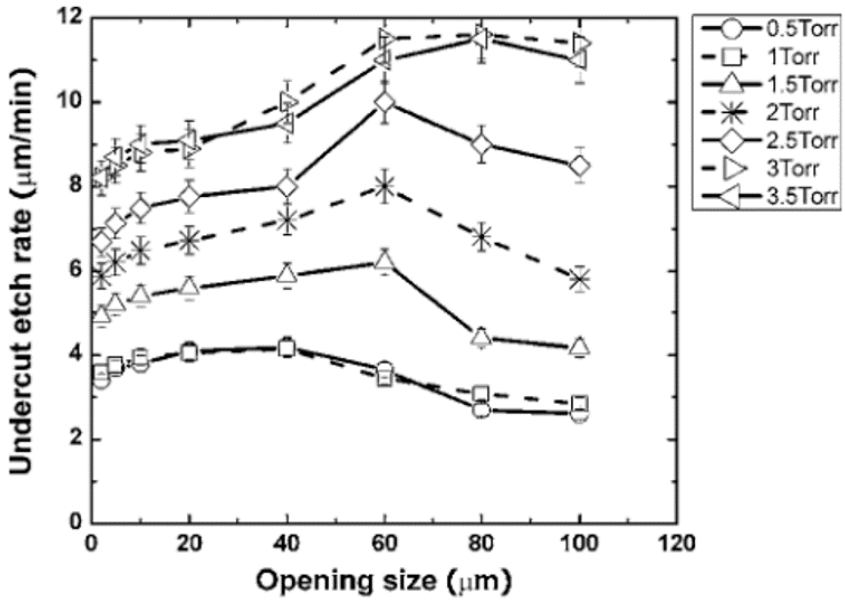

Figure 3.19. Si substrate etch rate as a function of opening size, with a variety of XeF_2 pressure from 0.5 to 3.5 Torr presented[71].

tensile strength, and elongation. For NNO stack, when etch depth exceeds 40 μm, cracks are observed on the released film.

3.5 Fabrication Process Optimization

3.5.1 Pd layer Patterning

The Pd layer acts as the catalyst for H_2 splitting which provides initial proton doping to the actuator. In this section we discuss the Pd layer patterning optimization. A new Pd layer patterning process is selected. In the old flow, the BYZ and NNO layers were patterned prior to Pd layer deposition. in this design Pd is patterned by lift-off, where the Pd electrode has to be 1-2 μm smaller than the lower layers to accommodate possible misalignment and avoid shorting to the bottom electrode. The Pd layer also exhibited some delamination during ultrasonic cleaning and H2 annealing. In the new design, the Pd, BYZ and NNO layers were all deposited first and mill the 3 layers together. Using the new design helped us maximize Pd coverage of the NNO surface, which allows to dope the NNO all the way to the edge of the actuator and increases the percentage of NNO phase transition during switching.

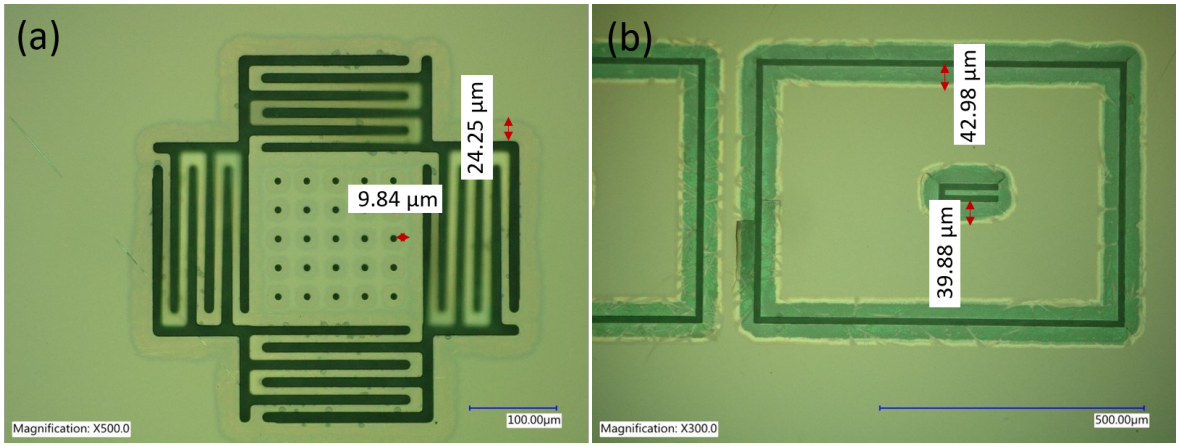

Figure 3.20. (a) NNO device after XeF_2 release. A different etch depth is observed at different etch openings. (b) Cracks started to appear when the XeF_2 etch depth is higher than 40 μm.

The old and new layer structure are shown in Fig. 3.21. In the new design using ion milling, Pd showed better adhesion to the underlying BYZ layer as compared with the old process.

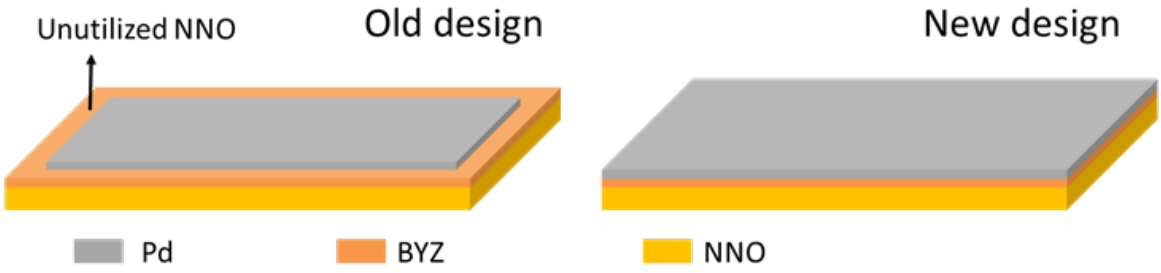

Figure 3.21. Comparison of the NNO actuator stack in old and new designs. Using simultaneous etch of all three layers with ion milling, the NNO surface is now fully covered with Pd, which ensures full doping of NNO.

3.5.2 Ion Milling Optimization

During ion mill, the inert ions carry a high energy, which heats up the sample during milling. The surface photoresist will be hardened if appropriate cooling process is not added. hardened photoresist is very difficult to remove from the sample, causing a surface contamination, and also influences surface reaction, as shown in Fig. 3.22.

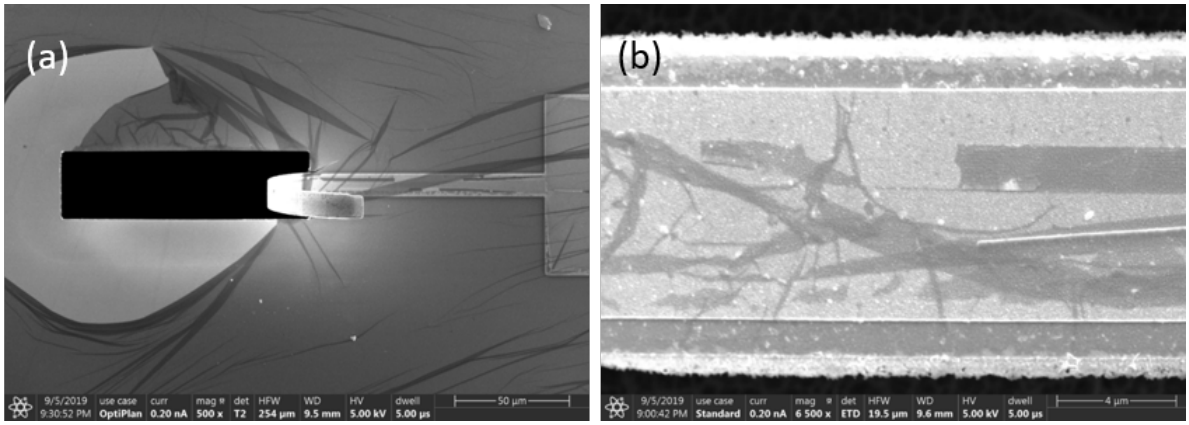

Figure 3.22. NNO actuator with hardened photoresist on sample surface after ion mill. (b) shows the zoomed in picture on the cantilever, there are also photoresist residuals that affects H_2 doping.

To eliminate the photoresist hardening, a series of steps are performed. Since the hardening of photoresist usually occurs on the top part, a thicker resist shows a better performance during ion mill. Besides, since the hardening is due to photoresist being heated during ion mill, a cooling process during ion mill could prevent the sample to be heated up. A pre UV curing step could also decrease the ion mill heating influence. O_2 plasma cleaning as well as ultrasonic cleaning can help with photoresist residual removal. The steps are summarized below:

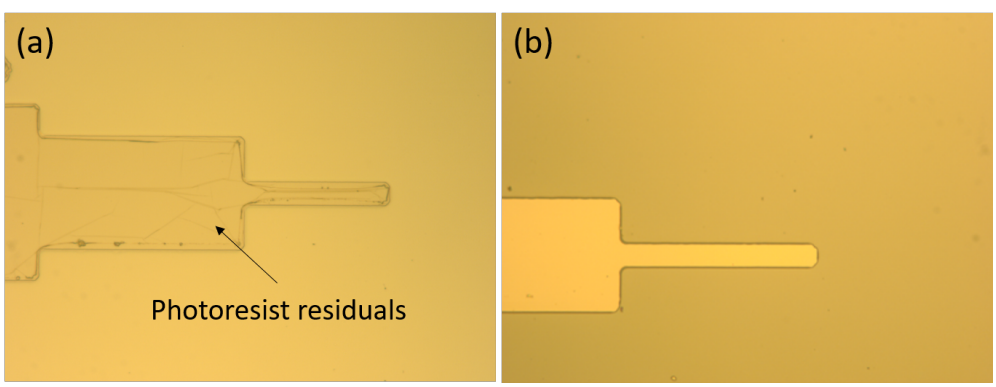

Figure 3.23. Optical images for NNO stack after ion mill and removing photoresist mask with (a) previous recipe and (b) optimized recipe. No photoresist residual is observed with optimized recipes.

- **Thicker resist:** With a thicker photoresist, only the top of the photoresist is compromised, while the intermediate photoresist is still able to dissolve in solvent, thus the burned out photoresist can be lifted off.

- **UV curing:** A 365nm UV curing process after photoresist development and before ion mill can greatly reduce the photoresist hardening. The UV curing dose we used is the same as the photoresist exposure.

- **Cooling cycle:** The mill is separated to individual cycles, and each cycle contains 1.5 min etch plus 7 mins cooling down. besides, there is 5 mins rest time between each cycle to make sure the samples has enough time to dissipate heat.

- **Post cleaning:** 7 min oxygen plasma cleaning (low power RIE O_2 etch) and 1 min ultrasonic cleaning is added to remove remaining photoresist residuals.

Adding all the steps mentioned above, there is no photoresist residuals appeared after ion mill, as shown in Fig. 3.23.

3.5.3 ITO Deposition Optimization

A poor ITO film quality causes a leaky dielectric layer as well as low induced stress during actuation. Due to this, an investigation of additional post-deposition anneals on ITO film quality is conducted. ITO was deposited via E-beam evaporator with a deposition rate of 2Å/s. Fig. 3.24 shows the SEM images of as deposited and annealed ITO films. Precipitates are uniformly generated in the surface of ITO film, which resulting a high surface roughness and causes front dielectric layers failing. Annealing process did lower ITO resistivity, but the surface morphology remained poor.

As shown in Fig. 3.24, the as deposited ITO shows a sheet resistance of 1.78 kΩ/sq, after anneal in air and O_2, the sheet resistance is down to 57.7 Ω/sq and 53.78 Ω/sq, respectively. While when annealed in N_2 atmosphere, the resulted sheet resistance is 32.97 Ω/sq, which is lower compared with air and O_2 atmosphere. All the annealing is conducted at 350 °C for 1 hour. This favors the explanation that ITO electrical conductivity comes from the

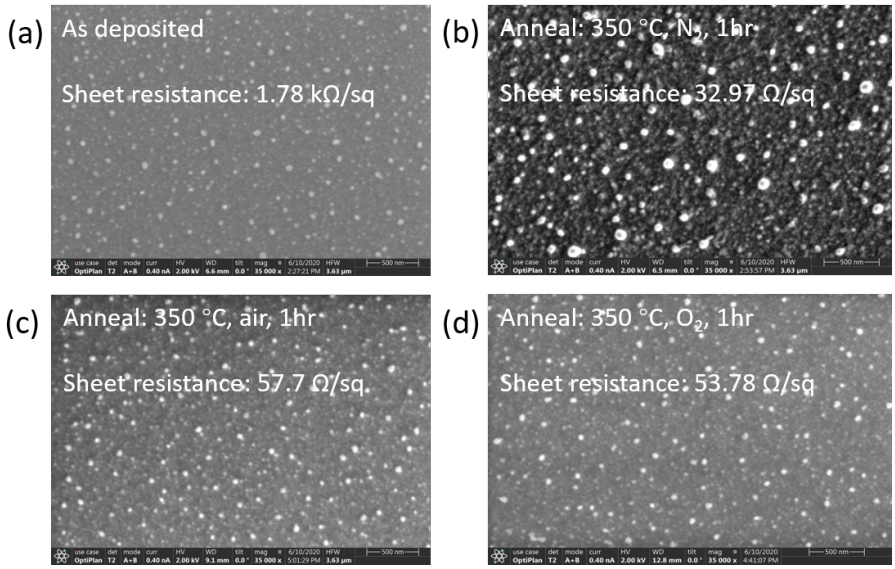

Figure 3.24. SEM images of (a) As deposited ITO film and annealed ITO film at 350C, 1 hour, in (b) N_2, (c) air, and (d) O_2 atmosphere. No significant morphology change is observed. ITO annealed in N_2 reached the lowest sheet resistance.

oxygen vacancy, and the O_2 in annealing atmosphere decreases the oxygen vacancies as well as carrier concentration, resulting a decrease of resistance.

Due to the surface roughness problems, ITO film by magnetron sputtering is considered as the candidate for NNO actuator. Fig. 3.25 shows the SEM image of as doposited and annealed 100nm ITO film. Unlike the poor surface morphology that the E-beam evaporated ITO, magnetron sputtered ITO shows a clean and flat surface, and no precipitations observed after anneal. Crystallization is shown in Fig. 3.25(b) with a grain boundary size of 100 nm, which makes sense for a 100 nm thick film. The sheet resistance is 105 Ω/sq after anneal in N2 at 350 °C for 1 hour, which larger than annealed E-beam evaporated ITO (32.97 Ω/sq), but it's still acceptable as a bottom electrode for NNO actuator. Fig. 3.26 shows the AFM image of annealed ITO film, with roughness RMS of 451.325 pm.

3.5.4 XeF_2 Anchor Release

Owning to the isotropic etch nature of XeF_2, the anchor of NNO actuator is released accompanied with the cantilever release, the SEM image is shown in Fig. 3.27. Without

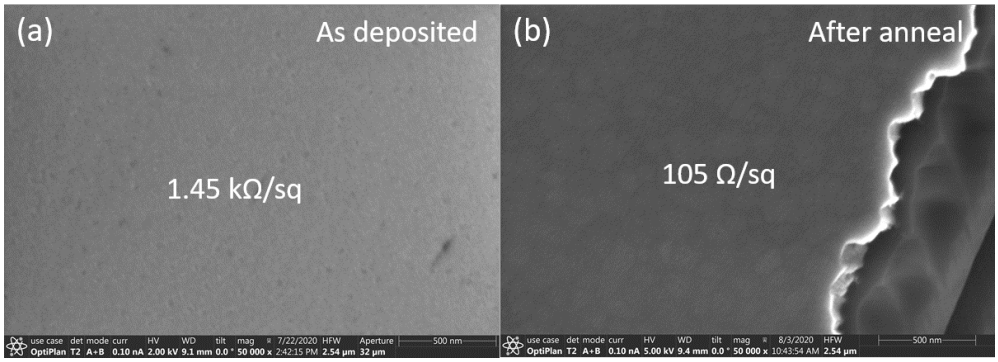

Figure 3.25. SEM images of magnetron sputtered ITO film, (a) as deposited and (b) annealed in N_2 at 350 °C for 1 hour.

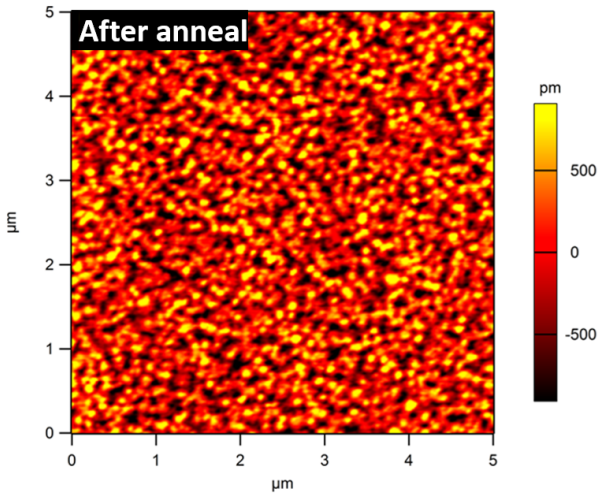

Figure 3.26. AFM image of magnetron sputtered ITO film. The roughness RMS is 451.325 pm.

substrate support, the anchor is bending downward due to the internal stress between ITO and SiN, and cracks formed in the corner of the released film. The bending down anchor takes the cantilever to the downside of the etch opening, when the opening is not deep enough, the cantilever deformation will be prevented. Moreover, the released anchor is not parallel to the sample, which increases the difficulty of cantilever deflection measurement.

To solve the anchor release problem, a two step substrate release is conducted. Instead of a single mask for both the ITO opening etch and XeF_2 release, a layout design with separate mask for ITO opening etch and XeF_2 substrate release near the anchor is shown in Fig. 3.28. Red layer shows the ITO etch opening, and this etch shapes the NNO actuator in

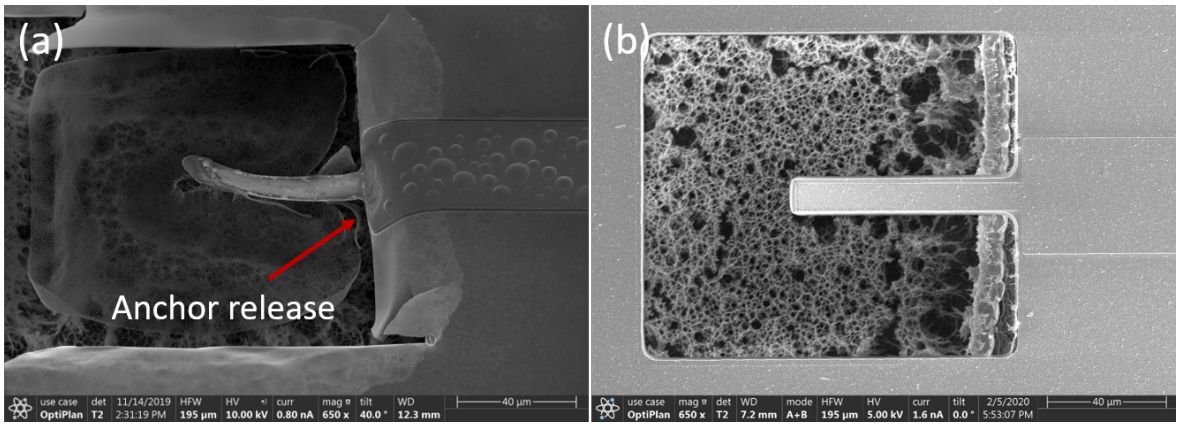

Figure 3.27. (a) released NNO actuator with a bending downward anchor, showing the anchor release problem. (b) released NNO actuator with double etch masks for ITO and Si etch to avoid anchor release.

ITO layer; green layer is the Si etch opening, which is farther away with the anchor compared with ITO etch opening. During Si XeF_2 etch, a lateral etch is accompanied with the depth etch based on XeF_2 isotropic nature, and the SEM image of released actuator is shown in Fig. 3.27(b). A step is observed near the anchor, showing a smaller etch depth near the anchor, and no anchor release is observed.

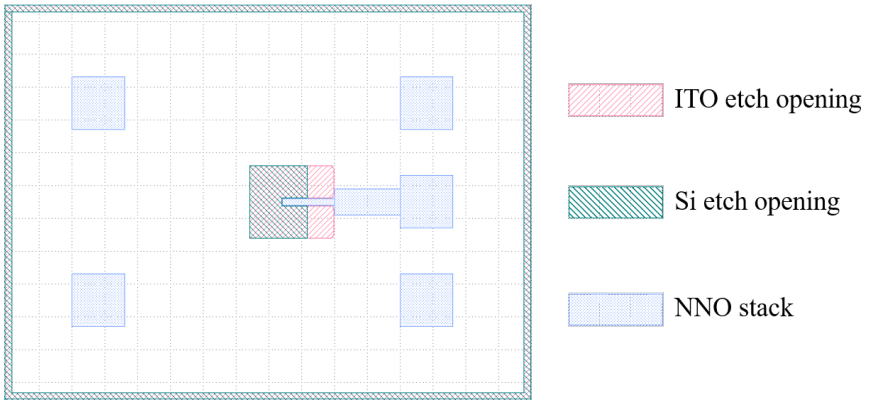

Figure 3.28. Layout design with separate ITO opening and Si opening to avoid anchor release.

4. NNO ACTUATOR WITH BYZ PROTON STORAGE LAYER

4.1 Actuator Design

In order to transfer the NNO lattice expansion to a cantilever deflection and enable a electrical driving mechanism, the NNO actuator is composed of 4 layers: two electrode layers, NNO layer, and BYZ layer, as shown in Fig. 4.1.

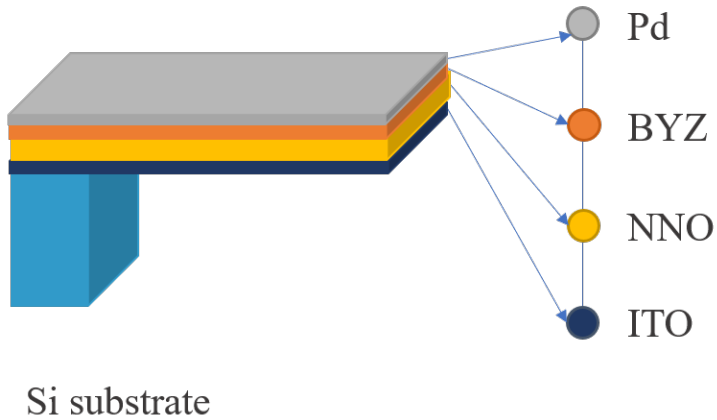

Figure 4.1. Schematic of NNO actuator layer stack.

Each layer has the following functions:

- **Pd** top electrode, catalyst of H_2, splitting H_2 into protons and electrons.
- **BYZ** dielectric layer that provides electric field to drive protons in electrical driven mechanism. Store protons as well.
- **NNO** Core material layer that provides strain during proton doping.
- **ITO** bottom electrode, resistant to rigorous annealing process of NNO.

To initialize the actuator and store proton in the film stack, the actuator is annealed in Ar balanced 5% H_2 atmosphere at 210 °C for 10 mins. Electron doping is accompanied when proton enters the NNO layer, and drives the NNO transition from metallic phase to insulating phase. The phase transition induces 6 orders of magnitude change in resistivity, 35% transimitivity change, and most importantly, 2.37% lattice expansion (6.9% volume

expansion). The lattice expansion in NNO induces strain to adjacent layers and causes actuator deflection. Since NNO is located in the down side of the actuator stack, a expansion in NNO causes a upward bending.

Fig. 4.2 shows the electrical driven mechanism in NNO actuator. The idea is to use bias added on Pd top electrode to control the proton movement. When protons are stored in BYZ layer by a negative bias, NNO is in pristine state with metallic phase; when positive bias added and protons are pushed into NNO layer, NNO shows the transition and lattice parameter expands by 2.37%, thus causes actuator deflection.

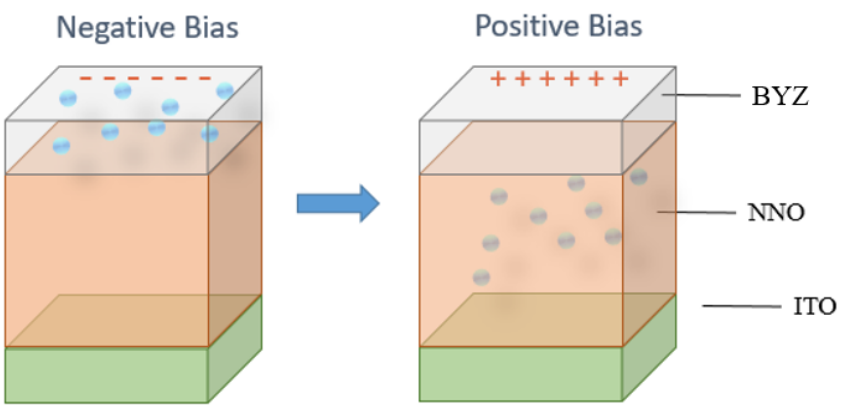

Figure 4.2. Schematic of electrical driven NNO actuation mechanism. Protons are moving back and forth to dope and undope NNO layer.

The process flow of NNO actuator is shown in Fig. 4.3. The selected substrate is Si (100) wafer. The bottom electrode ITO is evaporated via E-beam evaporation. Then 150 nm NNO is deposited by room temperature magnetron co-sputtering with Nd and Ni target, with 40 sccm Ar flow, 10 sccm O_2 flow under 5 mTorr chamber pressure. An annealing process is followed at 500 °C, 24 hours in air. After NNO annealing, 40 nm BYZ is deposited by magnetron sputtering at 550 °C, and top electrode50 nm Pd is evaporated by E-beam evaporation.

After thin film deposition, the fabrication of actuator is followed. The Pd/BYZ/NNO stack is patterned and etched by ion milling together with a photoresist etch mask. ITO layer is etched by ion milling as well, using the ITO opening layout design and photoresist as the etch mask. XeF_2 Si substrate releases uses the Si opening etch mask. After all the

etch task is done, photoresist is removed by Remover PG. Actuator is doped in Ar balanced 5% H_2 atmosphere at 210 °C for 10 mins to generate deflection.

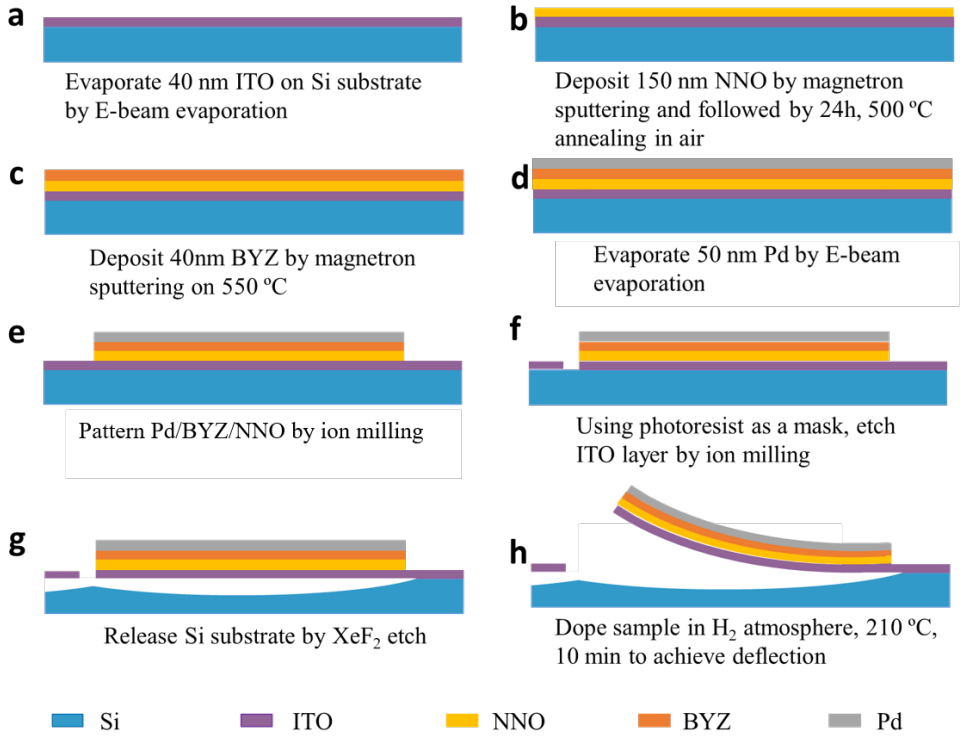

Figure 4.3. Process flow of NNO actuator with BYZ proton storage layer.

4.1.1 Doping Test

As described in Section 1.4, electron doping of NNO drives the MIT, where giant electrical, optical, and structural changes are accompanied. This makes NNO a competitive candidate for MEMS actuators. Fig. 4.4 shows the NNO XRD plot before and after proton doping. Here Fluorine doped Tin oxide (FTO) glass is used as the substrate. The reason here we choose FTO is because NNO XRD peak is overlapped with Si (200), while using FTO glass substrate is not. Using this substrate can help us define the exact position of NNO peak. Three peaks were observed for NNO, and their peaks shifted to left side after doping, indicating a lattice expansion happened during MIT.

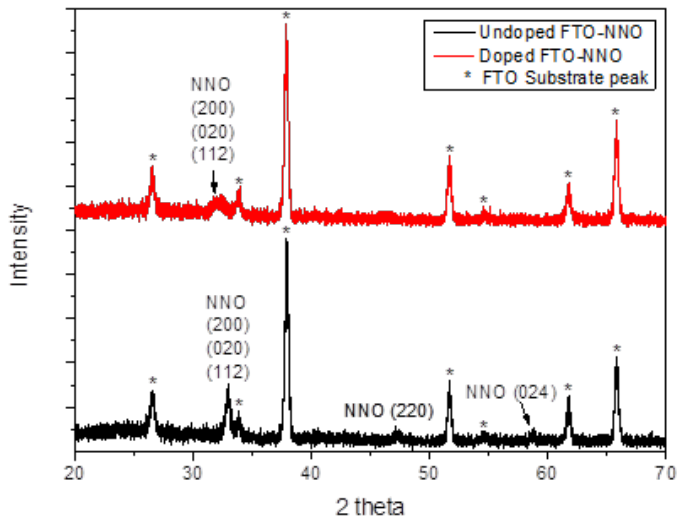

Figure 4.4. Schematic of standard perovskite ABX_3 cubic structure [1]

Pristine NNO is orthorhombic (*Pbnm*) crystal symmetry with lattice parameters a, b, and c of 5.45 Å, 5.44Å, and 7.70 Å, respectively. It is also called a pseudocubic structure, with the relation

$$a \approx b \approx \frac{c}{\sqrt{2}}. \tag{4.1}$$

After doping, peak (200)/(020)/(112) shifted from 32.84° to 32.06°. Back calculating the lattice parameter a from (200) peak, a increased from 5.45 to 5.57 during MIT, showing a 2.37% linear expansion. Considering the electron doping occurs in each nickel octahedra, an isotropic lattice expansion among NNO is expected. Treating the NNO structure as psudocubic, the volume expansion during MIT is estimated to be 6.9%.

4.1.2 Proton Storage Layer: BYZ

$Ba(Y_{0.8}Zr_{0.2})O_3$ (BYZ) is a widely used proton conductor dielectric material. It's a proton conductor but an electron insulator. In NNO actuator, BYZ layer is acted as a proton storage layer. When positive bias is applied, protons are pushed from BYZ layer to NNO layer; when negative bias is applied, protons are pull back to BYZ layer.

The BYZ layer was deposited at 550 °C by sputtering system. The morphology of as prepared BYZ/NNO/ITO stack is characterized by atomic force microscopy (AFM, Asylum Research) as shown in Fig. 4.5(a). The topography of BYZ/NNO/ITO stack shows flat surface with surface roughness of 2 nm, and with no clear signature of particles in the 1 μm region. X-ray diffraction pattern shows that as prepared BYZ, NNO and ITO thin film are polycrystalline, with no identifiable impurity diffraction peaks (Fig. 4.5(b)).

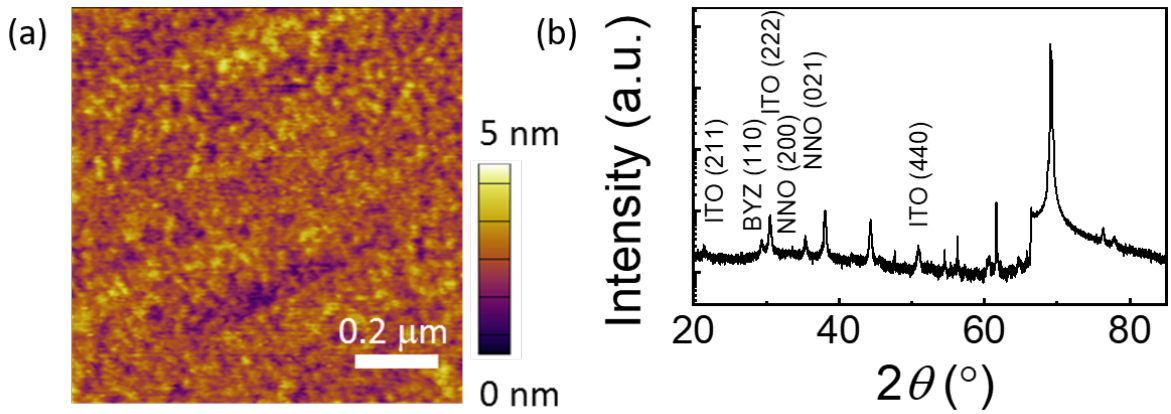

Figure 4.5. (a) The atomic force microscopy image of BYZ/NNO/ITO stack. (b) The x-ray diffraction pattern of BYZ/NNO/ITO stack. BYZ, NNO and ITO are labeled in the figure. Others without label are diffraction peaks from Si wafer and aluminum measurement setup.

To figure out an appropriate BYZ layer thickness as a dielectric layer, in plane resistance is measured for BYZ layer with varied thickness, as shown In Fig. 4.6. The resistance is measured between two parallel electrode bars with separation width 10 μm. The resistance for 10 nm, 40 nm, 70 nm BYZ are $3.5 \times 10^4\Omega$, $1.16 \times 10^6\Omega$, and $1.34 \times 10^{11}\Omega$ respectively. 10 nm BYZ is electrically leaky, while 40 nm and 70 nm BYZ performed well as a dielectric layer. For the 70 nm BYZ, the current measured is noise signal, as seen it didn't show a linear relationship with an increasing voltage.

To further discover the BYZ layer behavior in the thickness between 10 nm and 40 nm, a detailed vertical measurement is done for 20 nm, 30 nm, and 40 nm BYZ layer. The layer stack is shown in Fig. 4.7.

Pd serves as the opt electrode and ITO is the bottom electrode. The current flows vertically from Pd to BYZ, NNO then, ITO, giving a more accurate number of vertical

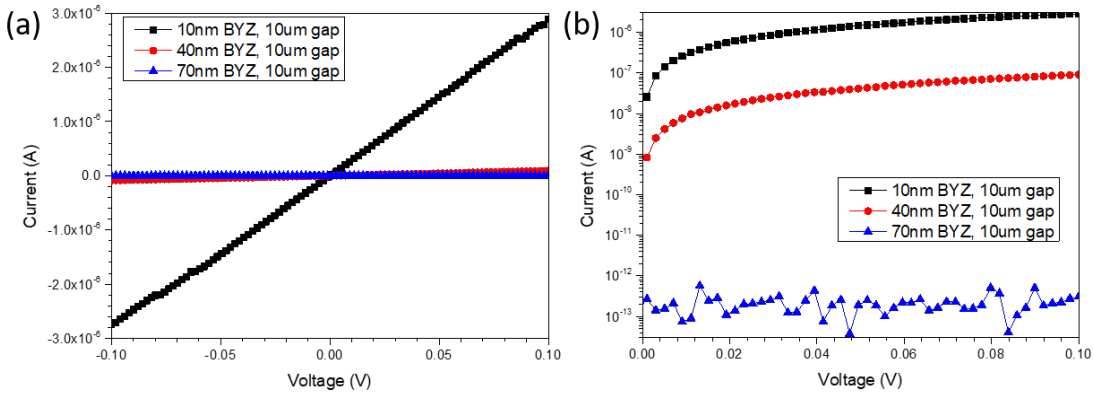

Figure 4.6. BYZ layer in plane resistance with varied layer thickness in (a) linear scale and (b) log scale.

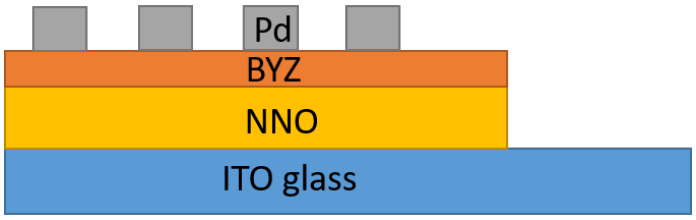

Figure 4.7. schematic of Pd-BYZ-NNO stack. Pd is the top electrode and ITO is the bottom electrode.

resistance and capacitance. A control sample with the stack Pd-NNO-ITO is tested to eliminate other layers' influence. The measured resistance and capacitance is shown in table 4.1

4.1.3 ITO Layer Thickness Adjustment

To maximize the deflection and remove stress neutral axis outside NNO layer, a series of ITO thickness is tried in COMSOL simulation. The cantilever deflection versus ITO thickness is shown in Fig. 4.8. Pd/BYZ/NNO layer is set as 50nm/40nm/150nm. Cantilever length is 35um. 2% expansion strain is added to NNO layer to simulate the phase transition induced deflection. It is observed that when ITO layer thickness is smaller than 80 nm, stress neutral axis is on top of NNO layer, making the whole cantilever bending upward. The trend of deflection with ITO thickness is shown in Fig. 4.8(a), where the thinner the

Table 4.1. BYZ Stack Resistance and Capacitance with Varied BYZ Thickness

BYZ thickness (nm)	Resistance Ω	Capacitance (pF)
20	1.37×10^6	133
30	4.97×10^6	96.5
40	6.62×10^6	36.5
0 (control sample)	70.2	-

ITO film, the larger the deflection. Considering ITO conductivity dramatically decreases when ITO thickness is smaller than 50 nm, 40 nm would be an appropriate ITO thickness for bending up case. For bending down case, thicker ITO film generates lager deflection with a decreasing trend, as shown in Fig. 4.8(b). Considering total film thickness, 150 nm is selected as the ITO thickness for bending down case.

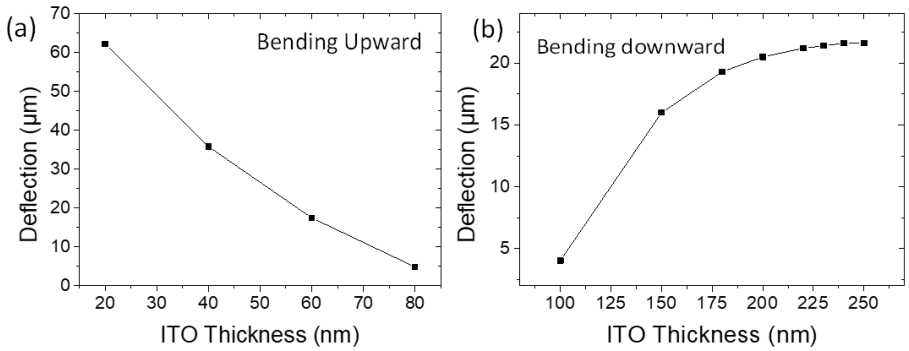

Figure 4.8. NNO stack cantilever deflection versus ITO layer thickness, calculated by COMSOL simulation. (a) Cantilever bends upward when ITO thickness is smaller than 80 nm; (b) Cantilever bends downward when ITO thickness is larger than 100 nm.

4.2 Characterization and Analysis

4.2.1 Deflection after Doping

The doping process is accomplished by Ar balanced 5 % H_2 anneal at 210 °C for 5 mins. The H_2 flow is set at 40 sccm. NNO layer expands with proton doping, leading the cantilever bending upward based on the stack configuration (with 40nm ITO). Fig. 4.9 shows the optical profilometer images of an NNO actuator before and after proton doping. The actuator dimension is 160 um long, 9 um wide, 0.48 um thick with the layer stack Pd/BYZ/NNO/ITO/SiN. Before doping, the actuator tip deflection to the anchor is -7.69 um, as shown in Fig. 4.9(a): the lower figure shows the x profile which across the actuator. while after proton doping, the tip deflection raised to 29.47 μm (Fig. 4.9(b)), indicating a 37.16 μm deflection. Using COMSOL simulation back calculating the induced strain, the 37.16 um deflection corresponds to 0.45% strain expansion toward the cantilever direction in the NNO layer.

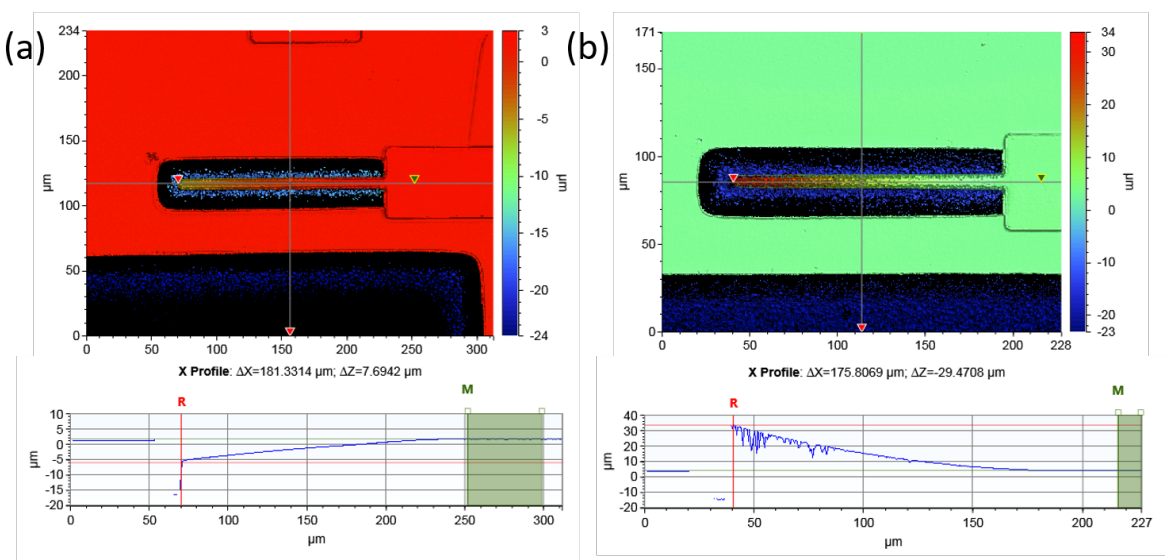

Figure 4.9. Optical profilometer images of a 160 um long, 9 um wide, 0.48 um thick actuator (a) before and (b) after proton doping.

4.2.2 Effects of Actuator Dimension

To study the effect of actuator dimension, NNO actuator with varied cantilever length (ranges from 20 μm to 200 μm) and width (ranges from 9 μm to 22 μm) is fabricated. All the actuators are on the same chip and fabricated together to make sure all the other conditions are equal. There are 72 released actuators in the matrix, and 33 of them showed response to the H_2 annealing and deflected upward. The largest deflection is 37.16 μm, achieved by device 3 with cantilever length = 160 μm and width = 9 μm, shown in Fig. 4.9. The cantilever tip deflection increases with increasing cantilever length as expected, except for the 200 μm long cantilever which showed a sudden decrease.

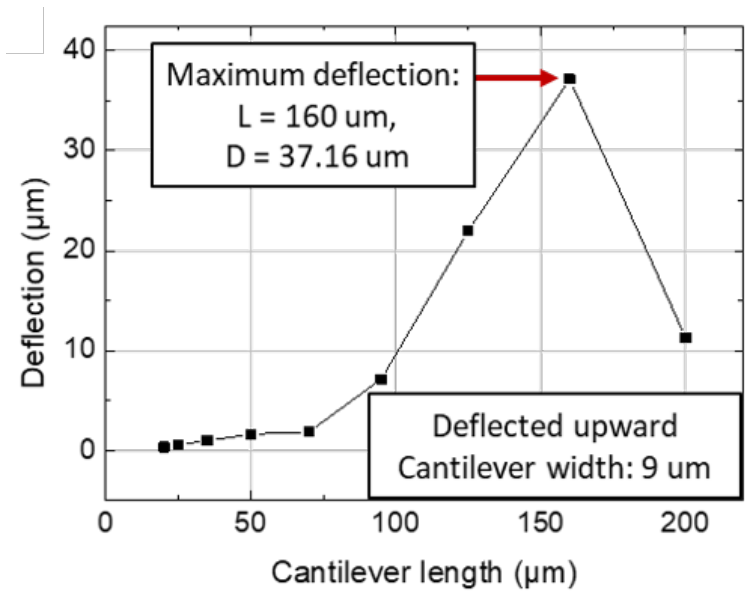

Figure 4.10. The measured cantilevers deflection D after H_2 doping. The cantilevers' width are 9 um, and the length L range from 20 to 200 μm.

To understand the deflection decrease happened at 200 μm cantilever, a 2D cantilever model with one side fixed is established in COMSOL to simulate the tip deflection with different cantilever length. 1% expansion strain is added to the NNO layer to generate deflection. When cantilever length is smaller than 140 μm, an increase of cantilever length results a larger deflection; while when cantilever length is longer than 140 μm, a decrease in deflection is observed. 140 um cantilever is found to be the optimized cantilever length that achieved the highest deflection. The deflected cantilever with 140 μm and 200 μm length

is shown in Fig. 4.11. 89.4 μm deflection is observed for the 140 μm cantilever, while for the 200 μm cantilever only 62.6 μm deflection is generated. This result explains why we obtained small deflection from the 200 μm long actuator.

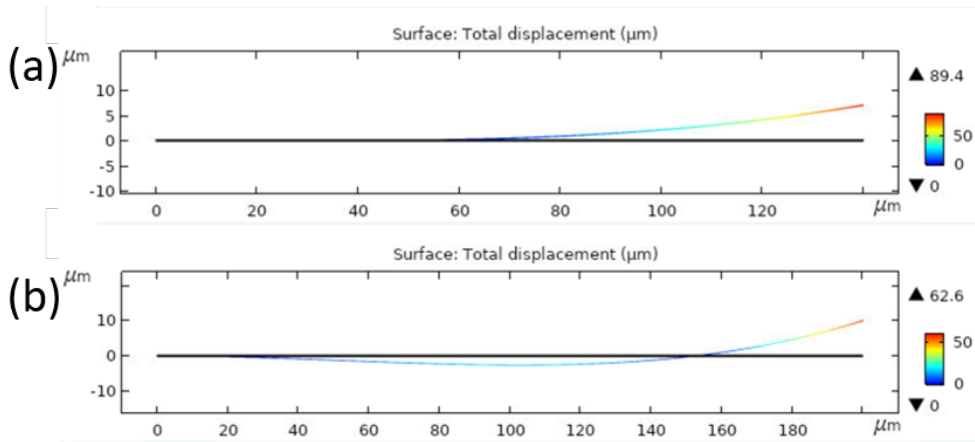

Figure 4.11. Simulated bending deflection of a 2D model by COMSOL with cantilever length of (a) 140 μm and (b) 200 μm, where 1% expansive strain is applied to NNO layer to generate deflection.

4.2.3 Doping Recovery Analysis

To analysis the doping and recovering process of the actuator, the deflection during the doping and recovering is measured, as shown in Fig. 4.12:

Since doping process requires a long time for heating and cooling, it's hard to accurately record the annealing time. From Fig. 4.12(a) we can see that the actuator started to saturate after 5 min H_2 anneal (the heating and cooling take about 25 min, and the device is placed in H_2 atmosphere during that period of time). 4 devices which owns relatively large deflection is recorded and showed the same trend. Geometrical parameters of the 4 devices is listed below:

The recovering process takes more time, after 1 hour annealing in air, the tip height returned to unbend state, but were not able return to initial downward bending state, shown in Fig. 4.12(b). From the result we confirmed that the doping caused deflection is repeatable and recoverable, and it gives us a basic idea about the required time for doping and recovery.

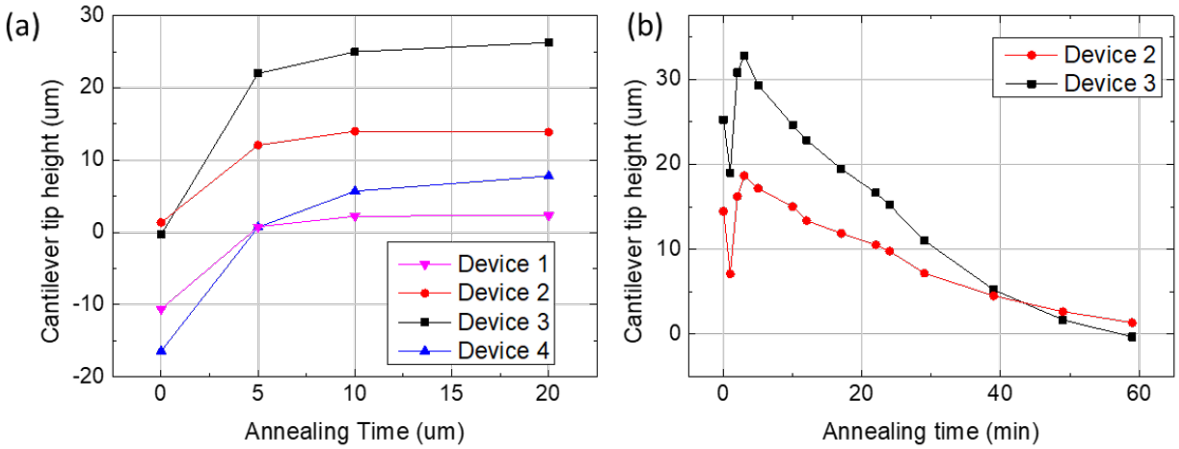

Figure 4.12. (a) Cantilever tip height change in the doping process when annealed in H_2, as a function of anneal time and (b) cantilever tip height change in the recovery process when annealed air. Device parameters are listed in Table. 4.2.

Table 4.2. Geometrical Parameters of Device 1-4

Device #	Cantilever length (μm)	Cantilever width (μm)
1	125	16
2	125	9
3	160	9
4	200	9

5. NNO ACTUATOR WITH OTHER LAYER STACKS

Despite the high strain and deflection of the actuator, one problem raised from the BYZ layer is the poor proton conductivity at room temperature. To better understand the the actuator performance, several stack actuators are fabricated and characterized for a optimized performance, including direct NNO acutator and stiffened NNO actuator.

5.1 Direct NNO Actuator Stack

5.1.1 Actuator Design

To get rid of proton diffusion problem raised from the BYZ layer, a Pd-NNO-ITO-SiN stack actuator is built. Without BYZ layer, Pd is the only layer on top of NNO, moving the NNO layer to the center of the stress neutral axis. While Pd is a metal layer with much lower young's modulus compared with other oxide layers, NNO falls under the stress neutral axis, which means doping will bend the cantilever downward (tensile stress from protons with a NNO layer lattice expansion). Besides, since only the Pd-NNO-ITO layer stack is not stiff enough, the strain induced from doping may cause the cantilever bending too much and generating cracks. In this case SiN bottom layer is added beneath ITO layer. The reason of choosing ITO as the bottom layer is because if SIN layer is added above ITO, the electrical connection among Pd, NNO and ITO is hard to build; if add SiN layer above NNO or Pd layer, proton diffusion is prohibited. On the other hand, the bottom SiN layer mechanically brings NNO away from stress neutral axis, resulting a higher transfer efficiency of NNO strain to deflection. The layer stack design of the actuator is shown in Fig. 5.1.

Without the proton storage layer BYZ, protons only move between Pd layer and NNO layer. Besides, since once NNO is back to pristine state, it transits from insulating phase to metallic phase. In metallic phase the Pd/NNO/ITO layer becomes a resistor and generates current flows from Pd to NNO and then to ITO. Two problem raises in this scenario: first, there is no voltage or very little voltage drop inside NNO layer, thus no bias to driving the proton moving; second, current flow generates heat and causes global heating. TO prevent these two problems, there should always be a part of NNO is doped, and the proton redistribution induced by voltage bias to generate cantilever deflection. Fig. 5.2 shows the

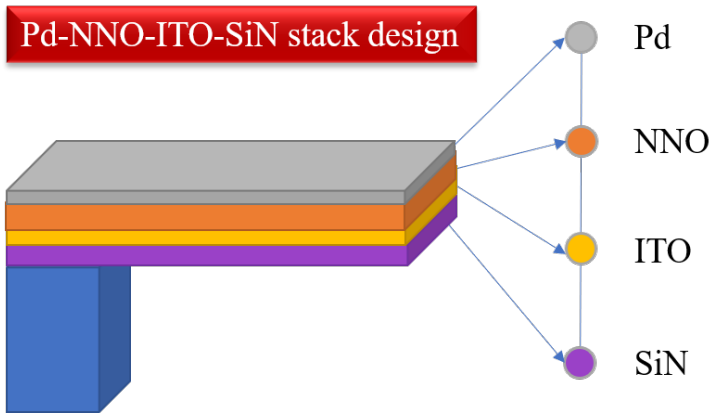

Figure 5.1. Schematic of NNO actuator layer stack.

schematic of pristine, doped and bias added NNO stack. When NNO stack is first time doped, protons uniformly spread in Pd layer and NNO layer, generating the NNO phase transition. lattice parameter expansion is accompanied and causing the cantilever to deflect. Once bias is added, protons redistributes inside the NNO layer. when protons gather in the top part of NNO, only the top NNO expands; while when protons gather in the bottom part of NNO, the bottom part shows the phase transition and expands.

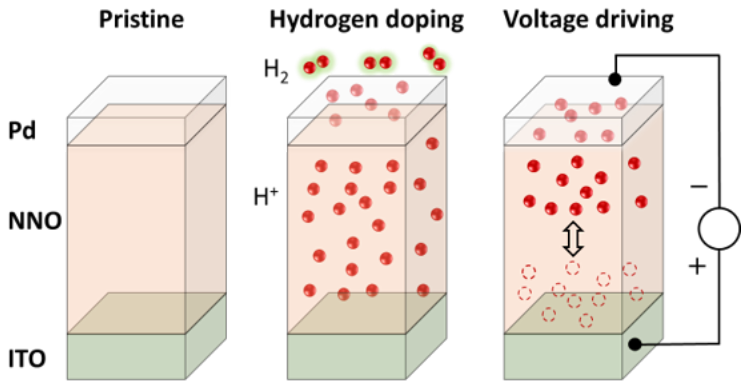

Figure 5.2. Proton distribution when bias is added to Pd layer. When NNO stack is first time doped, protons uniformly spread in Pd layer and NNO layer; when bias is added, protons redistributes inside the NNO layer.

5.1.2 Fabrication and Characterization

The fabrication process flow is shown in Fig. 4.3. Most of the thin film growth step is the same as the NNO actuator with BYZ proton storage layer, the difference is that instead of bare (100) Si wafer is selected as the substrate, here Si wafer with 200 nm low stress LPCVD SiN is selected. As for etch steps, Considering that SiN is pretty thick (200 nm), Reactive ion etch (RIE) is selected as the etch method for ITO and SiN layer. SiN is also a very good XeF_2 etch mask that protects front layers.

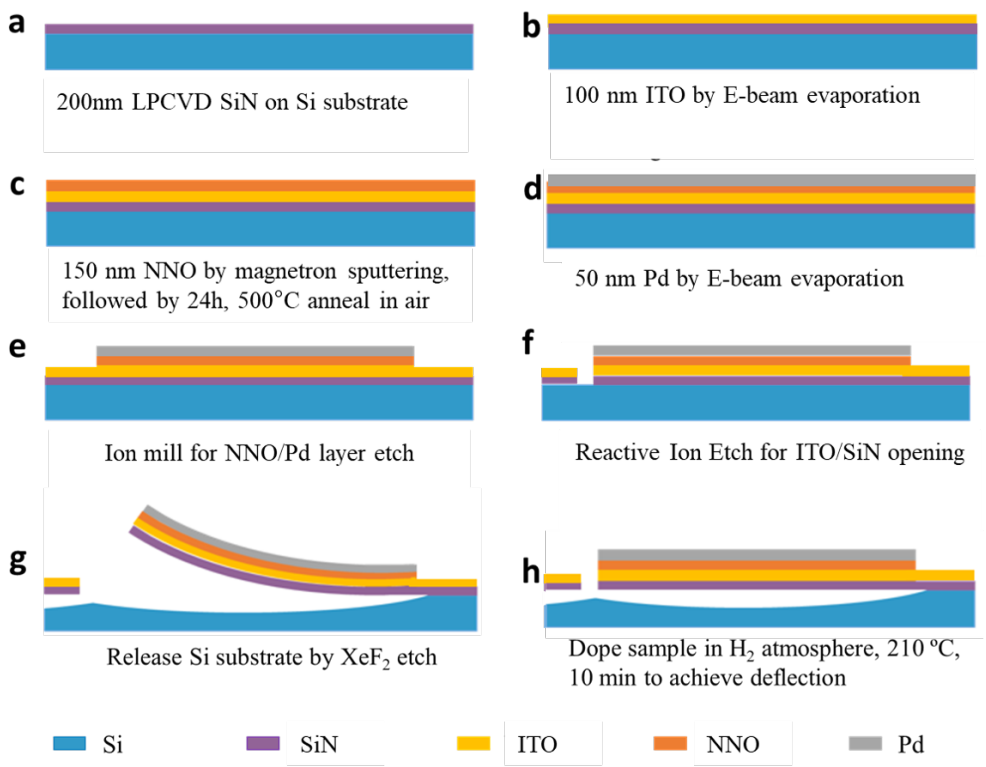

Figure 5.3. Pd-NNO-ITO-SiN stack NNO actuator fabrication process flow.

The SEM image of as fabricated NNO actuator is shown in Fig. 5.4(a). Owning to the initial stress in SiN layer as well as stress generated during annealing process, the cantilever curves up with a extremely tight radius of curvature (R=30 μm) at its pristine state. After doping the actuators in Ar balanced 5% H_2 atmosphere at 200 °C for 10 mins, the cantilevers flattened to a relatively low curvature (R=104 μm), as shown in Fig. 5.4(b). The transparent

thin films on top of the sample are hardened photoresist during ion milling, and this problem is discussed in section optimization.

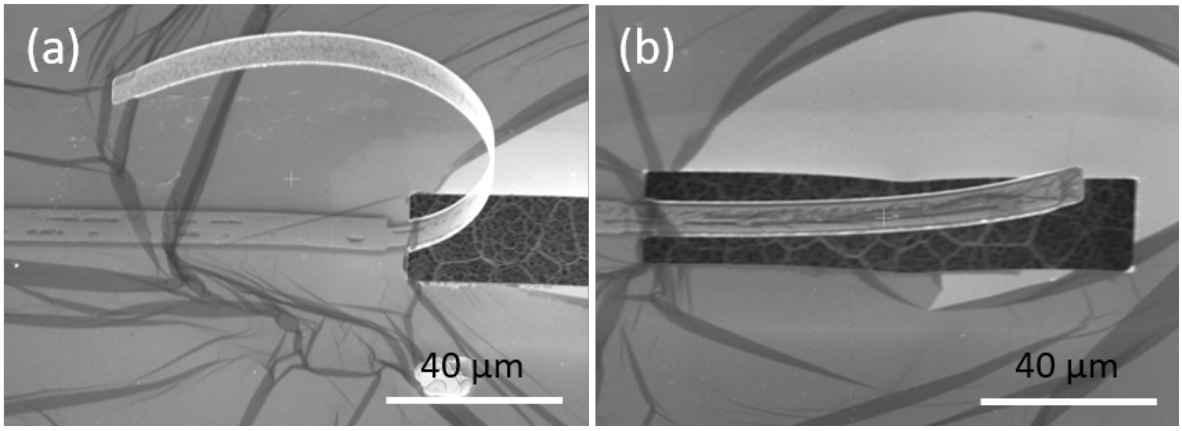

Figure 5.4. SEM images of (a) pristine and (b) proton doped Pd/NNO/ITO/SiN stack actuator.

5.1.3 Cantilever Deflection with Different Dimension

Cantilever dimensions varied from 5 μm to 20 μm in width, and 80 μm to 160 μm in length is studied in this section. Here we mainly discuss the influence of cantilever length. Fig. 5.5 (a)-(e) shows the actuator with different cantilever length before proton doping. The picture is captured by Keyence BZX-700 microscope with a 30° tilting angle. All the cantilevers are curved up with similar radius of curvature. The extremely large deflection makes them not able to get z-axis height from confocal microscope or optical profilometer.

The doping condition is Ar balanced 5% H_2 atmosphere, 200 °C for 10 mins. The optical images of doped cantilevers are shown in Fig. 5.5(f-g), with cantilever lengths range from 80 μm to 160 μm. After proton doping, all cantilevers deflected down, and no clear cracks were observed. The etch hole is only 40 μm deep, based on the fact that all cantilevers shows a similar tip height despite their different cantilever length, it is possible that the cantilever tip already touched the substrate, resulting a smaller measured deflection.

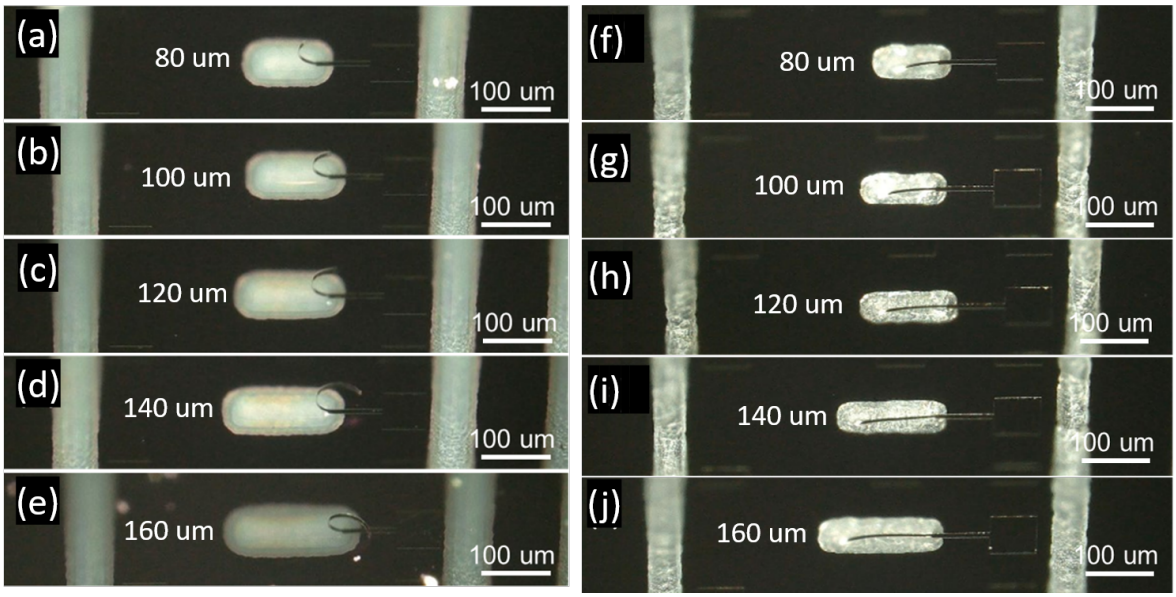

Figure 5.5. 30 °tilted optical images of (a-e) pristine cantilever and (f-j) proton doped Pd/NNO/ITO/SiN stack actuator.

5.1.4 DC Testing

To invastigate how DC bias drives the NNO actuator deflection, Keithley 2400 Source-Measure Unit is used for NNO actuator DC testing. the sample adopted for DC measurement is doped NNO actuator with Pd/NNO/ITO/SiN layer stack. Cycles of bias are added on actuator, and Fig. 5.6(a) shows a typical cycle with maximum voltage of 3 V.

There are 3 cycles of bias added to the actuator in total. The first cycle has a maximum voltage of 3 V. Cantilever remained straight and no deflection is observed via optical microscope. With no response observed in first bias cycle, the second cycle increased the maximum voltage to 5 V. From Fig. 5.6(b) the current started to increase, suggesting current leakage happened. At the same time the cantilever bends down sharply, and when voltage decreases the deflection didn't recover. This indicates that when 5 V bias is added, protons are pushed down, resulting a nonvolatile deflection. after the third bias cycle with maximum voltage if 5 V is added to the actuator, the cantilever has snapped upright, showing slight thermal displacement downward, and its resistance has further decreased. This indicates that the actuator has been back to the pristine state, since the leakage current heated up the device and protons are diffused out.

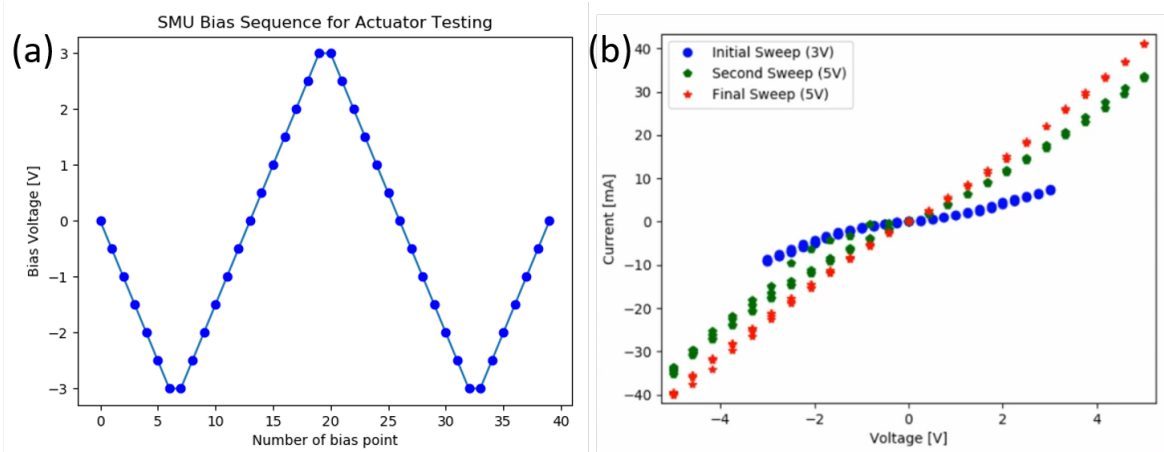

Figure 5.6. (a) Bias added to NNO actuator and (b) resulted leakage current once bias are added.

5.2 Stiffened NNO Actuator with Dielectric Layer

5.2.1 Acutator Design

The direct NNO actuator showed a extremely large deflection which is not ideal in actuation applications, and the design of no current limitation brought electrothermal heat up issues. To solve these problems a dielectric layer is introduced to the NNO layer stack. Considering that the electrical actuation process needs volatge drop on NNO layer, here ALD HfO_2 was chosen due to its comparable permittivity to NNO (20-25). To insure that most of the voltage drop is through cantilever region, 50nm SiO_2 is added underneath pad area. The same SiO_2 layer can also be used to increase stiffness in certain regions in and around the actuator, providing an added degree of freedom in actuator design and increasing stiffness in the anchor areas for higher yield.

The schematic of stiffened NNO actuator is shown in Fig. 5.7. Considering that the SiN initial stress and annealing induced stress still exist, the pristine state cantilever assumed to be bending up, just like the direct NNO actuator. in this stack, only Pd is on top of NNO, HfO_2, ITO and SiN are all beneath NNO, indicating that NNO is on top of the stress neutral axis. With proton doping induced NNO lattice expansion, the cantilever is expected to bend downward, shown in Fig. 5.7(b).

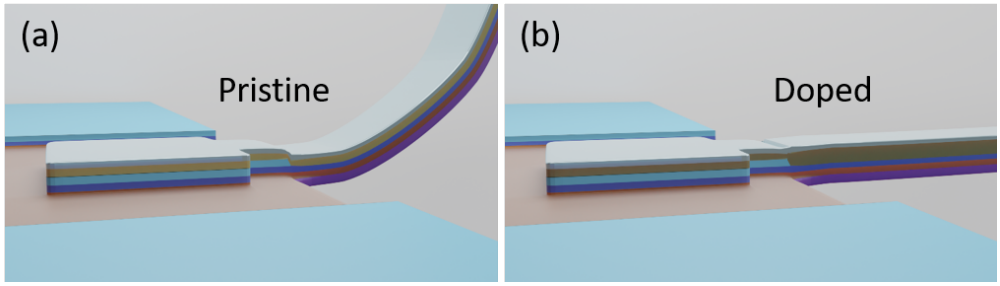

Figure 5.7. Schematics of (a) pristine and (b) proton doped stiffened NNO actuator. The initial inner stress resulted a bending up pristine state, and the doping induced strain generates a downward deflection.

5.2.2 Fabrication Process

Fig. 5.8 shows the process flow of the stiffened NNO actuator. The SiN layer is thickened to 400 nm to increase cantilever stiffness. After 50 nm ITO is deposited, an extra RTA (Rapid Thermal Annealing) is performed at 500° for 5min to crystallize and stabilize ITO. Then 50 nm thermal HfO_2 is deposited via ALD (Atomic Layer Deposition) at 200 °C. SiO_2 is evaporated via E-beam evaporator, patterned by lift-off to get desired layout. The NNO and Pd deposition process is the same as NNO actuators described previously. HfO_2 layer is etched together with NNO and Pd by ion mill. ITO and SiN layer are etched by RIE. Then XeF_2 is selected for Si substrate release.

The as fabricated cantilever is shown in Fig. 5.9. The SEM images were captured by FEI Apreo SEM with 30° tilted to observe the deflection. Before doping, NNO actuator was bending up, which is the same as the direct NNO actuator; after doping, cantilever bent down with a smaller deflection compared with the direct NNO actuator as designed. The deflection generated in stiffened NNO actuator is capable to profilometer z-axis measurement, enabling a quantitative analysis of actuator deflection performance.

With an appropriate cantilever tip height that enables light focus on the cantilever tip, the cantilever deflection before and after doping is measured by optical profilometer. Summarizing deflection data with varied cantilever dimensions, the deflection as a function of Cantilever length from 30 μm to 80 μm is shown in Fig. 5.10. A longer cantilever results

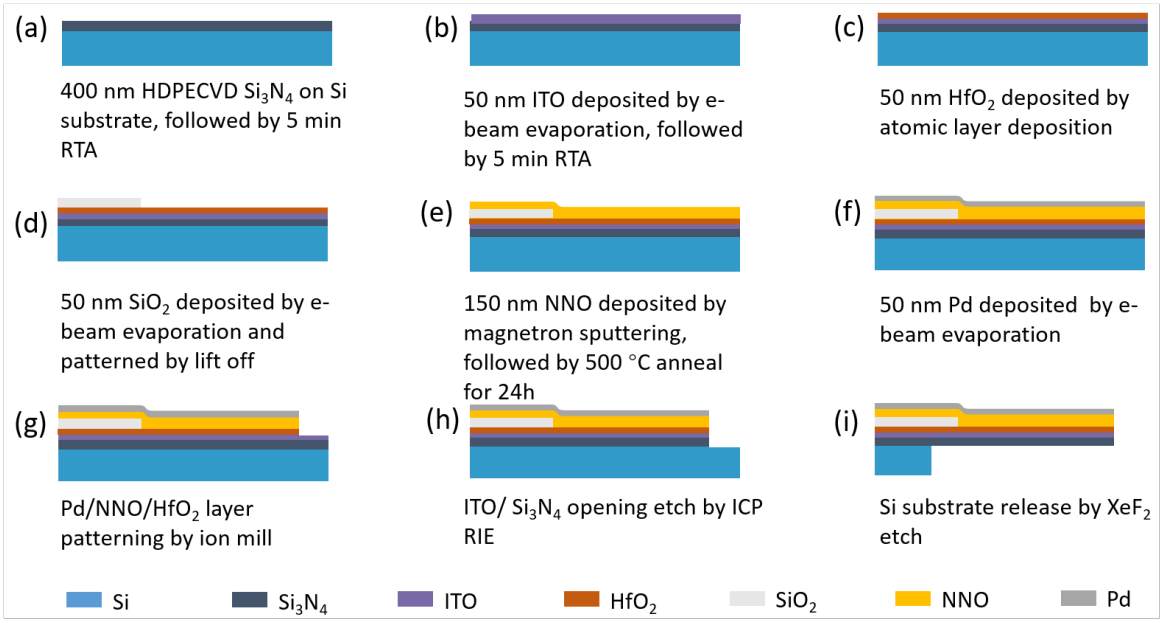

Figure 5.8. Fabrication process flow of stiffened NNO actuator.

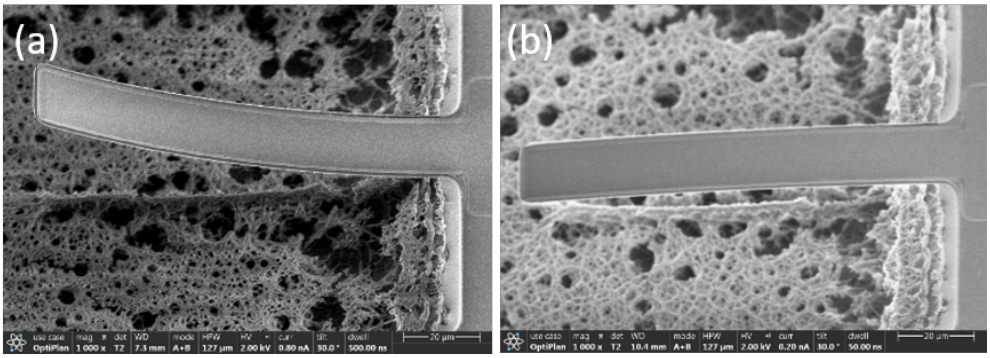

Figure 5.9. 30° tilted SEM images of (a) pristine and (b) proton doped stiffened NNO actuator.

a larger deflection, and the difference between varied cantilever width is very small. Wider beams exhibit lower tip displacements due to lateral curling.

The cantilevers exhibited lower work output performance compared to the first highly curved cantilever, as shown in Table. 5.1. This is believed to be due to growth issues with the ITO layer in the second fabrication run. Even so, FEA modelling estimates the NNO work density, U_{NNO}, to still be an extremely high 1.04 J/cm^3, corresponding to a cantilever work density, U_{tot}, of 0.21 J/cm^3.

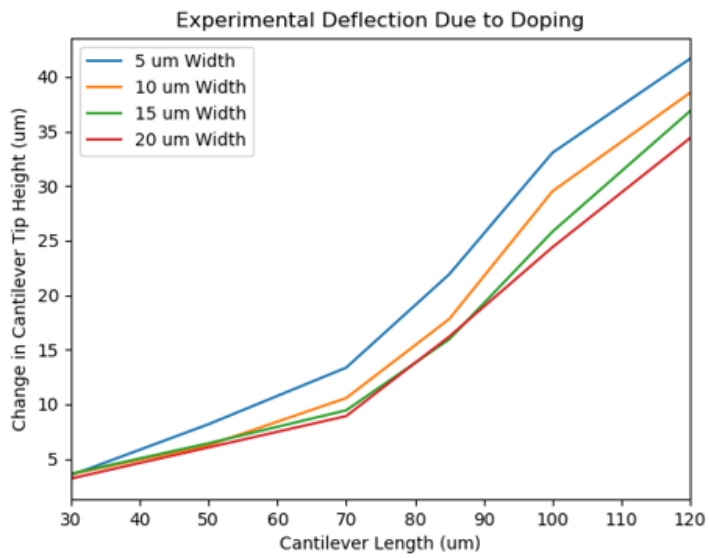

Figure 5.10. Stiffened NNO actuator deflection as a function of cantilever length, with cantilever width varied from 5 μm to 20 μm.

Table 5.1. Stiffened Cantilever Set Deflection Results

Length(μm)	30	50	70	85	100	120	Avg	Std
δY	3.5	8.2	13.4	21.9	33.1	41.7	N/A	N/A
W_{tot} **(pJ)**	33	40	39	60	86	801	N/A	N/A
U_{NNO} **(J/cm^3)**	1.48	1.06	0.74	0.94	1.14	0.89	1.04	0.23
U_{tot} **(J/cm^3)**	0.30	0.22	0.15	0.19	0.23	0.18	0.21	0.05

5.3 NNO Actuator Analysis

5.3.1 Work Density Calculation

The total elastic work along the cantilever length in all layers was computed by integrating the elastic strain energy over the entire cross sectional area. This integral also extends along the width of the beam by assuming E, ϵ_{xx}, and σ_{xx} are uniform in the Z direction. V is the entire volume of the cantilever in the x, y, and z directions. Using this method

the stresses and strains within the cantilever were calculated and the total work computed using the equation below:

$$W_{total} = \int_V \frac{1}{2} E(x,y)\sigma_{xx}(x,y)\epsilon_{xx}(x,y)dxdydz \tag{5.1}$$

To compute the maximum work density of the NNO actuating layer this total work is divided only by the volume of the NNO, (V_{NNO}).

$$U_{NNO} = W_{total}/V_{NNO} \tag{5.2}$$

This particular calculation allows for an estimate regarding the upper bounds of the NNO performance as an actuating material without particular regard for the exact configuration of the rest of the material stack, which will change depending on the actuator design. If the work densities of these cantilevers as micro-actuators are desired, one would divide by the total volume of the entire cantilever, $V_{cantilever}$:

$$U_{tot} = W_{total}/V_{cantilever} \tag{5.3}$$

5.3.2 Work Measurement Using Wafer Bow

To measure the work done by NNO proton doping, wafer bow measurement for pristine and doped NNO on Si substrate is conducted. The film stack uses 424 μm highly doped (100) Si wafer as conducting substrate, then 50 nm HfO_2 is deposited by ALD as a dielectric layer. 150 nm NNO is deposited via magnetron sputtering, followed by 50 nm Pd as the top electrode as well as H_2 split catalyst. Wafer bow was measured using Toho FLX-2023-S, and the prinstine NNO stack on wafer shows a reference radius of curvature of 32 m. Then the sample was doped in Ar balanced 5% H_2 atmosphere for 10 mins at 200 °C, and the radius of curvature reduced to -69 m, yielding a change of -100.5 m. Stoney equation is widely used in transferring film radius of curvature to film stress:

$$\sigma_f = \frac{E_s t_s^2}{6Rt_f} \tag{5.4}$$

The parameters are listed below:

- E_s substrate Young's modulus
- t_s thickness of the substrate
- R wafer radius of curvature
- t_f NNO film thickness

HfO_2 and Pd layer here are neglected since they are thin enough. Converting from radius of curvature to film stress and setting the pristine NNO as 0 stress point, wafer after proton doping shows a stress of 1.19 GPa. After proton doping the sample is annealed in air to diffuse protons out and see how the stress changes. The wafer was then subjected to five separate one minute intervals at 200 °C on a hotplate, with wafer bow remeasured after each minute to view the strain relaxation in the NNO as hydrogen dopant was driven out. Fig. 5.11 shows the doped film stress as a function of out diffusion annealing time at 200 °C, indicating that the rate of stress relaxation is rapid within the first minute and then slows as time goes on, with the stress at 5 min being -333 MPa.

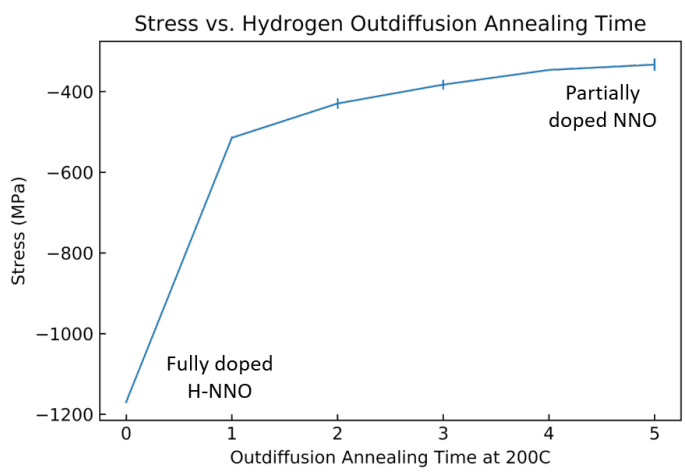

Figure 5.11. Film stress as a function of proton outdiffusion annealing time at 200 °C.

5.3.3 COMSOL Finite Element Analysis

Finite element modeling (FEM) was carried out with COMSOL multiphysics software version 5.4 with the structural mechanics module. The deflections of the set of stiffened cantilevers with lengths ranging from 30 to 120 μm was modeled in 2D. In order to model the extreme curvatures and strains exhibited by the experimental devices, techniques for nonlinear geometry were implemented to assist in convergence. [72] This model was then compared with the experimentally measured tip deflections. The model used assumes an isotropic expansion of the NNO during doping and is fit to experimental data taken at room temperature.

Fitting the direct NNO actuator with Pd/NNO/ITO/SiN stack, The COMSOL-simulated NNO strain upon doping was modeled as an isotropic expansion up to 1.5%, with the value increased until the radius of curvature matched the experimentally observed curvatures. the work done by this curved cantilever was found to be: 705 pJ. This value corresponds to an NNO work density of $U_{NNO} = 6.7$ J/cm^3, and an actuator work density of $U_{tot} = 1.4$ J/cm^3.

To better understand the NNO actuator performance with varied cantilever dimensions, The simulation adopted the film stack of the NNO actuator of 50 nm Pd/150 nm NNO/100 nm ITO/200 nm SiN to fit the experimental deflection data with different cantilever dimension. The COMSOL-simulated NNO strain upon doping was modeled as an isotropic expansion up to 1.5%, with the value increased until the radius of curvature matched the experimentally observed curvatures, as shown in Fig. 5.12(a). Setting 1.5% lattice expansion as 100% doping, 0 doping to 100% doping is simulated. 20% doping shows the best fitting with experimental results, suggesting the NNO induced strain is 0.285% for a 5 μm wide beam.

Fig. 5.12(b) shows the 2D COMSOL simulation fitting with optical profilometry results of cantilever tip displacement after proton doping. with all the cantilever lengths, the simulated deflection maintained an excellent fit with experimental results. The experimental data used in Fig. 5.12(a) is with 10 μm cantilever width, and 0.285% strain is obtained; the purple dashed line in Fig. 5.12(b) simulates the 5 μm wide, cantilever, showing a strain of 0.43%.

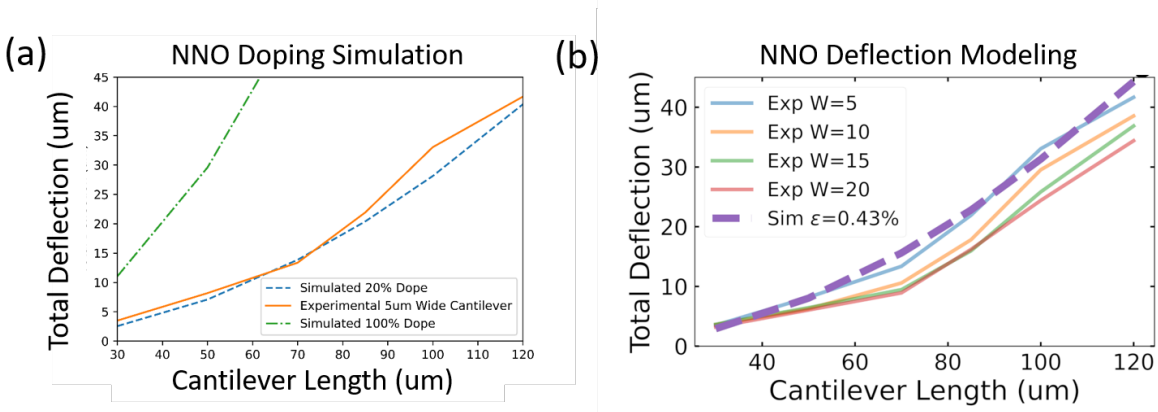

Figure 5.12. (a) setting 1.5% lattice expansion as 100% doping, simulated results of 20% doping shows a perfect match with experimental results. (b) 2D COMSOL simulation fitting with optical profilometry results of cantilever tip displacement after proton doping.

5.3.4 Mechanical Modeling of Loaded Cantilever

The theoretical total work generated during actuation is calculated by:

$$W = \frac{1}{2}E\epsilon^2 \tag{5.5}$$

Plugging in NNO stack parameters, the total wrok is 16.81 nJ at unconstrained expansion. Dividing the work only by the NNO layer volume, the material work density is 20.25 J/cm^3; Dividing the work by the whole cantilever volume, the output work density is 1.04 J/cm^3.

To find the blocking force of the actuator, a 2D FEA Model assuming 1.5% strain in the NNO upon doping is established. A 50 μm long and 10 μm wide cantilever with the same material stack as the stiffened cantilever set was utilized. The simulations demonstrated an exceptional blocking force of 0.05 mN and a displacement of 25 μm, as shown in Fig. 5.13. The work done on the simulated load is calculated to be 364 pJ, corresponding to a output NNO work density of 2.94 J/cm^3, and an actuator work density of 0.60 J/cm^3 .

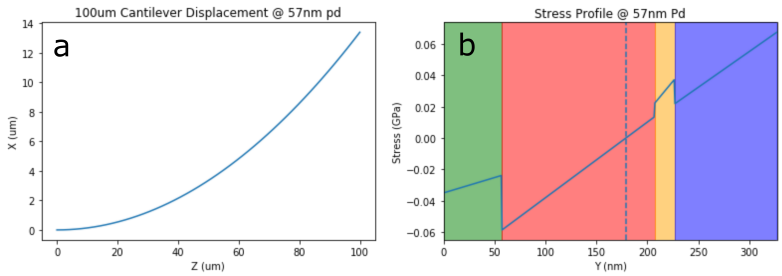

Figure 5.13. COMSOL simulated result of Cantilever tip deflection versus loading force.

5.3.5 Comparison to Alternative MEMS Actuator Materials

NNO actuator shows a fantastic performance with work density based on its high Young's modulus as well as giant strain introduced during doping. Wafer bow volumetric work density is lower than other estimates due to the load (Si wch$_a fer)beingextremelyhighfortheNNOfilm$

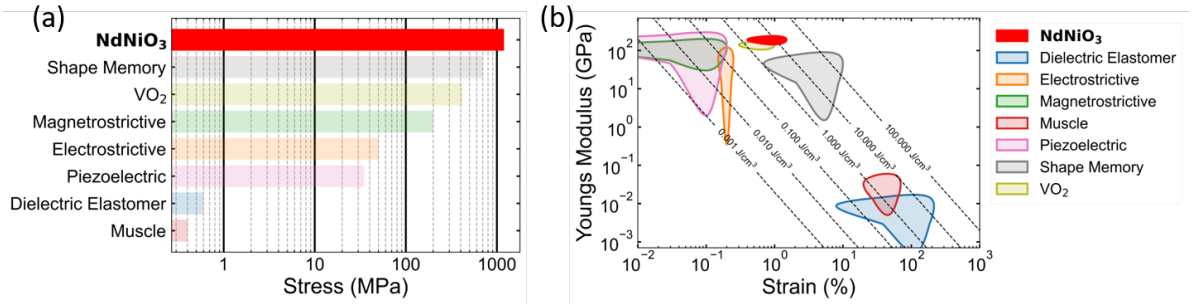

Figure 5.14. (a) Demonstrated stress in NNO film due to phase transition surpasses values reported for other actuator technologies. (b) Plot of material modulus and measured strain for NNO and other popular actuator materials, with theoretical maximum work density for given strains and moduli [73]–[83]

6. VERTICAL VO_2 MEMS ACTUATOR [84]

6.1 Introduction

Nowadays with the development of micro and nanotechnologies, there is a growing interest in micro actuation systems with phase transition materials which can provide large deflection amplitude, fast response, high force output and long duration. Among these materials, VO_2 is a promising candidate whose phase transition behavior has been studied since 1950's [85]. Vanadium dioxide (VO_2) undergoes an metal-insulator transition (MIT) from a monoclinic phase (insulating, M phase) to rutile phase (metallic, R phase) at around 68 °C with abrupt electrical, optical, and lattice structure changes. The structural change of VO_2 generates a giant, rapid, repeatable strain during the phase transition, which has created interest in exploring VO_2-based electronics and MEMS actuators for micro-robotics [86]–[89].

6.1.1 VO_2 Material Properties

In 1959, Morin [90] first reported the MIT of VO_2 was due to the change of inner crystal structure. In room temperature, VO_2(M) is monoclinic phase and act as a semiconductor with large resistance and high transmittance, while when the temperature is higher than 68 °C, VO_2 changes to rutile phase which act as a metal with lower resistance and lower transmittance. The linear V-V chains in VO_2(R) distorted to the zigzag chains in VO_2(M)[91] and induced the fully reversible MIT. The status of the outer 3d electrons in VO_2 are based on the electron-electron correlation strengths of the cation-cation interactions. Here is a critical separation value ($R_c = 0.293 \pm 0.004$ nm) of the 3d electron coupling interaction in VO_2: the 3d electrons are localized when the separation value R is larger than R_c, and the electrons are itinerant when R is smaller than R_c [92].

Figure 6.1 shows the atomic structures of monoclinic and rutile phase VO_2. the red atoms are oxygen and white atoms are vanadium. The V-V distance between VO_2(M) is about 0.316 nm and 0.262 nm as shown in Fig. 6.1(a), the first one is much larger than the critical V-V interaction distance (0.294 nm), so the d-orbital electrons are localized, and because of lack of itinerant electrons, VO_2(M) performs as a semiconductor [93]. To the

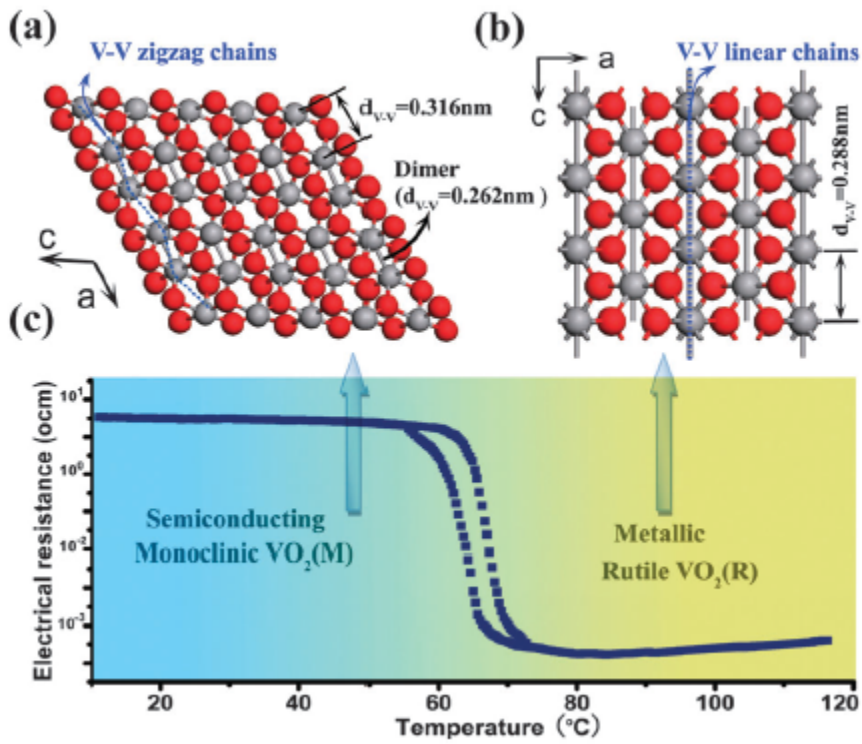

Figure 6.1. Atomic crystal structure of (a) monoclinic and (b) rutile VO_2. (c) shows the electrical resistance of VO_2 near the phase transition temperature.

contrary, as shown in Fig. 6.1(b), the V-V distance between VO_2(R) is about 0.288 nm, which is smaller than 0.294 nm, indicating the d-orbital electrons are shared by all of the nearby V atoms, thus giving a metallic VO_2(R) [94].

In its low-temperature phase, VO_2 has lattice parameters of $a_M = 5.755$ Å, $b_M = 4.526$ Å, and $c_M = 5.384$ Å, corresponding to a unit cell volume of 118.11 ^{3}[95]. Above the phase transition temperature, the lattice parameters for rutile phase VO_2 are $a_R = 5.700$ Å, $b_R = 4.553$ Å, and $c_R = 5.371$ Å, with unit cell volume of 118.16 Å^3[95], using the relationship between monoclinic and rutile-type unit cells of VO_2 $a_M = 2c_R$; $b_M = a_R$; $c_M = a_R - c_R$. Comparing the volume of the monoclinic and rutile phase VO_2, a slight volume expansion(0.044%) during the heating process has been observed [95]. At the same time, a_M and c_M shrink (0.96% for parameter a and 0.24% for parameter c) while b_M expands (0.59%) during the heating process. All the parameters were listed in Table 6.1.

Table 6.1. Lattice Parameters and Unit Cell Volume for VO_2 [95].

	Monoclinic	Rutile	Change
a_M (Å)	5.755	5.700	-0.055 (-0.96%)
b_M (Å)	4.526	4.553	0.027 (0.59%)
c_M (Å)	5.384	5.371	-0.013 (-0.24%)
V (Å^3)	118.11	118.16	0.052 (0.044%)

6.1.2 Existing VO_2 Actuators

Previous work on the VO_2 actuators generally has three approaches to drive the phase transition: global heating, electrothermal, and photothermal. In electrothermally driven VO_2 actuators reported to date, the lateral structures are used where two electrodes are placed above the VO_2 layer, and the current flows through the in-plane direction [96]. When a voltage is applied, the current flowing through the phase change material heats up the total circuit, and thus drives the VO_2 phase transition. Several structures of the VO_2 actuators reported in the literature are illustrated in Fig. 6.2

Merced et al. [97] investigated the strain energy of VO_2 actuators by measuring the curvature change; Cabrera *et al.* [98] integrated the VO_2 actuators in the MEMS devices and determined its static and frequency response performance driven electrothermally; Dong et al.[99] fabricated the VO_2 switches with ultra low operating voltage and long life cycle; Merced et al. [88] combined the electrical and mechanical performance of the VO_2 actuators and established a self-sensing feedback system.

Apart from the lateral structures, the motivation of Vertical structure actuator is to investigate the performance of the vertical stack actuators. Although such configuration is being actively studied for the memory devices, there is currently no literature discussing the VO_2 vertical stack actuators [100], [101]. Here, we perform a study of the vertical stack on the performance of the VO_2 actuator, toward the goal of IC integration for applications

	Cantilever Structure	Cantilever Length	Driving method	Reference
1		800 μm	Heating	[1]
2		40 μm	Heating	[2]
3		550 μm	Electrothermal	[7]
4		300 μm	Electrothermal	[9]
5		40 μm	Heating & Electrothermal	*This work*

Figure 6.2. Comparison of VO_2 actuator structures. Yellow: VO_2, light blue: Si, blue: SiO_2, gray: metal, green: ITO, black: Si_3N_4

benefiting from reduced size, weight, power, and cost. Fig. 6.3 illustrates the cantilever bending based on the induced in-plane strain during phase transition. Compared with the traditional VO_2 lateral electrode actuators, the vertical stacked actuators are more scalable, and the actuator size can reach very small scale without the electrode patterning size limit. Besides, the top electrode is uniformly coated, which avoids the induced strain in the electrode boundary, making the initial strain more uniform. In addition, the surface of VO_2 is protected without the need for a capping layer which would load the actuator. This can prevent VO_2 contacting with the environment directly, making the device more robust in harsh environments. The vertical electrode design provides opportunities to improve the efficiency and flexibility of microscale and nanoscale actuators, with possible applications in smart surfaces and actuation for autonomous microrobots. An understanding of the behavior of the vertical stack actuation in VO_2 is a necessary first step to more sophisticated actuators.

In the following session, the design, analytical calculation, FEA(finite element analysis) and fabrication of a vertical structure VO_2 actuator will be discussed. This device config-

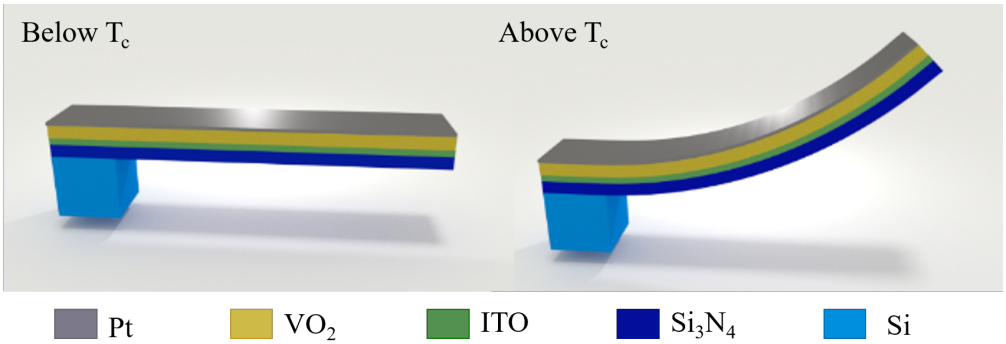

Figure 6.3. Schematic of a vertical stack VO_2-based actuator showing a flat cantilever below the phase transition temperature T_c (left), with thevertical actuation aboveT_c (right).

uration is particularly challenging due to the limited choice of bottom electrodes that can withstand the high-temperature VO_2 deposition conditions and still retain function. The microactuators leveraging this multilayer stack could, therefore, contribute to new design configurations for the monolithic microrobot platforms.

6.2 VO_2 Actuator Design and Fabrication

6.2.1 Layer Stack Design

The multilayer structure under consideration is detailed in Fig. 6.3, composed of four thin films stacked vertically in a cantilever beam. At the bottom, a Si_3N_4 layer is used to push the VO_2 actuation film away from the bending neutral axis. It also serves as an etch stop layer during the release of the device from the Si substrate. Because VO_2 is deposited under high temperature and oxygen atmosphere, typical elemental metals cannot sustain such process due to chemical instability or adhesion problems. Instead, indium tin oxide (ITO) is chosen for the bottom electrode. This is followed by the VO_2 layer, with a final platinum thin film for the top electrode.

There are several concerns when determine the thickness of each layer. First, the Si_3N_4 layer needs to be thick enough for working as a stop layer for XeF_2 etch. 200 nm is a safe thickness to protect front-side layers when etching 10 μm deep Si [102]. Second, the electrical conductivity of ITO is not as good as elemental metals. Therefore, to minimize energy loss in

the ITO layer, thicker ITO is preferred. The resistivity of thin film ITO increases drastically when its thickness is smaller than 50 nm [4], while too thick ITO suppresses deflection. Combining these 2 considerations, the ITO layer thickness is set to be 100 nm.

Besides, the VO_2 layer needs to be offset from the stress neutral axis to provide strain during phase transition, so that Pt is designed thinner than bottom layers (ITO and Si_3N_4) to generate actuation. The thickness of each layer influences the stress neutral axis and total device stiffness comprehensively, which determines the total deflection. Using the stack thickness of 200nm Si_3N_4/100nm ITO/150nm VO_2/50nm Pt, The stress distribution in each layer can be simulated by the finite element analysis via COMSOL Multiphysics^{TM}, as shown in Fig. 6.4.

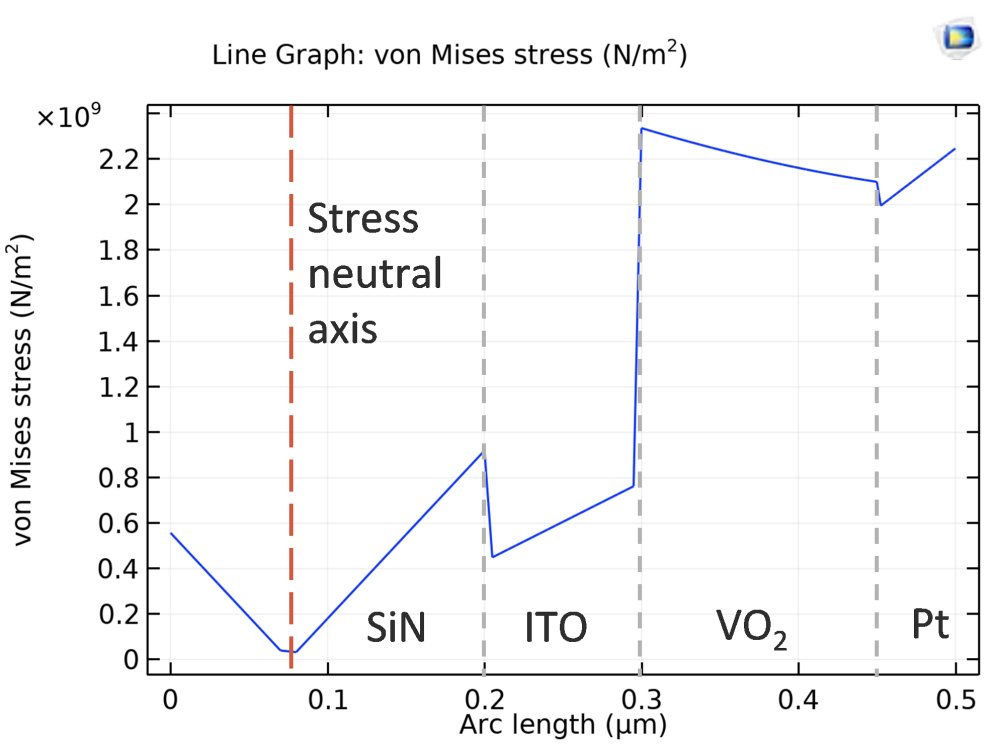

Figure 6.4. Comsol simulation of stress distribution of Si_3N_4/ITO/VO_2/Pt stack in z-axis when it vibrates. x=0 is the bottom of SiN layer.

The x axis in Fig. 6.4 indicates the out of plane direction in the 200nm Si_3N_4/100nm ITO/150nm VO_2/50nm Pt stack, where x=0 is the bottom of the Si_3N_4 layer, and x=500 is the top surface of the Pt layer. In this stack design, when volume shrinkage is added to the VO_2 layer (simulating the VO_2 phase transition induced stress), the lowest stress shows

up in x=0.8, which means the stress neutral axis is placed at the middle of SiN layer. This indicates that in such layer design, the shrinkage of VO_2 layer can successfully transfer to bending deflection in out of place direction.

The bending schematic based on stress is shown in Fig. 6.5. Due to the shrinkage occurred in the VO_2 layer, the nearby Pt and ITO as well as half of the Si_3N_4 also shrank based on the continuity. The bottom half Si_3N_4 layer expanded instead, showing an opposite direction of stress.

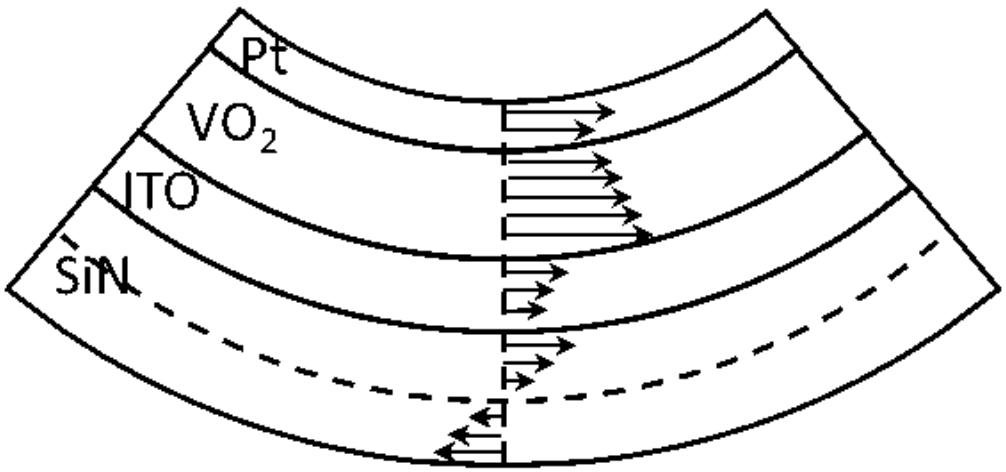

Figure 6.5. Schematic of stress distribution in a bending cantilever

6.2.2 Actuator Structure Design

Once the layer stack is determined, a lateral design for each layer is discussed to realize the actuator functionality. To achieve the vertical current flow through VO_2, in the cantilever part VO_2 is sandwiched by Pt and ITO. The top electrode is connected to the cantilever with a connecting rectangle, as shown in Fig. 6.6. The purpose of the connecting rectangle is to avoid the electrode pad being released, especially when over etch happened. Each device is electrically isolated by the outer XeF_2 etch channel. Inside the device, ITO layer is continuous. When performing electrical measurement, probe 1 is connected with ITO layer and usually is grounded. Probe 2 provides a bias to the top electrode Pt, thus generates a current flow from Pt to VO_2 and then to ITO.

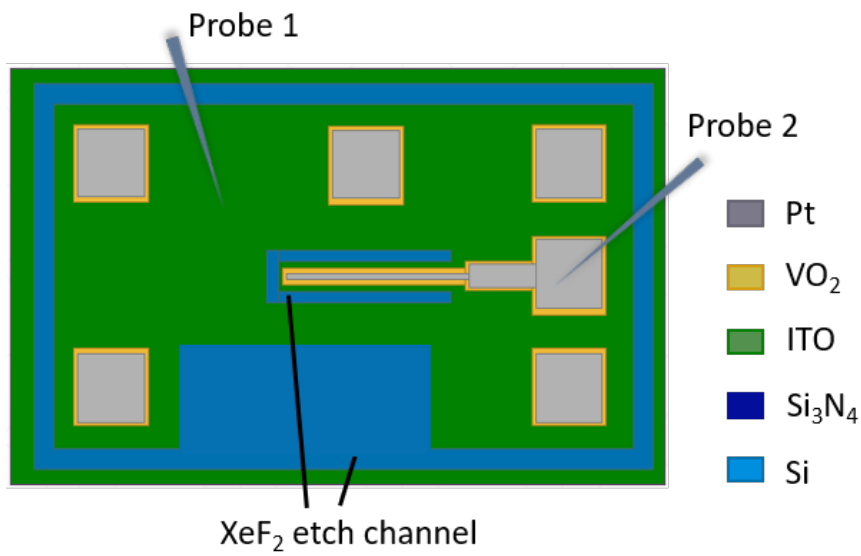

Figure 6.6. VO_2 actuator layout design, front view.

6.2.3 Electrothermal Model

The electrothermal analytical model are first performed to determine the time response of the proposed vertical structure VO_2 actuator. The film thickness configuration of Si_3N_4/ITO/VO_2/Pt of 200 nm/100 nm/150 nm/50 nm is used for the analysis.

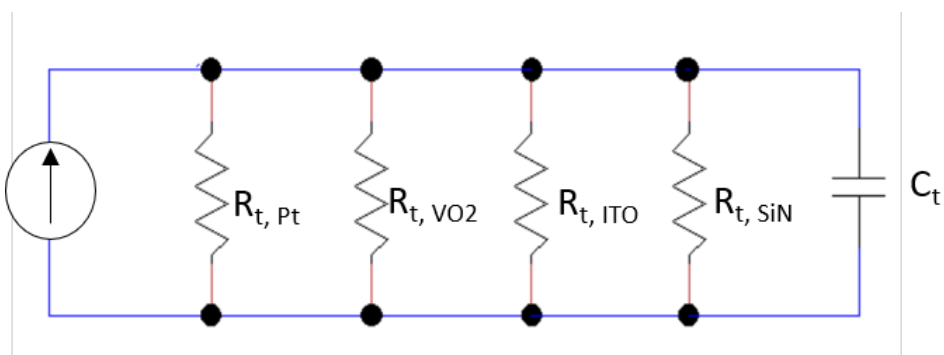

Figure 6.7. Equivalent thermal circuit of the VO_2 actuator cantilever beam.

The equivalent thermal circuit is shown in Fig. 6.7 for a beam of length l. The effective thermal resistance R_t of the parallel layers can be described by the parallel electrical resistance analogy [103], which in this case is

$$\frac{1}{R_t} = \frac{1}{R_{t,Pt}} + \frac{1}{R_{t,VO_2}} + \frac{1}{R_{t,ITO}} + \frac{1}{R_{t,SiN}} \tag{6.1}$$

For the ith layer in the stack, the thermal resistance $R_{t,\mathrm{i}}$ equals to

$$R_{t,\mathrm{i}} = \frac{l}{\kappa_\mathrm{i} A_\mathrm{i}} \tag{6.2}$$

where κ_i is the thermal conductivity and A_i is the cross section area,

$$A_\mathrm{i} = w t_\mathrm{i} \tag{6.3}$$

w is the width and t_i is the thickness for the ith layer. The response time can be calculated using

$$\tau = R_t C_t, \tag{6.4}$$

where the heat capacity C_t equals to

$$C_t = \rho_m \tilde{C}_m V \tag{6.5}$$

$\tilde{C}_m$ is the specific heat capacity, ρ_m is the density, and V is the volume. Because the layers are in parallel and we assume an even heat distribution through the thickness of the cantilever beam, the total thermal capacitance can be calculated by

$$C_{t,\mathrm{i}} = \sum \rho_{m,\mathrm{i}} \tilde{C}_{m,\mathrm{i}} V \tag{6.6}$$

with the following values:

This yields a thermal time constant of

$$\tau = R_t C_t = \frac{1}{\sum \kappa_\mathrm{i} t_\mathrm{i}} \sum \rho_{m,\mathrm{i}} \tilde{C}_{m,\mathrm{i}} t_\mathrm{i} l^2 \tag{6.7}$$

Based on the relationship above, the thermal response time of the proposed vertical structure is plotted in 6.8, assuming the film thickness based on the devices in this work. For the VO_2 cantilevers ranging in length from 1 to 500 μm with,fixed width of 15 μm, τ ranges

Si_3N_4 $\tilde{C}_m = 700$ J/kg · K, $\rho_m = 3100$ kg/m^3, $\kappa = 20$ W/m · K [104]

ITO $\tilde{C}_m = 700$ J/kg · K, $\rho_m = 7140$ kg/m^3, $\kappa = 5.8$ W/m · K [105], [106]

VO_2 $\tilde{C}_m = 690$ J/kg · K, $\rho_m = 4320$ kg/m^3, $\kappa = 6$ W/m · K [107], [108]

Pt $\tilde{C}_m = 133$ J/kg · K, $\rho_m = 21450$ kg/m^3, $\kappa = 7106$ W/m · K [109]

from 0.14 to 35 ms. For our 35-μm-long design, the response time is 0.39 ms. This result is comparable with the previous actuators in the literature. For example, Merced et al. [88] showed a 500 μm VO_2 cantilever with response time of 23 ms; Liuet al. [49] demonstrated a 60 μm VO_2 cantilever which shows a shorter response time of 0.17 ms.

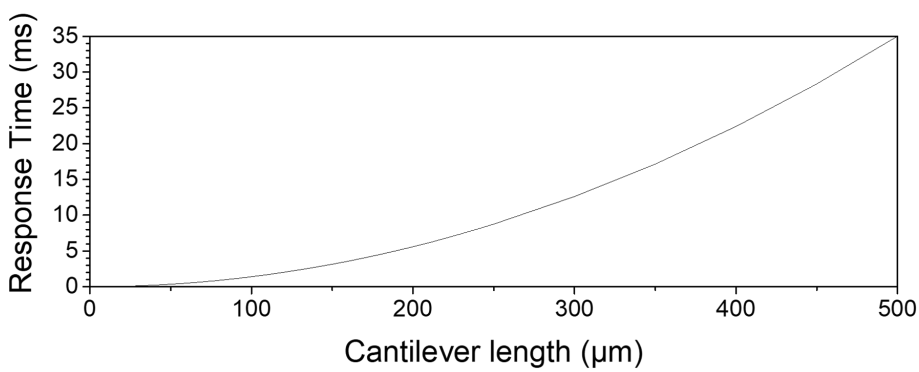

Figure 6.8. Response time of VO_2 cantilever versus cantilever length

The maximum deflection is limited by the ultimate strength as well as induced strain for each layers in the stack. The materials in our actuator have the following ultimate strength: ITO: 2.60 GPa, VO_2: 2 GPa, SiN: 2.76 GPa, Pt: 245 MPa [110], [111]. Since Pt is a ductile metal whose elongation can reach several tens of percent before failure, here the three ceramic layers' limits during tension/compression are mainly considered. The plot of induced stress versus deflection is shown in Fig. 6.9 for the constitutive materials, indicating that VO_2 is the first layer that reaches its ultimate strength during bending. This result is only the case for the specific set of layer thicknesses, and depends intimately on the location

of the neutral axis. In this case, the maximum deflection is 16.4 μm for a 35 μm long cantilever.

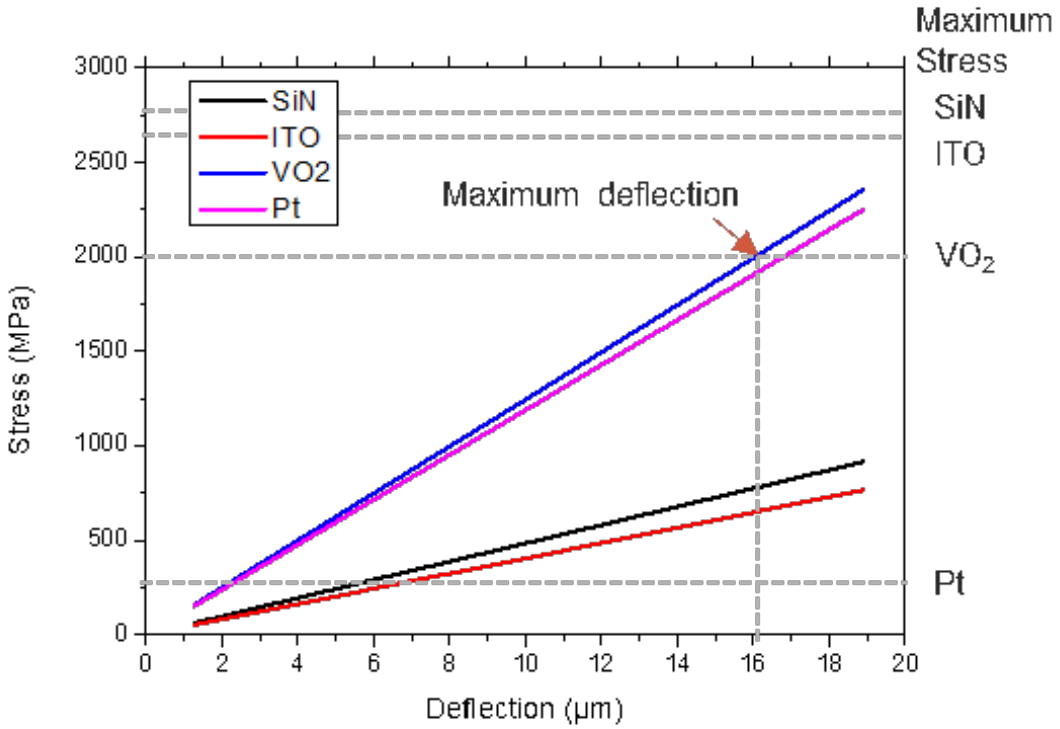

Figure 6.9. Stress induced in each layer by beam bending versus cantilever deflection.

6.2.4 COMSOL Simulation for Surface Temperature

In the geometric configuration of the VO_2 actuator, the multilayer stack exhibits the current-flow-driven Joule heating to induce the MIT which runs both along the length of the beam in the metal electrodes and vertically through the VO_2 layer. As such, any resistive contribution from the electrodes will result in a voltage drop along the beam length and the subsequent spatial dependence of the current. Factoring in the voltage drop along the beam length, the conductive thermal losses to the substrate at the anchor, as well as losses to the surrounding air, the COMSOL finite element analysis is performed to determine the temperature profile induced by the current flow induced by a voltage applied at the device anchor between the Pt and ITO electrodes.

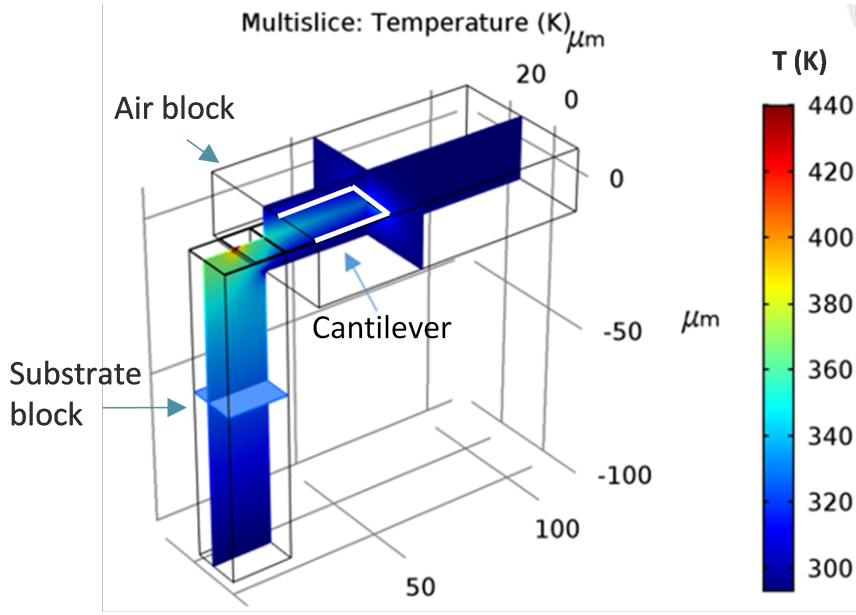

Figure 6.10. Simulated thermal distribution model of VO_2 actuator in COMSOL

Fig. 6.10 shows the heat transfer slice mode of the VO_2 actuator with the substrate and air block. The model mainly consists of three parts:

1. the suspending cantilever: It is a very thin plane in the center of the upper right cube in Fig. 6.10. This is the main object for the temperature analysis;

2. the actuator substrate: It is connected with the cantilever by the anchor. the substrate is the lower left cube shown in Fig. 6.10. The purpose of the substrate is to simulate the heat transfer through cantilever anchor to substrate. The substrate is set to be 100um thick, with bottom temperature set as 300 K.

3. the air block surrounding the cantilever: The upper right cube in Fig. 6.10 is the air block, which is used for cantilever heat loss through nearby air. The temperature of the air block boundary is set at 300 K.

To simulate the performance of electrothermal actuation, current is set to flow from the top electrode Pt layer to the bottom electrode ITO layer, at the center of the actuator anchor. This is simulating the real testing situation, since it is not possible to directly put probes on suspended cantilever, the most usual option is putting the probe at an unreleased

region that is close to the cantilever. Fig. 6.11 plots this temperature distribution along the cantilever axis with $l = 35\mu m$, $w = 15\mu m$, and 0.5 V bias across the actuator. D is the distance away from the anchor on the cantilever beam. For position farther away from the anchor which owns a larger D, a decreasing temperature is found. A 28 K temperature difference is shown between the anchor and the tip due to the voltage drop along the length of the beam, with a maximum of 355 K at the anchor.

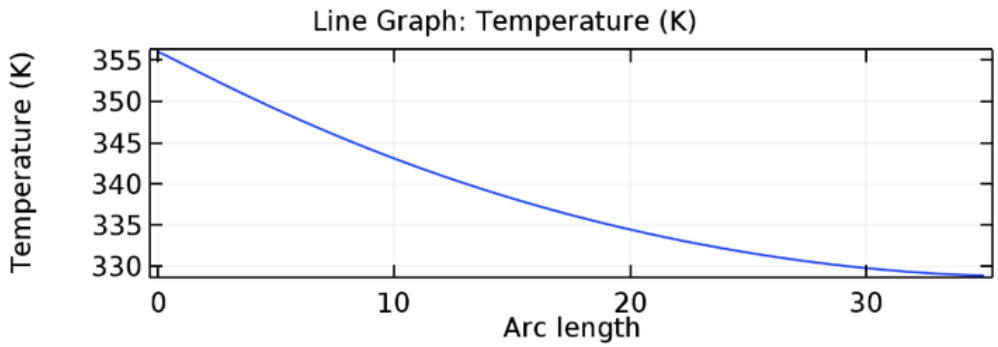

Figure 6.11. COMSOL simulated temperature distribution throughout the VO_2 cantilever.

6.3 Actuator Fabrication and Characterization

6.3.1 VO_2 Actuator Fabrication

Fig. 6.12 describes the micro-fabrication process flow for the actuator. Indium tin oxide (ITO) is selected as the bottom electrode because of the high temperature growth condition of VO_2. ITO is evaporated by e-beam evaporation on the top of commercially purchased 200-nm low-pressure chemical vapor deposition (LPCVD) Si_3N_4 with the Si substrate.

VO_2(150 nm) is deposited by RF magnetron sputtering. The sputtering chamber is heated and stabilized to 650 °C. A V_2O_5 target is used for VO_2 deposition with 100-W RF power. Constant gas flows of 50 sccm Ar and 0.5 sccm 10% O_2 under 5-mTorr chamber pressure are provided during film deposition. The deposition rate is 36 nm/h, with 4h growth for the desired 150 nm VO_2 thin film synthesis. After deposition, VO_2 is patterned lithographically using an inductively coupled plasma (ICP) reactive ion etch (RIE) with Cl_2/Ar chemistry. After removing residual photoresist and wafer cleaning, platinum (50

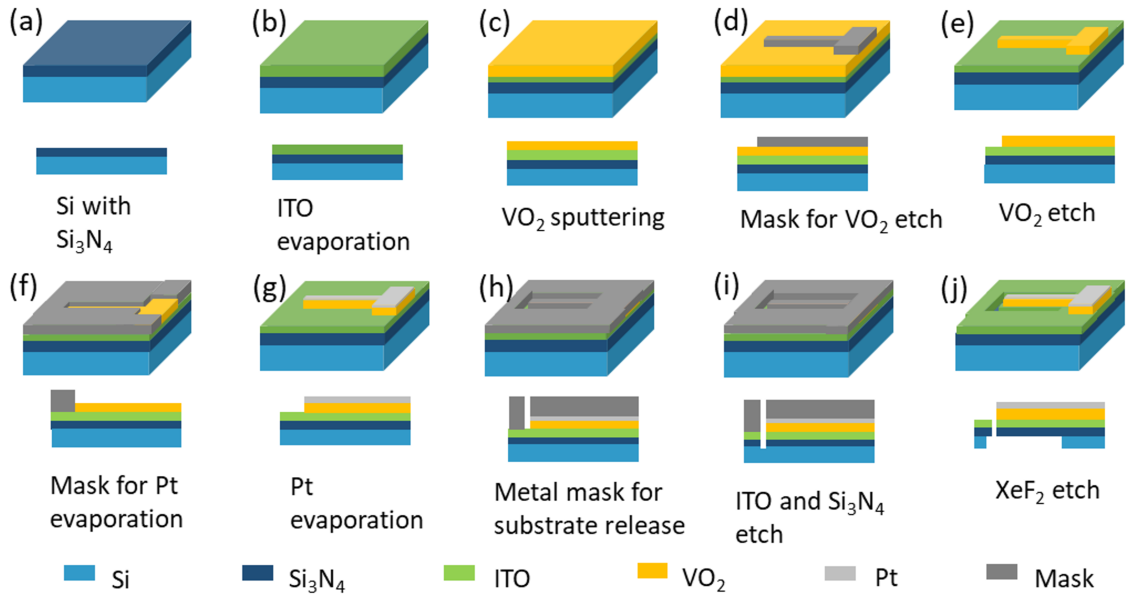

Figure 6.12. Schematics of the fabrication flow for the VO_2-based actuators. (a) physical vapor deposition (PVD) growth of Si_3N_4 on Si. (b) E-beam evaporation of the bottom electrode (ITO). (c) VO_2 sputtering. (d) and (e) RIE of VO_2. (f) and (g) E-beam evaporation of the top electrode (Pt). (h) and (i) RIE of the ITO and Si_3N_4 layer to open channels for XeF_2 etch. (j) Substrate release through XeF_2 etch.

nm) is evaporated and patterned with a lift-off process. To release the substrate underneath the VO_2 cantilever, an etch mask is used to pattern an Al hard mask that covers the devices and only etch-exposed channels. RIE is used to etch windows in ITO and the Si_3N_4 layers to expose the Si substrate below. For the ITO layer, a physical etch using Ar (5 mTorr) is performed under 15 mTorr, 150 W, and 510 V bias. The Si_3N_4 layer is etched by Ar (1 mTorr) and SF_2 (5 mTorr) under 15 mTorr, 100 W, 180 V bias. Finally, XeF_2 Si etch is used to release the cantilever from the Si substrate.

6.3.2 SEM Analysis

Hitachi S-4800 Field Emission SEM is used for image capture. SEM images of released VO_2 actuator is shown in Fig. 6.13. The cantilever has length l=35 μm and width w=15 μm. Due to residual stress in the composite stack, the tip deflection at room temperature under 0V bias is measured at 2.68 μm.

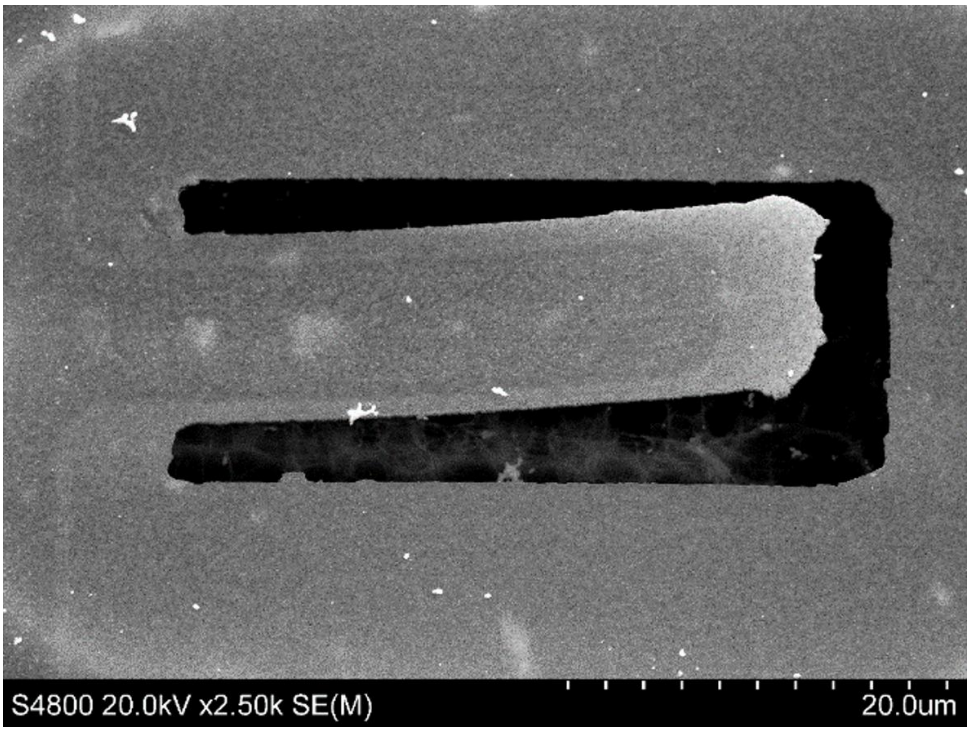

Figure 6.13. SEM image of released $VO2_2$ cantilever under 30º stage tilting.

6.3.3 XRD Analysis of VO_2

X-ray diffraction (XRD) is used to characterize the strain induced during the VO_2 MIT phase transition. Panalytical X'Pert PRO Materials Research Diffractometer (MRD) system was used with Cu anode material and the characteristic wavelength Kα 1 = 1.54056 Å. The XRD pattern of the VO_2 actuators before Pt evaporation is plotted in Fig. 6.14 (a). At 25 °C, VO_2 shows a monoclinic phase with the main peak M(011) at 27.99°; while at 100 °C, VO_2 transformed to its rutile phase, with main peak R(110) shifted leftward to 27.72°. M(011) and R(110) are the same crystal plane but with different Miller indices under different symmetry. Comparing the XRD pattern below and above the phase transition temperature, such shift of VO_2 monoclinic (011) plane peak verifies the structural transition during heating.

A step temperature XRD of the VO_2 actuator is plotted in 6.14 (b), where the peak shift occurs between the phase transition temperature regions. Because the (110) plane is the main observable peak for VO_2, this polycrystalline VO_2 thin film is oriented along the

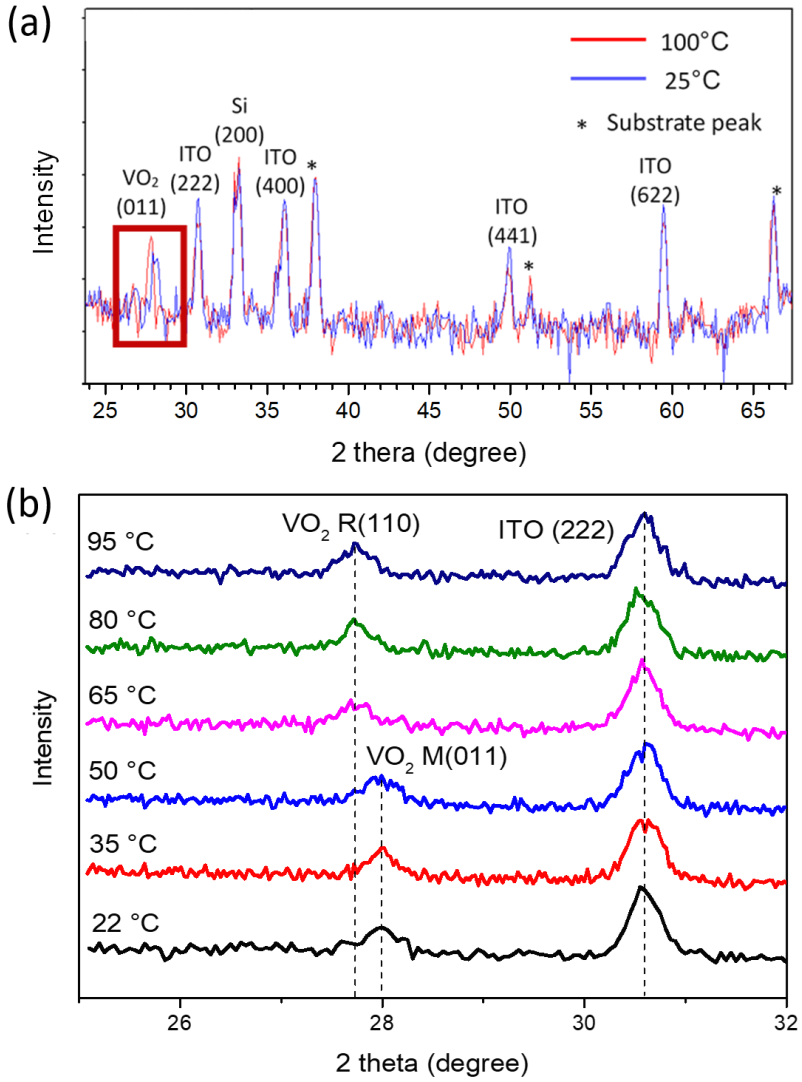

Figure 6.14. (a) XRD patterns of VO_2 at 25 °C (insulating) and 100 °C (metallic). The main VO_2 peak observed is (011) indicating textured film orientation. (b) XRD patterns of VO_2 with different temperatures. When the sample heats above 65 °C, a distinct phase shift of the monoclinic VO_2 (011) peak to rutile VO_2 (110) peak can be observed.

monoclinic (011) plane. Based on the lattice analysis discussed before, the shrinkage of a_M axis of 0.96% dominates the in-plane strain change during the phase transition. Combined with the contribution of the expanding b_M axis, the total in-plane strain is 0.3% [21]. Using this number, the theoretical tip deflection is 3.07 μm calculated by the COMSOL simulation, which is larger than the actual deflection we measured. One assumption is that the defects

and grain boundaries inside the VO_2 thin film released part of the strain induced by the phase transition.

6.4 Actuator Performance Discussion

6.4.1 Thermal Actuation by Heating in a Hot Stage

To characterize the actuator behavior under the MIT phase transition, the tip displacement of the VO_2 actuator is measured by the optical profilometer with interferometer mode equipped with a heating stage. The measured relative tip deflection as a function of cantilever temperature is plotted in black in Fig. 6.15. Below the MIT temperature, the actuator exhibits a minimal deflection of 0.19 μm. In the temperature range 60 °C–70 °C, a large abrupt deflection of 2 μm is observed due to the VO_2 phase transition.

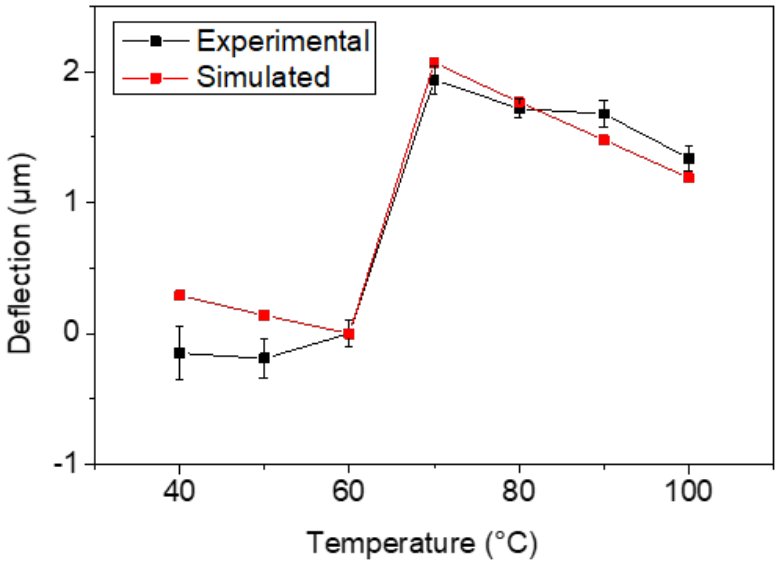

Figure 6.15. Experimentally obtained (black), simulated (red) relative tip displacement of VO_2 actuators. Zero displacement is defined as tip height when temperature is 40 °C. The simulated tip deflection is 3.07 μm, and the experimentally measured deflection is 2 μm.

To certify that the deflection is not owning to thermal expansion, the temperature induced thermal expansion is calculated. The thermal expansion coefficient (TEC) of each materials are listed below:

Materials	TEC
ITO	6.37×10^{-6} K^{-1}
VO_2, Monoclinic	5.7×10^{-6} K^{-1}
VO_2, rutile	13.35×10^{-6} K^{-1}
Si_3N_4	2.3×10^{-6} K^{-1}

In its low temperature (monoclinic) phase, TEC of VO_2 is similar to those of ITO and Si_3N_4 [95], [112], resulting in minimal displacement with changing temperature. However, the TEC of the rutile phase VO_2 is much larger than that of ITO and Si_3N_4, so that with increasing temperature above the MIT, the thermally expanded VO_2 cancels out part of the negative strain caused by the phase transition. Therefore, at high temperature, the tip displacement slightly reduces at a rate of 0.03 μm/K due to the TEC difference between the constituent layers. This aligns well with the COMSOL simulation factoring in the TEC contribution to strain in the actuator in the high-temperature regime. The simulated tip deflection including both the TEC effects and strain induced during the phase transition is plotted in red in Fig. 6.15. A simplified isotropic thermal-expansion induced strain is used to simulate the phase transition strain.

6.4.2 Electrothermal Actuation

Toward the goals of micro-actuator system integration, the VO_2 phase transition can also be electrothermally controlled by flowing a current to heat the cantilever [88], [113]. The upper right schematic in Fig. 6.16 indicated the electrical measurement of the vertical VO_2 actuator. The top Pt electrode is connected to a positive bias, and the bottom electrode ITO is grounded. Electrothermal induction of the phase transition was characterized for the

curve of the VO_2 cantilever. Abrupt changes in resistance corresponding to the MIT phase transition are observed at 1.95 V and 1.05 V in the upward and downward voltage ramps, respectively, shown in Fig. 6.16.

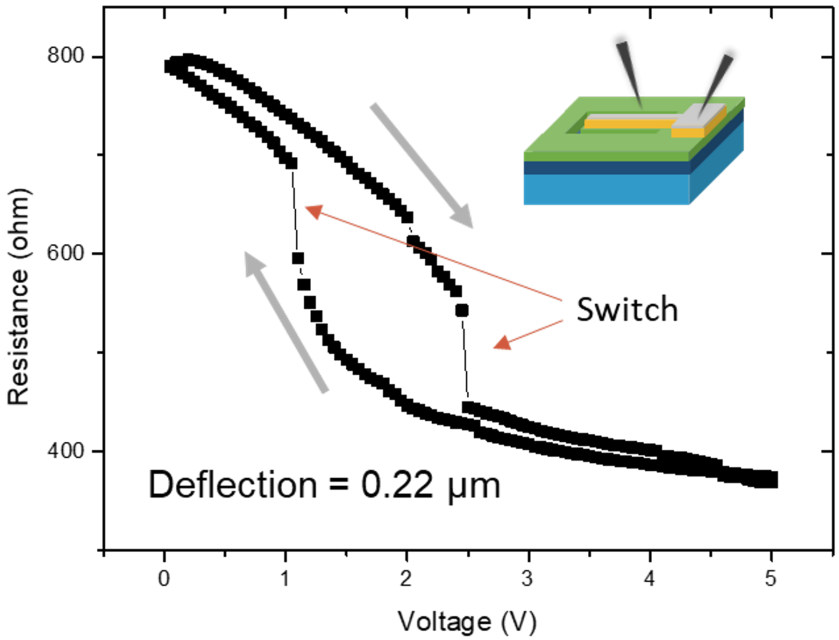

Figure 6.16. R-V characteristics of vertical VO_2 actuator. The abrupt change of resistance indicates that phase transition occurred around 2.2 V. A schematic of electrothermal driven method is shown in the lower left corner. The resulted deflection is 0.22 μm, measured by optical profilometer.

1000 cycles have been run to test the actuator's stability, as shown in Fig. 6.17. The phase transition showed no degradation after 1000 cycles, and 0.15V fluctuation of the MIT voltage is observed. The fluctuation may come from poor heat dissipation since the probe station is under vacuum, and the heat generated from previous sweep affects the following measurements.

Typically, the electrical conductivity of VO_2 films abruptly decreases during MIT by 2-4 orders of magnitude depending on the substrate and growth parameters [114], [115]. However, the measured resistance in this actuator device only changes 1.36x, which is small compared with what is noted in lateral actuators. To solve this problem, a distributed resistive network is defined in Fig. 6.18 to model the electrical behavior based on this

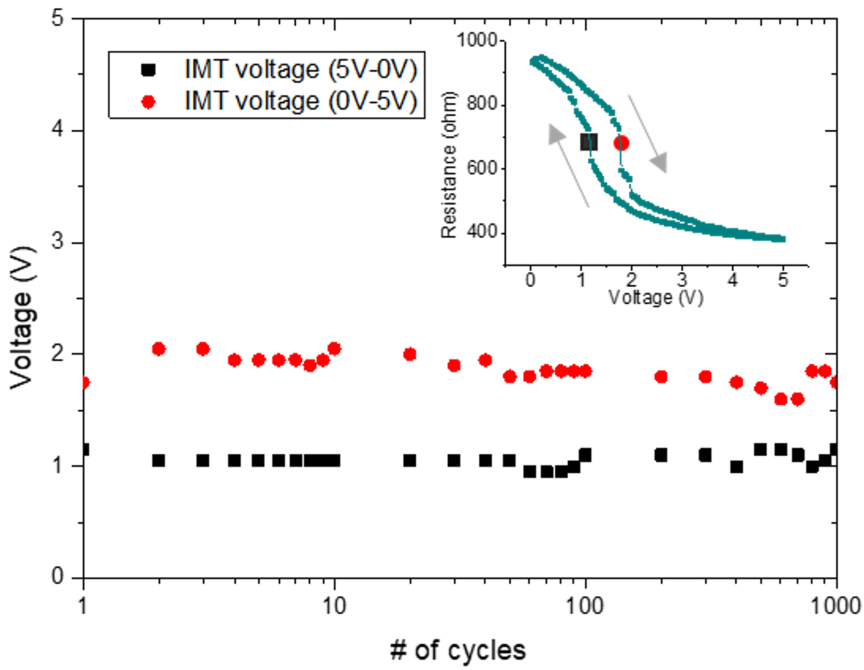

Figure 6.17. MIT voltage during positive/negative switching of R-V characteristics of vertical VO_2 actuator versus cycling number. Figure inserted in the top right indicated the MIT voltage during 0V-5V switch and 5V-0V switch.

device geometry. The incremental resistance at position x along length Δx for each of the constituent layers is given by

$$R_{Pt} = \rho_{Pt}\frac{\Delta x}{wt_{Pt}} \tag{6.8}$$

$$R_{ITO} = \rho_{ITO}\frac{\Delta x}{wt_{ITO}} \tag{6.9}$$

$$R_{VO_2} = \rho_{VO_2}\frac{\Delta x}{wt_{VO_2}} \tag{6.10}$$

ρ_{ITO} and ρ_{VO_2} are the electrical resistivity of ITO and VO_2. t_{ITO} and t_{VO_2} are the film thicknesses of ITO and VO_2. w is the beam width. Here, we assume current flow parallel to the beam length for the ITO and Pt layers, and vertical current flow in the VO_2. To simplify the model, we assume $R_{Pt} \ll R_{ITO}$ due to the 100x difference in resistivity between the two materials. Based on the distributed resistance model by Zeghbroeck [116], we find

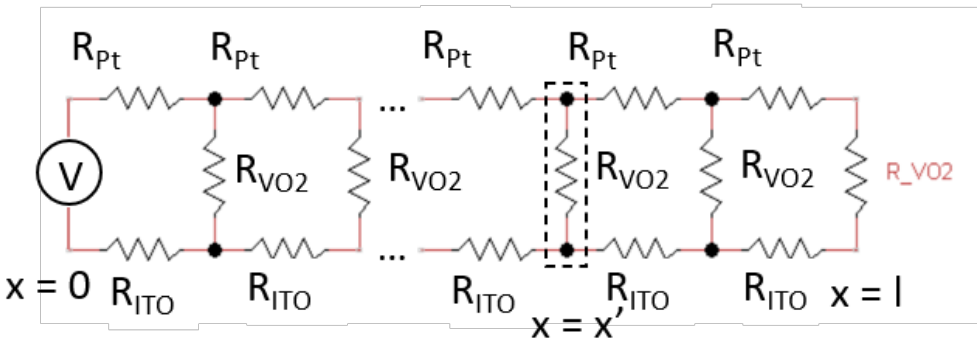

Figure 6.18. Distributed electrical resistance model of the VO_2 cantilever, including current paths in the Pt, VO_2 and ITO layers. For the loop at $x = x$, current runs from cantilever ground to x, then across VO_2 layer and runs back to cantilever ground through ITO layer.

$$\begin{aligned} \Delta V &= V(x+\Delta x) - V(x) = I(x)R_{ITO} \\ &= \frac{\rho_{ITO}}{wt_{ITO}} I(x)\Delta(x) \end{aligned} \tag{6.11}$$

$$\begin{aligned} \Delta I &= I(x+\Delta x) - I(x) = \frac{V(x)}{R_{VO_2}} \\ &= \frac{w}{\rho_{VO_2} t_{VO_2}} V(x)\Delta(x) \end{aligned} \tag{6.12}$$

Here V is the voltage across R_{VO_2} and I is the current flowing through R_{ITO} at position x. When Δx goes to infinitesimal, the expression of the current and voltage turns to

$$\frac{dv}{dx} = \frac{\rho_{ITO}}{wt_{ITO}} I(x) \tag{6.13}$$

$$\frac{dI}{dx} = \frac{w}{\rho_{VO_2} t_{VO_2}} V(x) \tag{6.14}$$

Combining these two equations we have

$$\frac{d^2 I(x)}{dx^2} = I(x) \frac{1}{\rho_{VO_2} t_{VO_2}} \frac{\rho_{ITO}}{t_{ITO}} = \frac{I(x)}{\lambda^2} \tag{6.15}$$

where

$$\lambda = \sqrt{\rho_{VO_2} t_{VO_2} \frac{t_{ITO}}{\rho_{ITO}}} \tag{6.16}$$

The expression for $I(x)$ and $V(x)$ is then

$$I(x) = I_0 \frac{sinh\frac{L-x}{\lambda}}{sinh\frac{L}{\lambda}} \tag{6.17}$$

$$V(x) = I_0 \lambda \frac{\rho_{ITO}}{w t_{ITO}} \frac{cosh\frac{L-x}{\lambda}}{sinh\frac{L}{\lambda}} \tag{6.18}$$

The total resistance of current flowing through VO_2 layers is

$$R_V = \frac{V(0)}{I(0)} = \frac{1}{w}\sqrt{\rho_{VO_2} t_{VO_2} \frac{\rho_{ITO}}{t_{ITO}}} cosh\frac{L}{\lambda} \tag{6.19}$$

The width and distance between 2 electrodes is w_{e} and d, and total resistance is

$$R = \frac{1}{w}\sqrt{\rho_{VO_2} t_{VO_2} \frac{\rho_{ITO}}{t_{ITO}}} cosh\frac{L}{\lambda} + \rho_{ITO}\frac{d}{w_{\mathrm{e}} t_{ITO}} \tag{6.20}$$

Plugging in the following numbers:

$$\rho_{ITO} = 7.5 \times 10^{-6}\ \Omega \cdot m$$
$$\rho_{VO_2} = 1 \times 10^{-4}\ \Omega \cdot m, \text{ conducting state}$$
$$\rho_{VO_2} = 0.1\ \Omega \cdot m, \text{ insulating state}$$
$$t_{ITO} = 100\ nm,\ t_{VO_2} = 150\ nm$$
$$L = 35\ \mu m,\ d = 235\ \mu m,\ w = 15\ \mu m,\ w_{\mathrm{e}} = 70\ \mu m$$

the overall resistance R corresponding to VO_2 insulating state and metallic state are 233.67 Ω and 169 Ω, which only shows a 1.34x resistance difference.

A 3D model of the multilayer Pt-VO_2-ITO actuator was then established in COMSOL as shown in Fig. 6.19, informing current density distributions across the device in both monoclinic and rutile VO_2. A 1000x conductivity difference was set to insulating (10 S/m) and metallic phase (10^4 S/m) of VO_2. Factoring in the non-uniform current flow along the cantilever length and distributed resistive contribution of the ITO, a resistance change of 1.4x is extracted across the measured VO_2 film which is consistent with the experimental

observation and theoretical results. Moreover, with insulating phase VO_2, there is very little current flows through the VO_2 cantilever, resulting very small effects to the VO_2 phase transition. Cantilevers farther away from the anchor has smaller effects, as shown in the zoomed in pictures shown in Fig. 6.19.

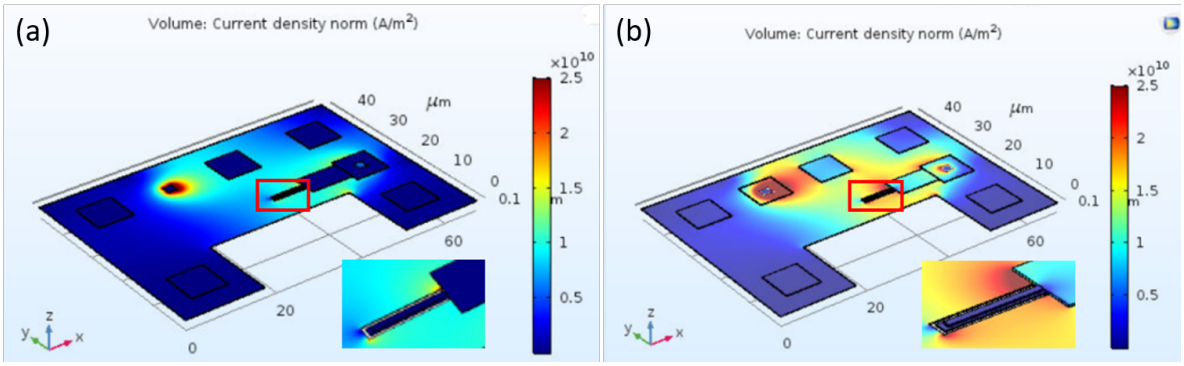

Figure 6.19. COMSOL Simulation of Current density distribution in vertical VO_2 actuator with (a) insulating VO_2 and (b) metallic VO_2. A positive bias is dropped at the cantilever connected electrode. The second left electrode pad (the pad with highest current density, there is no VO_2 and Pt layer on top of this pad.) is grounded.

The phase transition deflection is optically measured by optical profilometer during electrothermal actuation. Under zero bias, the cantilever tip height is 3.12 μm; when voltage larger than the critical phase transition voltage is applied, 0.22 μm tip displacement is observed. This value is 10x smaller than in the case of the global heating phase transition induced tip displacement due to the non-uniform heating of the cantilever discussed above and is exacerbated by the drop in VO_2 resistance above the phase transition. This result also matched up with the conclusion we got in the current density distribution simulation. This can be improved in future with the addition of a thin dielectric layer near the cantilever base, which would force current flow along a larger fraction of the length of the beam.

6.4.3 Anchor Undercut Effects Due to XeF_2 Release

The XeF_2 release step generates a 10 μm undercut on the perimeter of the release window, including at the actuator's anchor. The undercut serves to reduce the stiffness of the cantilever, altering the actuator deflection relative to the case of a fixed (ideally

anchored) design. To address this difference, COMSOL simulation was performed with the revised anchor boundary conditions. In the ideal case (Fig. 6.20(a)), the anchor is simulated with a fixed boundary condition directly at the base of the cantilever. In the case of the undercut (Fig. 6.20(b), a 10um wide membrane composed of the same stack as the actuator extends beyond the cantilever, with fixed boundary conditions at its perimeter.

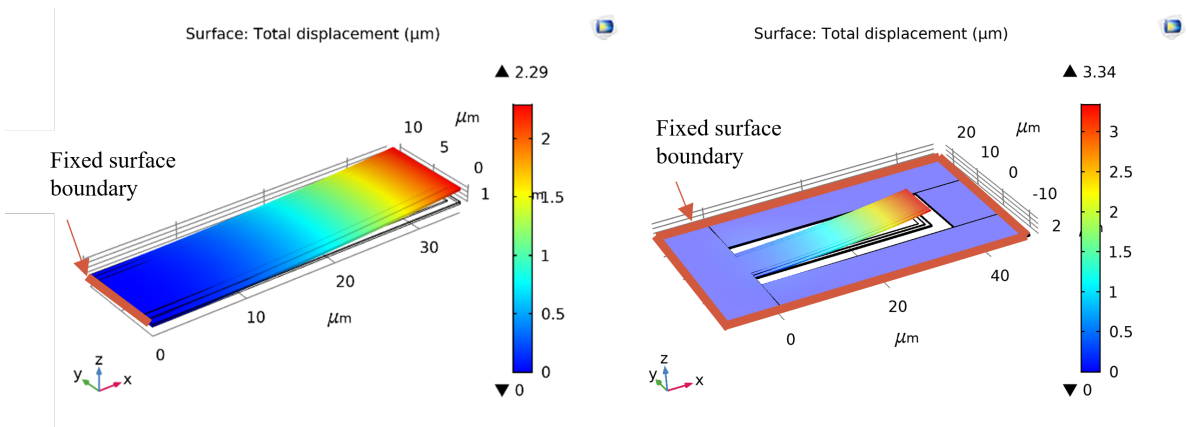

Figure 6.20. Comsol simulation of cantilever deflection (left) in ideal case and (right) considering anchor undercut. Red line indicates the fixed surface boundary adopted during simulation, which indicates the boundary of Si substrate release.

Based on simulation results, the anchor undercut does slightly increase the tip deflection. Comparing simulation and measurement, experimentally obtained tip deflection is smaller than theoretical value. One reason for this could be due to the polycrystalline nature of the VO_2 which might affect the exact stress relaxation profile.

7. SUMMARY AND FUTURE AVENUES

7.1 Summary of Vertical VO_2 Actuator

A vertically-stacked multilayer actuator is designed and fabricated using vanadium dioxide. During heating, the VO_2 film undergoes an insulator-to-metal phase transition resulting in an induced strain of 0.3% in the phase change material. The thermal actuation of the cantilever is measured with tip displacement of 2 μm. Due to the new electrode topology reported in this work, electrical and analytical models are developed to characterize the performance of this actuation platform. 3D models were generated in the COMSOL finite element analysis tool to analyze the current behavior for Joule heating and temperature profile in cantilever geometries. Electrothermal actuation of the VO_2 cantilever generates measured tip displacement of 0.22 μm for a 35 μm long beam, which is about 10x smaller than under global heating but can be ameliorated with the addition of a thin dielectric over a fraction of the beam to route current further toward the tip. The demonstration and characterization of this actuation geometry using phase change materials contributes toward monolithic integration of microactuators with active phase change-based devices.

7.2 Summary of Perovskite Nickelate Actuator

The unique phase transition phenomenon introduced by electron doping makes NNO a strong candidate for MEMS applications. Compared with other perovskite nickelates, NNO exhibits a metallic phase at room temperature, and also shows the tremendous property change after the electron doping induced phase transition at elevated temperature. The lattice parameter of NNO changed up to 2.37% in linear direction and more than 6% volumetric strain generated, with resistivity increased 8 orders of magnitude after electron doping. The nonvolatile actuation and standard surface micromachining at wafer scale makes it compatible to integrated fabrication.

The simultaneously large Young's modulus and strain present upon hydrogen-induced phase transition in $NdNiO_3$ make it an excellent candidate for further study as a competitive actuator material. Theoretical potential for even larger strains and for electrically-driven actuation aside, work densities of up to 6.7 J/cm^3, modeled by finite element analysis calibrated

to experimental data, are higher than piezoelectric actuators and are highly competitive with shape memory alloys and dielectric elastomer fibres. $NdNiO_3$ may complement other high work-density actuation materials and widens the range of possible stiffness and strain that can be used to achieve efficient actuation in the emerging field of micro- and nano-robotics.

7.3 Avenues of Future Research

There is still room for further optimization of NNO actuator structures. For example, hydrogen out diffusion from the top side during actuation still brings performance degradation. This problem may be alleviated by adding H_2 stop layer on top of Pd electrode. However, adding an extra layer will significantly reduce actuator performance and result in a lower utilization of total energy. An ideal extra H_2 stop layer should have specific structures that can minimize energy loss and performance reduction.

Becides, using lithium as the doping chemical may be another acceptable option, since lithium won't escape from the device based on its larger ion size and much lower vapor pressure. Lithium doping also provides a larger perovskite nicklates lattice change, but the same time a slower diffusion rate. Instead of protons that are doped through H_2 atmosphere and Pd catalyst, lithium is usually doped through electrochemical method in electrolyte solution. To adapt the lithium doping method, layout design has to be adjusted for NNO layer exposure, and the release step has to be done after doping process to avoid damaged due to surface tension when changing from the liquid to gaseous state during lithium doping.

NNO grown on substrates with matched lattice parameters will have much better performance due to the better crystallization and less defects. However, it's not easy to find a single crystal or epitaxial conducting thin film which has a matching lattice parameter to that of NNO, and at the same time be inert during the high temperature annealing process; here our choice is ITO. While ITO does not lattice match, it performs well in other aspects. Presently, we sacrifice the optimized thin film orientation to begin this research, but in the future a perfect bottom electrode is needed to replace ITO.

Besides single cantilever device, other designs of NNO based MEMS actuator can also be developed in the future. For example, NNO membrane has a better potential on damping efficiency, higher resonant frequency and higher quality factor compared with a

cantilever actuator. Fig. 7.1 shows an advanced NNO actuator composed of a center plane and 4 meander springs. The meander springs accumulate work and deflection from each cantilever, generating an amplified actuation performance compared with single cantilevers. besides, when the four meanders are controlled with different circuit, lateral deflection could be achieved by activating specific meanders.

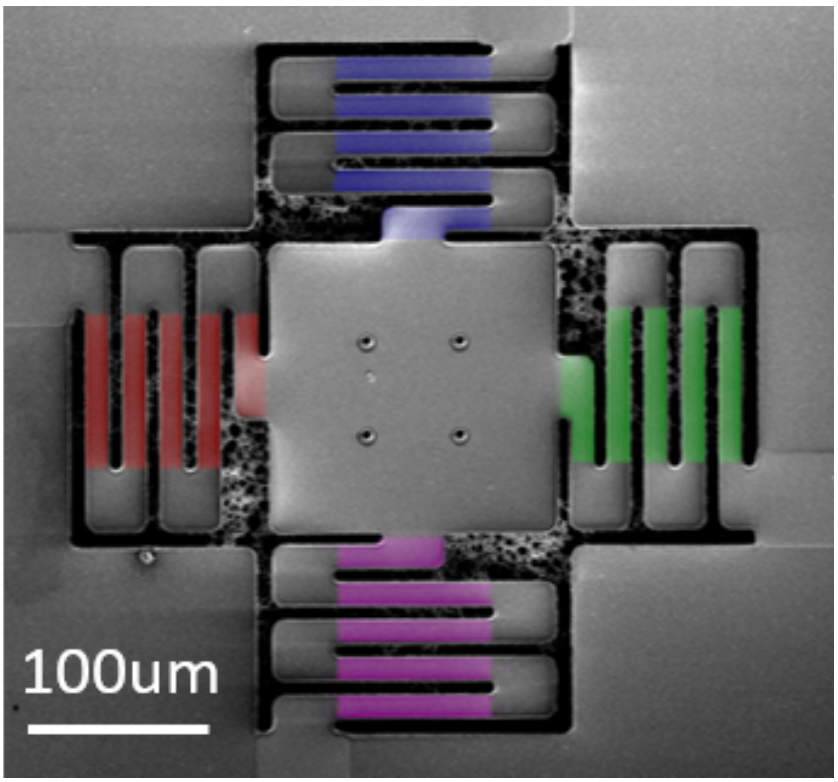

Figure 7.1. SEM image of fabricated Xcross NNO actuators with meandering springs

REFERENCES

[1] M. A. Green, A. Ho-Baillie, and H. J. Snaith, "The emergence of perovskite solar cells," *Nature photonics*, vol. 8, no. 7, pp. 506–514, 2014.

[2] M. L. Medarde, "Structural, magnetic and electronic properties of perovskites (r= rare earth)," *Journal of Physics: Condensed Matter*, vol. 9, no. 8, p. 1679, 1997.

[3] T. H. Nilsen, "Devonian (old red sandstone) sedimentation and tectonics of norway: Comparisons in the north atlantic borders," 1973.

[4] J. García-Muñoz, J. Rodriguez-Carvajal, P. Lacorre, and J. Torrance, "Neutron-diffraction study of r nio 3 (r= la, pr, nd, sm): Electronically induced structural changes across the metal-insulator transition," *Physical review B*, vol. 46, no. 8, p. 4414, 1992.

[5] J. Alonso, M. Martínez-Lope, M. Casais, J. García-Muñoz, and M. Fernández-Díaz, "Room-temperature monoclinic distortion due to charge disproportionation in r nio 3 perovskites with small rare-earth cations (r= ho, y, er, tm, yb, and lu): A neutron diffraction study," *Physical Review B*, vol. 61, no. 3, p. 1756, 2000.

[6] A. Wold, B. Post, and E. Banks, "Rare earth nickel oxides," *Journal of the American Chemical Society*, vol. 79, no. 18, pp. 4911–4913, 1957.

[7] S. Geller, "Crystal structure of gadolinium orthoferrite, gdfeo3," *The Journal of Chemical Physics*, vol. 24, no. 6, pp. 1236–1239, 1956.

[8] I. M. Reaney, E. L. Colla, and N. Setter, "Dielectric and structural characteristics of ba-and sr-based complex perovskites as a function of tolerance factor," *Japanese Journal of Applied Physics*, vol. 33, no. 7R, p. 3984, 1994.

[9] P. Lacorre, J. Torrance, J. Pannetier, A. Nazzal, P. Wang, and T. Huang, "Synthesis, crystal structure, and properties of metallic prnio3: Comparison with metallic ndnio3 and semiconducting smnio3," *J. Solid State Chem*, vol. 91, no. 2, pp. 225–237, 1991.

[10] J. Rodríguez-Carvajal, S. Rosenkranz, M. Medarde, P. Lacorre, M. Fernandez-Díaz, F. Fauth, and V. Trounov, "Neutron-diffraction study of the magnetic and orbital ordering in 154 smnio3 and 153 eunio3," *Physical Review B*, vol. 57, no. 1, p. 456, 1998.

[11] M. Cyrot and C. Lyon-Caen, "Orbital superlattice in the degenerate hubbard model," *Journal de Physique*, vol. 36, no. 3, pp. 253–266, 1975.

[12] R. Englman and R. Englman, *The Jahn-Teller effect in molecules and crystals*. Wiley-Interscience New York, 1972.

[13] G. Demazeau, A. Marbeuf, M. Pouchard, and P. Hagenmuller, "Sur une série de composés oxygènes du nickel trivalent derivés de la perovskite," *Journal of Solid State Chemistry*, vol. 3, no. 4, pp. 582–589, 1971.

[14] J. García-Muñoz, J. Rodríguez-Carvajal, and P. Lacorre, "Sudden appearance of an unusual spin density wave at the metal-insulator transition in the perovskites rnio3 (r= pr, nd)," *EPL (Europhysics Letters)*, vol. 20, no. 3, p. 241, 1992.

[15] J. García-Muñoz, J. Rodríguez-Carvajal, and P. Lacorre, "Neutron-diffraction study of the magnetic ordering in the insulating regime of the perovskites r nio 3 (r= pr and nd)," *Physical Review B*, vol. 50, no. 2, p. 978, 1994.

[16] J. Torrance, P. Lacorre, A. Nazzal, E. Ansaldo, and C. Niedermayer, "Systematic study of insulator-metal transitions in perovskites r nio 3 (r= pr, nd, sm, eu) due to closing of charge-transfer gap," *Physical Review B*, vol. 45, no. 14, p. 8209, 1992.

[17] R. G. Burns and R. G. Burns, *Mineralogical applications of crystal field theory*. Cambridge university press, 1993, vol. 5.

[18] J. Shi, Y. Zhou, and S. Ramanathan, "Colossal resistance switching and band gap modulation in a perovskite nickelate by electron doping," *Nature communications*, vol. 5, no. 1, pp. 1–9, 2014.

[19] J. Van Vleck, "Theory of the variations in paramagnetic anisotropy among different salts of the iron group," *Physical Review*, vol. 41, no. 2, p. 208, 1932.

[20] I. Mazin, D. Khomskii, R. Lengsdorf, J. Alonso, W. Marshall, R. Ibberson, A. Podlesnyak, M. Martínez-Lope, and M. Abd-Elmeguid, "Charge ordering as alternative to jahn-teller distortion," *Physical review letters*, vol. 98, no. 17, p. 176 406, 2007.

[21] X. Granados, J. Fontcuberta, X. Obradors, and J. Torrance, "Metastable metallic state and hysteresis below the metal-insulator transition in prnio 3," *Physical Review B*, vol. 46, no. 24, p. 15 683, 1992.

[22] X. Granados, J. Fontcuberta, X. Obradors, L. Manosa, and J. Torrance, "Metallic state and the metal-insulator transition of ndnio 3," *Physical Review B*, vol. 48, no. 16, p. 11 666, 1993.

[23] M. A. Mroginski, N. E. Massa, H. Salva, J. A. Alonso, and M. J. Martínez-Lope, "Metal-insulator phase transitions of smnio 3 and prnio 3: Electrons in a polaronic medium," *Physical Review B*, vol. 60, no. 8, p. 5304, 1999.

[24] G. Catalan, "Progress in perovskite nickelate research," *Phase Transitions*, vol. 81, no. 7-8, pp. 729–749, 2008.

[25] J.-S. Zhou, J. Goodenough, B. Dabrowski, P. Klamut, and Z. Bukowski, "Enhanced susceptibility in l nio 3 perovskites (l= l a, p r, n d, n d 0.5 sm 0.5)," *Physical review letters*, vol. 84, no. 3, p. 526, 2000.

[26] M. T. Escote, V. Barbeta, R. Jardim, and J. Campo, "Metal–insulator transition in nd1- xeuxnio3 compounds," *Journal of Physics: Condensed Matter*, vol. 18, no. 26, p. 6117, 2006.

[27] G. Frand, O. Bohnke, P. Lacorre, J. Fourquet, A. Carré, B. Eid, J. Théobald, and A. Gire, "Tuning of metal/insulator transition around room temperature of perovskites sm1-xndxnio3," *Journal of Solid State Chemistry*, vol. 120, no. 1, pp. 157–163, 1995.

[28] J. A. Alonso, M. J. Martinez-Lope, M. T. Casais, M. A. Aranda, and M. T. Fernandez-Diaz, "Metal- insulator transitions, structural and microstructural evolution of rnio3 (r= sm, eu, gd, dy, ho, y) perovskites: Evidence for room-temperature charge disproportionation in monoclinic honio3 and ynio3," *Journal of the American Chemical Society*, vol. 121, no. 20, pp. 4754–4762, 1999.

[29] G. H. Aydogdu, S. D. Ha, B. Viswanath, and S. Ramanathan, "Epitaxy, strain, and composition effects on metal-insulator transition characteristics of smnio3 thin films," *Journal of Applied Physics*, vol. 109, no. 12, p. 124 110, 2011.

[30] A. Tiwari, C. Jin, and J. Narayan, "Strain-induced tuning of metal–insulator transition in ndnio 3," *Applied physics letters*, vol. 80, no. 21, pp. 4039–4041, 2002.

[31] E. Mikheev, A. J. Hauser, B. Himmetoglu, N. E. Moreno, A. Janotti, C. G. Van de Walle, and S. Stemmer, "Tuning bad metal and non-fermi liquid behavior in a mott material: Rare-earth nickelate thin films," *Science advances*, vol. 1, no. 10, e1500797, 2015.

[32] P. Laffez, O. Lebedev, P. Ruello, R. Desfeux, G. Banerjee, and F. Capon, "Evidence of strain induced structural change in hetero-epitaxial ndnio3 thin films with metal-insulator transition," *The European Physical Journal Applied Physics*, vol. 25, no. 1, pp. 25–31, 2004.

[33] G. Janssen and W. Nieuwpoort, "Band gap in nio: A cluster study," *Physical Review B*, vol. 38, no. 5, p. 3449, 1988.

[34] Y. Zhou, X. Guan, H. Zhou, K. Ramadoss, S. Adam, H. Liu, S. Lee, J. Shi, M. Tsuchiya, D. D. Fong, *et al.*, "Strongly correlated perovskite fuel cells," *Nature*, vol. 534, no. 7606, pp. 231–234, 2016.

[35] R. Ramadoss, R. Dean, and X. Xoing, "System on chip test architectures," *System on Chip Test Architectures: Nanometer Design for Testability; Elsevier: Burlington, MA, USA*, 2008.

[36] M. K. Mishra, V. Dubey, P. Mishra, and I. Khan, "Mems technology: A review," *Journal of Engineering Research and Reports*, pp. 1–24, 2019.

[37] R. Ghodssi and P. Lin, *MEMS materials and processes handbook*. Springer Science & Business Media, 2011, vol. 1.

[38] K. E. Petersen, "Silicon as a mechanical material," *Proceedings of the IEEE*, vol. 70, no. 5, pp. 420–457, 1982.

[39] R. Noyce and M. Hoff, "A history of microprocessor development at intel," *IEEE Micro*, no. 1, pp. 8–21, 1981.

[40] K. A. Shaw, Z. L. Zhang, and N. C. MacDonald, "Scream i: A single mask, single-crystal silicon, reactive ion etching process for microelectromechanical structures," *Sensors and Actuators A: Physical*, vol. 40, no. 1, pp. 63–70, 1994.

[41] O. Solgaard, F. Sandejas, and D. Bloom, "Deformable grating optical modulator," *Optics letters*, vol. 17, no. 9, pp. 688–690, 1992.

[42] K. W. Markus, D. A. Koester, A. Cowen, R. Mahadevan, V. R. Dhuler, D. Roberson, and L. Smith, "Mems infrastructure: The multiuser mems processes (mumps)," in *Micromachining and Microfabrication Process Technology*, International Society for Optics and Photonics, vol. 2639, 1995, pp. 54–63.

[43] V. SUMMiT, "Five level surface micromachining technology design manual," *See URL www. mems. sandia. gov/samples/doc/SUMMiT_V_Dmanual. pdf*, 2012.

[44] W. Wang and S. A. Soper, *Bio-MEMS: technologies and applications*. CRC press, 2006.

[45] J. Minase, T.-F. Lu, B. Cazzolato, and S. Grainger, "A review, supported by experimental results, of voltage, charge and capacitor insertion method for driving piezoelectric actuators," *Precision Engineering*, vol. 34, no. 4, pp. 692–700, 2010.

[46] P. Muralt, "Ferroelectric thin films for micro-sensors and actuators: A review," *Journal of micromechanics and microengineering*, vol. 10, no. 2, p. 136, 2000.

[47] M. D. Manrique-Juarez, S. Rat, L. Salmon, G. Molnár, C. M. Quintero, L. Nicu, H. J. Shepherd, and A. Bousseksou, "Switchable molecule-based materials for micro- and nanoscale actuating applications: Achievements and prospects," *Coordination Chemistry Reviews*, vol. 308, pp. 395–408, 2016.

[48] J. Cao, W. Fan, Q. Zhou, E. Sheu, A. Liu, C. Barrett, and J. Wu, "Colossal thermal-mechanical actuation via phase transition in single-crystal vo 2 microcantilevers," *Journal of Applied Physics*, vol. 108, no. 8, p. 083 538, 2010.

[49] K. Liu, C. Cheng, Z. Cheng, K. Wang, R. Ramesh, and J. Wu, "Giant-amplitude, high-work density microactuators with phase transition activated nanolayer bimorphs," *Nano letters*, vol. 12, no. 12, pp. 6302–6308, 2012.

[50] B. Watson, J. Friend, and L. Yeo, "Piezoelectric ultrasonic micro/milli-scale actuators," *Sensors and Actuators A: Physical*, vol. 152, no. 2, pp. 219–233, 2009.

[51] D. L. Polla and L. F. Francis, "Processing and characterization of piezoelectric materials and integration into microelectromechanical systems," *Annual review of materials science*, vol. 28, no. 1, pp. 563–597, 1998.

[52] S. Trolier-McKinstry and P. Muralt, "Thin film piezoelectrics for mems," *Journal of Electroceramics*, vol. 12, no. 1-2, pp. 7–17, 2004.

[53] K. Bhattacharya and G. Ravichandran, "Ferroelectric perovskites for electromechanical actuation," *Acta Materialia*, vol. 51, no. 19, pp. 5941–5960, 2003.

[54] R. Jaramillo, F. Schoofs, S. D. Ha, and S. Ramanathan, "High pressure synthesis of smnio 3 thin films and implications for thermodynamics of the nickelates," *Journal of Materials Chemistry C*, vol. 1, no. 13, pp. 2455–2462, 2013.

[55] F. Capon, D. Horwat, J. Pierson, M. Zaghrioui, and P. Laffez, "Thermochromic effect in ndnio3- δ thin films annealed in ambient air," *Journal of Physics D: Applied Physics*, vol. 42, no. 18, p. 182 006, 2009.

[56] P. Laffez, M. Zaghrioui, R. Retoux, and P. Lacorre, "Oriented and polycrystalline ndnio3 thin films on silicon substrate," *Journal of magnetism and magnetic materials*, vol. 211, no. 1-3, pp. 111–117, 2000.

[57] G. Catalan, R. Bowman, and J. Gregg, "Metal-insulator transitions in ndnio 3 thin films," *Physical Review B*, vol. 62, no. 12, p. 7892, 2000.

[58] G. Catalan, R. Bowman, and J. Gregg, "Transport properties of ndnio 3 thin films made by pulsed-laser deposition," *Journal of Applied Physics*, vol. 87, no. 1, pp. 606–608, 2000.

[59] H. Kim, a. C. Gilmore, A. Pique, J. Horwitz, H. Mattoussi, H. Murata, Z. Kafafi, and D. Chrisey, "Electrical, optical, and structural properties of indium–tin–oxide thin films for organic light-emitting devices," *Journal of applied physics*, vol. 86, no. 11, pp. 6451–6461, 1999.

[60] Y. Hu, X. Diao, C. Wang, W. Hao, and T. Wang, "Effects of heat treatment on properties of ito films prepared by rf magnetron sputtering," *Vacuum*, vol. 75, no. 2, pp. 183–188, 2004.

[61] H. Kim, J. Horwitz, G. Kushto, A. Pique, Z. Kafafi, C. Gilmore, and D. Chrisey, "Effect of film thickness on the properties of indium tin oxide thin films," *Journal of Applied Physics*, vol. 88, no. 10, pp. 6021–6025, 2000.

[62] R. E. Honig, *Vapor pressure data for the more common elements*. David Sarnoff Research Center, 1957.

[63] A. Sarangan, *Nanofabrication: Principles to Laboratory Practice*. CRC Press, 2016.

[64] J. Bhardwaj, H. Ashraf, and A. McQuarrie, "Dry silicon etching for mems," in *Proc. Symp. Microstructures and Microfabricated Systems, ECS*, 1997, pp. 1–13.

[65] G. K. Fedder, "Mems fabrication," in *null*, Citeseer, 2003, p. 691.

[66] H.-B. Fang, J.-Q. Liu, Z.-Y. Xu, L. Dong, L. Wang, D. Chen, B.-C. Cai, and Y. Liu, "Fabrication and performance of mems-based piezoelectric power generator for vibration energy harvesting," *Microelectronics Journal*, vol. 37, no. 11, pp. 1280–1284, 2006.

[67] Y. Liao, *Practical electron microscopy and database*, 2006.

[68] O. M. Amirmajdi, R. Ashyer-Soltani, M. P. Clode, S. H. Mannan, Y. Wang, E. Cabruja, and G. Pellegrini, "Cross-section preparation for solder joints and mems device using argon ion beam milling," *IEEE transactions on electronics packaging manufacturing*, vol. 32, no. 4, pp. 265–271, 2009.

[69] H. Winters and J. Coburn, "The etching of silicon with xef2 vapor," *Applied Physics Letters*, vol. 34, no. 1, pp. 70–73, 1979.

[70] D.-I. Cho, *Silicon etching apparatus using xef2*, US Patent 6,736,987, May 2004.

[71] T. Zhu, P. Argyrakis, E. Mastropaolo, K. K. Lee, and R. Cheung, "Dry etch release processes for micromachining applications," *Journal of Vacuum Science & Technology B: Microelectronics and Nanometer Structures Processing, Measurement, and Phenomena*, vol. 25, no. 6, pp. 2553–2557, 2007.

[72] *What Is Geometric Nonlinearity?* en. [Online]. Available: https://www.comsol.com/blogs/what-is-geometric-nonlinearity/ (visited on 09/16/2020).

[73] T. Mirfakhrai, J. D. Madden, and R. H. Baughman, "Polymer artificial muscles," *Materials Today*, vol. 10, no. 4, pp. 30–38, 2007, ISSN: 1369-7021.

[74] K. Liu, C. Cheng, Z. Cheng, K. Wang, R. Ramesh, and J. Wu, "Giant-amplitude, high-work density microactuators with phase transition activated nanolayer bimorphs," *Nano Letters*, vol. 12, no. 12, pp. 6302–6308, 2012, ISSN: 1530-6984.

[75] I. W. Hunter, J. M. Hollerbach, and J. Ballantyne, "A comparative analysis of actuator technologies for robotics," *Robotics Review*, vol. 2, pp. 299–342, 1991.

[76] F. Carpi, S. Bauer, and D. De Rossi, "Stretching dielectric elastomer performance," *Science*, vol. 330, no. 6012, pp. 1759–1761, 2010, ISSN: 0036-8075.

[77] J. D. Madden, N. A. Vandesteeg, P. A. Anquetil, P. G. Madden, A. Takshi, R. Z. Pytel, S. R. Lafontaine, P. A. Wieringa, and I. W. Hunter, "Artificial muscle technology: Physical principles and naval prospects," *IEEE Journal of Oceanic Engineering*, vol. 29, no. 3, pp. 706–728, 2004, ISSN: 0364-9059.

[78] S. Arora, T. Ghosh, and J. Muth, "Dielectric elastomer based prototype fiber actuators," *Sensors and Actuators A: Physical*, vol. 136, no. 1, pp. 321–328, 2007, ISSN: 0924-4247.

[79] C.-K. Chen, L.-J. Yeh, and M.-C. Chiu, "A study of mechanical property for a type of shape memory alloy," *Journal of Information and Optimization Sciences*, vol. 32, no. 4, pp. 863–875, 2011, ISSN: 0252-2667.

[80] H. Li, C. Tian, and Z. D. Deng, "Energy harvesting from low frequency applications using piezoelectric materials," *Applied Physics Reviews*, vol. 1, no. 4, p. 041 301, 2014, ISSN: 1931-9401.

[81] J. Scortesse, J. Manceau, F. Bastien, M. Lejeune, S. Kurutcharry, and M. Oudjedi, "Apparent young's modulus in pmn-pt electrostrictive ceramics," *The European Physical Journal-Applied Physics*, vol. 14, no. 3, pp. 155–158, 2001, ISSN: 1286-0042.

[82] Y. Chen, J. E. Snyder, C. R. Schwichtenberg, K. W. Dennis, D. Falzgraf, R. W. McCallum, and D. C. Jiles, "Effect of the elastic modulus of the matrix on magnetostrictive strain in composites," *Applied Physics Letters*, vol. 74, no. 8, pp. 1159–1161, 1999, ISSN: 0003-6951.

[83] Y. Bar-Cohen, Ed., *Electroactive Polymer (EAP) Actuators as Artificial Muscles: Reality, Potential, and Challenges, Second Edition*, en. 1000 20th Street, Bellingham, WA 98227-0010 USA: SPIE, Mar. 2004, ISBN: 978-0-8194-5297-9. DOI: 10.1117/3.547465. [Online]. Available: http://link.aip.org/link/doi/10.1117/3.547465 (visited on 06/12/2020).

[84] C. Huang, Z. Zhang, S. Ramanathan, and D. Weinstein, "Vo 2 phase-transition-based vertical mems microactuators," *IEEE Transactions on Electron Devices*, vol. 66, no. 10, pp. 4380–4386, 2019.

[85] G. Andersson, "Studies on vanadium oxides, ii. the crystal structure of vanadium dioxide," *Acta Chem. Scand.*, pp. 623–628, 1956.

[86] B. Rajeswaran, L. Viannie, K. Rajanna, G. Jayanth, and A. Umarji, "Phase transition induced micromechanical actuation in vo2 coated cantilever," *Journal of Applied Physics*, vol. 124, no. 7, p. 074 502, 2018.

[87] K. Dong, S. Lou, H. S. Choe, K. Liu, Z. You, J. Yao, and J. Wu, "Stress compensation for arbitrary curvature control in vanadium dioxide phase transition actuators," *Applied Physics Letters*, vol. 109, no. 2, p. 023 504, 2016.

[88] E. Merced, D. Torres, X. Tan, and N. Sepúlveda, "An electrothermally actuated vo2-based mems using self-sensing feedback control," *Journal of Microelectromechanical Systems*, vol. 24, no. 1, pp. 100–107, 2014.

[89] N. Manca, L. Pellegrino, T. Kanki, Y. Higuchi, W. Venstra, G. Mattoni, A. Caviglia, H. Tanaka, and D. Marre, "Vo2: A material for high-performance micro/nanoactuators," in *ACTUATOR 2018; 16th International Conference on New Actuators*, VDE, 2018, pp. 1–4.

[90] F. Morin, "Oxides which show a metal-to-insulator transition at the neel temperature," *Physical review letters*, vol. 3, no. 1, p. 34, 1959.

[91] L. De'Medici, A. Georges, G. Kotliar, and S. Biermann, "Mott transition and kondo screening in f-electron metals," *Physical review letters*, vol. 95, no. 6, p. 066 402, 2005.

[92] J. Goodenough, "Semiconductor-to-metal transition in vo2," in *AMERICAN CERAMIC SOCIETY BULLETIN*, AMER CERAMIC SOC 600 N CLEVELAND AVE, WESTERVILLE, OH 43082 USA, vol. 50, 1971, pp. 390–+.

[93] K. Appavoo and R. F. Haglund Jr, "Detecting nanoscale size dependence in vo2 phase transition using a split-ring resonator metamaterial," *Nano letters*, vol. 11, no. 3, pp. 1025–1031, 2011.

[94] D. McWhan, M. Marezio, J. Remeika, and P. Dernier, "X-ray diffraction study of metallic vo2," *Physical Review B*, vol. 10, no. 2, p. 490, 1974.

[95] D. Kucharczyk and T. Niklewski, "Accurate x-ray determination of the lattice parameters and the thermal expansion coefficients of vo2 near the transition temperature," *Journal of Applied Crystallography*, vol. 12, no. 4, pp. 370–373, 1979.

[96] K. Wang, C. Cheng, E. Cardona, J. Guan, K. Liu, and J. Wu, "Performance limits of microactuation with vanadium dioxide as a solid engine," *ACS nano*, vol. 7, no. 3, pp. 2266–2272, 2013.

[97] E. Merced, X. Tan, and N. Sepúlveda, "Strain energy density of vo2-based microactuators," *Sensors and Actuators A: Physical*, vol. 196, pp. 30–37, 2013.

[98] R. Cabrera, E. Merced, and N. Sepúlveda, "Performance of electro-thermally driven vo2-based mems actuators," *Journal of microelectromechanical systems*, vol. 23, no. 1, pp. 243–251, 2013.

[99] K. Dong, H. S. Choe, X. Wang, H. Liu, B. Saha, C. Ko, Y. Deng, K. B. Tom, S. Lou, L. Wang, *et al.*, "A 0.2 v micro-electromechanical switch enabled by a phase transition," *Small*, vol. 14, no. 14, p. 1 703 621, 2018.

[100] M. Son, X. Liu, S. M. Sadaf, D. Lee, S. Park, W. Lee, S. Kim, J. Park, J. Shin, S. Jung, *et al.*, "Self-selective characteristics of nanoscale vo2 devices for high-density reram applications," *IEEE electron device letters*, vol. 33, no. 5, pp. 718–720, 2012.

[101] M.-J. Lee, Y. Park, D.-S. Suh, E.-H. Lee, S. Seo, D.-C. Kim, R. Jung, B.-S. Kang, S.-E. Ahn, C. B. Lee, *et al.*, "Two series oxide resistors applicable to high speed and high density nonvolatile memory," *Advanced Materials*, vol. 19, no. 22, pp. 3919–3923, 2007.

[102] K. R. Williams and R. S. Muller, "Etch rates for micromachining processing," *Journal of Microelectromechanical systems*, vol. 5, no. 4, pp. 256–269, 1996.

[103] A. Cengel Yunus, *Heat Transfer: A Practical Approach*. New York, NY, USA: McGraw-Hill, 2002.

[104] A. E. Kaloyeros, F. A. Jové, J. Goff, and B. Arkles, "Silicon nitride and silicon nitride-rich thin film technologies: Trends in deposition techniques and related applications," *ECS Journal of Solid State Science and Technology*, vol. 6, no. 10, P691, 2017.

[105] S.-K. Choi and J. Lee, "Effect of film density on electrical properties of indium tin oxide films deposited by dc magnetron reactive sputtering," *Journal of Vacuum Science & Technology A: Vacuum, Surfaces, and Films*, vol. 19, no. 5, pp. 2043–2047, 2001.

[106] T. Ashida, A. Miyamura, N. Oka, Y. Sato, T. Yagi, N. Taketoshi, T. Baba, and Y. Shigesato, "Thermal transport properties of polycrystalline tin-doped indium oxide films," *Journal of applied physics*, vol. 105, no. 7, p. 073 709, 2009.

[107] D.-W. Oh, C. Ko, S. Ramanathan, and D. G. Cahill, "Thermal conductivity and dynamic heat capacity across the metal-insulator transition in thin film vo2," *Applied Physics Letters*, vol. 96, no. 15, p. 151 906, 2010.

[108] C. Berglund and H. Guggenheim, "Electronic properties of vo2 near the semiconductor-metal transition," *Physical Review*, vol. 185, no. 3, p. 1022, 1969.

[109] D. R. Lide, *CRC handbook of chemistry and physics: a ready-reference book of chemical and physical data*. CRC press, 1995.

[110] D. R. Cairns, D. C. Paine, and G. P. Crawford, "The mechanical reliability of sputter-coated indium tin oxide polyester substrates for flexible display and touchscreen applications," *MRS Online Proceedings Library Archive*, vol. 666, 2001.

[111] P. Jin, S. Nakao, S. Tanemura, T. Bell, L. Wielunski, and M. Swain, "Characterization of mechanical properties of vo2 thin films on sapphire and silicon by ultra-microindentation," *Thin Solid Films*, vol. 343, pp. 134–137, 1999.

[112] A. D. Carter and S. Elhadj, "Modulus of elasticity and thermal expansion coefficient of ito film," Lawrence Livermore National Lab.(LLNL), Livermore, CA (United States), Tech. Rep., 2016.

[113] Y. Cao, D. Torres, T. Wang, X. Tan, and N. Sepúlveda, "Enabling tunable micromechanical bandpass filters through phase-change materials," *Smart Materials and Structures*, vol. 26, no. 8, p. 085 032, 2017.

[114] Z. Yang, C. Ko, and S. Ramanathan, "Oxide electronics utilizing ultrafast metal-insulator transitions," *Annual Review of Materials Research*, vol. 41, pp. 337–367, 2011.

[115] B. Viswanath and S. Ramanathan, "Direct in situ observation of structural transition driven actuation in vo 2 utilizing electron transparent cantilevers," *Nanoscale*, vol. 5, no. 16, pp. 7484–7492, 2013.

[116] B. Van Zeghbroeck, "Principles of semiconductor devices," *Colarado University*, vol. 34, 2004.